


5-2013

# III-V Bismide Optoelectronic Devices

Dongsheng Fan

*University of Arkansas, Fayetteville*

Follow this and additional works at: <http://scholarworks.uark.edu/etd>

 Part of the [Electronic Devices and Semiconductor Manufacturing Commons](#), [Nanoscience and Nanotechnology Commons](#), [Nanotechnology Fabrication Commons](#), and the [Semiconductor and Optical Materials Commons](#)

---

## Recommended Citation

Fan, Dongsheng, "III-V Bismide Optoelectronic Devices" (2013). *Theses and Dissertations*. 598.  
<http://scholarworks.uark.edu/etd/598>

This Dissertation is brought to you for free and open access by ScholarWorks@UARK. It has been accepted for inclusion in Theses and Dissertations by an authorized administrator of ScholarWorks@UARK. For more information, please contact [scholar@uark.edu](mailto:scholar@uark.edu), [ccmiddle@uark.edu](mailto:ccmiddle@uark.edu).



## III-V BISMIDE OPTOELECTRONIC DEVICES

# III-V BISMIDE OPTOELECTRONIC DEVICES

A dissertation submitted in partial fulfillment  
of the requirements for the degree of  
Doctor of Philosophy in Electrical Engineering

By

Dongsheng Fan  
Tianjin University  
Bachelor of Science in Microelectronic Technology, 2002  
Institute of Microelectronics of Chinese Academy of Sciences  
Master of Science in Microelectronics and Solid State Electronics, 2005

May 2013  
University of Arkansas

## ABSTRACT

This dissertation explores modeling, molecular beam epitaxy growth, and fabrication of III-V bismide optoelectronic devices, which are of great importance in modern applications of telecommunication, gas sensing, environment monitoring, etc. In the current room-temperature continuous-wave operational GaSb-based type-I InGaAsSb/AlGaInAsSb quantum well laser diodes in 3-4  $\mu\text{m}$  mid-wavelength range, the lasing wavelength and performance of the devices are limited due to the lack of hole confinement in the active regions. In this dissertation, a novel GaSb-based GaInAsSbBi material is proposed to replace the conventional InGaAsSb material in the quantum well region, which enables the laser diodes achieve up to 4  $\mu\text{m}$  optical transition wavelength with significantly enhanced hole confinement. Moreover, quasi-Al-free laser diode designs are realized for the first time in this wavelength range by employing GaInAsSbBi/GaSb active region and InGaAsSb cladding layers, which considerably improves the reliability of the laser diodes. In addition, GaInAsSbBi material is proposed to be used for high efficiency thermophotovoltaic devices. It provides narrower bandgap than traditionally InGaAsSb material so that more low-energy photons can be utilized during the energy conversion to achieve higher efficiency.

In the development of GaAsBi/GaAs temperature-insensitive optoelectronic devices, laser diodes have not been realized due to the lack of separate confinement heterostructures, which is bottlenecked by the difficulty of growing high quality AlGaAs barrier layers at low temperatures. In this work, we systematically investigate the effects of Bi during the growth of GaAsBi and propose Bi-mediated growth to grow high quality AlGaAs at low temperatures. GaAsBi/GaAs/AlGaAs single quantum well and double quantum well separate confinement heterostructures with excellent structural and optical properties are grown using molecular beam

epitaxy with the upper AlGaAs layers grown at 320 °C. The surfactant effect of Bi is evidenced by the presence of a (1×3) surface reconstruction throughout the growth of AlGaAs. The Bi surfactant mediated growth of AlGaAs at low temperatures is reported for the first time. Process flows and photomasks are developed to fabricate optoelectronic devices. The capability and flexibility of the processes are successfully demonstrated by the fabrication of high performance GaAs quantum well laser diodes and InAs quantum dots light emitting diodes.

This dissertation is approved for recommendation  
to the Graduate Council.

Dissertation Director:

---

(Dr. Shui-Qing Yu)

Dissertation Committee:

---

(Dr. Gregory J. Salamo)

---

(Dr. Hameed A. Naseem)

---

(Dr. Simon S. Ang)

**DISSERTATION DUPLICATION RELEASE**

I hereby authorize the University of Arkansas Libraries to duplicate this dissertation when needed for research and/or scholarship.

Agreed \_\_\_\_\_  
(Dongsheng Fan)

Refused \_\_\_\_\_  
(Dongsheng Fan)



## ACKNOWLEDGEMENTS

First of all, I would like to deeply thank my advisor Professor Shui-Qing Yu, for being an amazing mentor and supporting my study and research in University of Arkansas. He has guided me throughout the years with his innovative thinking, insightful suggestions and constant encouragement. I am greatly impressed by his vision, passion, and enthusiasm which I wish I could emulate a fraction of. I have truly enjoyed the time in Yu group and I am very grateful for everything he has done for me.

I am extremely grateful to Professor Gregory Salamo for allowing me to work on the MBE in his lab. He has graciously provided me the assistance and guidance whenever I needed. My discussions with him have always been enlightening and his effort in maintaining an open research environment has broadened my thinking both academically and personally. I am honored to have him on my research committee.

I would also like to thank Professor Hameed Naseem and Professor Simon Ang for taking time out of their busy schedules to serve as my research committee members. Their feedback to my research was invaluable assessment of the areas that I needed pay attention to. I am very grateful for their help during my research.

This work could not have been done without the help of a number of people. In particular, Dr. Zhiming Wang and Dr. Zhaoquan Zeng introduced me to and got me started on MBE growth. Dr. Zeng and I have spent almost one year to bring a flooded MBE into working conditions. I am especially grateful to him. I would also like to thank David Monk for maintaining the MBE lab with his seemingly effortless skills and patiently teaching me the techniques to fix the UHV and MBE instruments. Thanks go to Marvin Macedo for graciously allowing me to enroll his

class in the middle of the semester and use the facilities in his Nanofab. Thanks to Dr. Aqiang Guo for his help on lapping process development and device fabrication. Thanks to Chen Li for his help on MBE growth and maintenance. Xian Hu, Dr. Vitaliy Dorogan, Dr. Yuriy Mazur, Yusuke Hirono and P.C. Grant deserve much gratitude for their excellent characterization works on the III-V bismide samples. Great appreciation goes to Dr. Mourad Beramara and Dr. Michael Hawkrige for training and helping me on the TEM and HRXRD measurements.

I would also like to thank our collaborator Dr. Shane Johnson in Arizona State University for all his advices on the GaAsBi research and his refining my journal papers.

I am deeply indebted to my wife Xiaoxiao Zhang for her love, compassion and encouragement. I would not be here without her support. I give my special appreciation to my parents and my sister for their love and unconditional support. I cannot thank them enough for what they have done for me over the years. I would also like to thank my parents-in-law for their loving support and encouragement. Any finally, thanks to my friends that have been supporting me all the time.

This work was supported by NSF Career Award No. DMR-1149605, MRSEC Program of NSF Grant No. DMR-0520550, Arkansas Biosciences Institute.

## TABLE OF CONTENTS

1 Introduction.....	1
1.1 GaSb-based GaInAsSbBi MWIR laser diodes .....	5
1.2 GaAs-based GaAsBi temperature insensitive IR laser diodes .....	8
1.3 Scope of this dissertation .....	13
2 GaSb-based GaInAsSbBi for MWIR Laser Diode and TPV Applications .....	15
2.1 GaInAsSbBi for MWIR laser diodes .....	15
2.2 GaInAsSbBi alloys for TPV devices .....	35
2.3 Summary .....	45
3 Molecular Beam Epitaxy and Surfactant Mediated Growth.....	47
3.1 Brief introduction of molecular beam epitaxy .....	47
3.2 Bi surfactant mediated growth .....	49
3.3 Summary .....	54
4 MBE Growth of GaAsBi Alloys.....	55
4.1. GaAsBi/GaAs material growth .....	56
4.2 Effects of Bi flux on morphological and optical properties of GaAsBi .....	58
4.3 Effects of substrate temperature on the Bi composition .....	64
4.4 Structural Characterization of the GaAsBi/GaAs.....	65
4.5 Discussion of the growth of GaSbBi material .....	69
4.6 Summary .....	72

5 GaAsBi Separate Confinement Heterostructures.....	75
5.1 Motivation.....	75
5.2 SQW SCH development.....	78
5.3 Double quantum well development.....	84
5.4 Integration of DQW and SCH designs.....	88
5.5 Summary.....	92
6 Device fabrication.....	93
6.1 Motivation.....	93
6.2 Process flows.....	95
6.3 Mask design.....	101
6.4 Device demonstration.....	105
6.5 Summary.....	107
7 Conclusion and Future Work.....	109
7.1 Conclusion.....	109
7.2 Future work.....	111
Bibliography.....	113
Appendix A: Permission to reuse copyrighted materials.....	127
Appendix B: List of papers.....	138

## LIST OF FIGURES

Fig. 1.1 Group III and group V elements that compose compound semiconductor. ....	2
Fig. 1.2 Bandgaps and lattice constants of III-V materials.....	2
Fig 1.3 Development of GaSb-based type-I QW Mid-IR laser diodes in 3-4 $\mu\text{m}$ in last decade. The dashed line shows the state-of-art record of lasing wavelength of each year.....	6
Fig. 1.4 (a) Schematic of the CHSH Auger process, (b) schematic of the suppression of the CHSH Auger process in the proposed GaAsBi alloys.....	9
Fig. 1.5 Schematics of the band anti-crossing model for the GaAsN and GaAsBi. ....	9
Fig 1.6 Spin-orbit splitting energy of Ga and In containing binary alloys, showing the bismide alloys possessing significantly higher spin-orbit splitting energies than other binary alloys. ....	10
Fig. 1.7 Bandgap and spin-orbit splitting energy of GaAsBi alloys as a function of Bi composition, showing the spin-orbit splitting energy exceeds the bandgap at Bi composition of around 10.5%. ....	11
Fig. 2.1 Schematic band diagram of a typical GaSb-based InGaAsSb QW laser diode. The bandgaps and band offsets of the materials are drawn to scale. ....	16
Fig. 2.2 Band positions of lattice-matched InGaAsSb as a function of wavelength. The valence band of InSb is used as the reference position. The VBM of InGaAsSb decreases dramatically as the increase of wavelength.....	17
Fig. 2.3 Carrier confinement between the $\text{In}_{0.5}\text{Ga}_{0.5}\text{As}_{0.23}\text{Sb}_{0.77}$ QW regions and the lattice- matched AlGaAsSb barriers. As the increase of Al composition, the electron confinement rises much faster than the hole confinement does.....	18

Fig. 2.4 Electron and hole confinement of InGaAsSb/AlGaInAsSb active regions in the RT CW operational laser diodes made by Vizbaras <i>et al.</i> . As the increase of wavelength, there is a clear trend of decreased hole confinement. ....	19
Fig. 2.5 The wavelengths and In compositions of RT CW operational GaSb-based type-I InGaAsSb QW laser diodes. The wavelength is extended at the expense of increasing growth complexity to push the InGaAsSb alloys into deeper miscibility.....	21
Fig. 2.6 Bi 6p energy level relative to the band alignments of GaAs, GaSb, InAs, and InSb. ....	22
Fig. 2.7 Schematic of the bandgap interpolation of $Ga_xIn_{1-x}Sb_y(As_zBi_{1-z})_{1-y}$ alloys.....	23
Fig. 2.8 Optical transition wavelength contours of GaInAsSbBi QWs (with 1.5% compressive strain) at different In and Bi compositions. For a given wavelength, In composition decreases dramatically as Bi composition increases. ....	25
Fig 2.9 Contour plot of VBOs of GaInAsSbBi QWs with 1.5% compressive strain, showing the considerable increase of VBO as the decrease of In composition and the increase of Bi composition.....	26
Fig. 2.10 As composition and VBO as a function of Bi composition in the GaInAsSbBi QWs with 1.5% compressive strain and 4 $\mu$ m optical transition wavelength.....	27
Fig. 2.11 Carrier confinement between $Ga_{0.7}In_{0.3}As_{0.11}Sb_{0.77}Bi_{0.12}$ QW and lattice-matched AlGaAsSb barrier layer. The QW region has 1.5% compressive strain and the expected wavelength is 4 $\mu$ m. Balanced electron-hole confinement is obtained in a large Al composition range.....	28

Fig. 2.12 Carrier confinements of GaInAsSbBi/GaSb active regions with 4 $\mu\text{m}$ optical transition wavelength and 1.5% compressive strain in the QWs. Type-I band alignment is achieved in the Al-free active region when Bi composition exceeds 8%.....	29
Fig. 2.13 Laser structure design with 1.5% strain in the GaInAsSbBi QW region. The optical transition wavelength is 4 $\mu\text{m}$ . .....	30
Fig. 2.14 Good optical confinement of the proposed laser structure shown in Fig. 2.13 calculated by using Rsoft software. ....	31
Fig. 2.15 The effect of bowing coefficient on the bandgaps of GaAsBi alloys, showing the bandgap reduction is much underestimated by using linear interpolation.....	33
Fig. 2.16 The effect of the GaAsBi bowing coefficient on the optical transition wavelengths of the GaIn <sub>0.3</sub> AsSbBi QWs (with 1.5% compressive strain).....	34
Fig. 2.17 Schematic diagram of a typical TPV, including a heat source, a selective emitter and filter for spectral control, a photovoltaic diode cell (converter), and a reflector. ....	35
Fig. 2.18 Comparison of the solar extraterrestrial AM0 spectrum with the 1000K and 1400 K blackbody radiation spectra, showing the blackbody radiation spectra possessing much higher incident powers and much longer wavelength peaks.....	36
Fig. 2.19 Efficiency as a function of the bandgap with source temperatures varying from 1000K to 1800 K.....	38
Fig. 2.20 Power output as a function of the bandgap with source temperatures varying from 1000K to 1800 K.....	38
Fig. 2.21 Graphical analysis of the efficiencies of single-junction, double-junction and triple-junction TPV cells.....	40

(c) triple-junction ..... 41

Fig. 2.22 Efficiencies of multi-junction TPVs under 1400 K blackbody radiation. (a) single-junction; (b) double-junction; (c) triple-junction. The efficiency of the TPV cell is improved from 21.5% (single-junction) to 28.5% (double-junction) and 31.9% (triple-junction) respectively. .... 41

Fig. 2.23 Bandgap contours of GaInAsSbBi material (lattice-matched with GaSb) at different In and Bi compositions..... 43

Fig. 2.24 Schematic diagram of a three junction TPV cell which contains three diodes with different bandgaps connected in tandem..... 44

Fig. 3.1 Schematic diagram of a RHEED system..... 48

Fig 3.2 (a)  $1 \times 1 \mu\text{m}^2$  AFM image of the sample A (Bi-free) with the density of  $4.1 \times 10^{10} \text{cm}^{-2}$ ; (b)  $1 \times 1 \mu\text{m}^2$  AFM image of the sample B (Bi-mediated) with the density of  $2.0 \times 10^{10} \text{cm}^{-2}$ ; (c) Height histograms of samples A and B: the size distribution of sample B is shifted to the larger size direction. [D. Fan, *et al.*, “Bismuth surfactant mediated growth of InAs quantum dots by molecular beam epitaxy”, *J. Mater. Sci: Mater. Eletron.*, DOI: 10.1007/s10854-012-0987-z, 2012]. With kind permission from Springer Science and Business Media. .... 52

Fig. 3.3 Excitation intensity dependence of the wavelength-integrated PL intensity for Sample A grown without Bi (black diamonds) and Sample B grown with Bi (red circles). The measurement is performed at 16 K. The inset shows the spectra of the two samples at excitation intensity of  $0.02 \text{W/cm}^2$ . [D. Fan, *et al.*, “Bismuth surfactant mediated growth of InAs quantum dots by molecular beam epitaxy”, *J. Mater. Sci: Mater. Eletron.*, DOI: 10.1007/s10854-012-0987-z, 2012]. With kind permission from Springer Science and Business Media. .... 53



Fig. 4.1: Band diagram, growth temperature profile and cross-sectional STEM image of a typical GaAsBi/GaAs QW sample. ....	57
Fig. 4.2: (2 × 1) RHEED reconstruction pattern in the growth of GaAsBi QW region (a) and (1 × 3) pattern in the growth of GaAs cap layer (b). ....	57
Fig 4.3 AFM images of the six GaAsBi/GaAs QW samples grown at the same condition but with increasing Bi fluxes from (a) to (f). ....	59
Fig. 4.4: The effect of Bi flux on the morphology and optical properties of GaAsBi/GaAs QW samples A-F: (a) surface roughness, (b) density of Bi droplets, (c) PL peak wavelength, (d) Bi content, (e) FWHM of the PL spectra, and (f) integrated PL intensity. ....	60
Fig. 4.5 PL spectra of the GaAsBi/GaAs QW samples measured at 18 K (a) and RT (b). The samples with intermediate Bi fluxes show best optical properties. ....	62
Fig. 4.6 PL peak wavelength of GaAsBi bulk samples grown at the same condition but with different growth temperatures. The emission wavelength increases steadily as decreasing temperatures. ....	64
Fig. 4.7 PL spectra of the GaAsBi bulk samples measured at 18 K (a) and RT (b). The samples are grown at the same growth condition except with different Bi flux. The samples show good optical properties at both low temperature and room temperature. ....	65
Fig. 4.8 HRXRD (004) $\theta$ -2 $\theta$ scan of a GaAsBi QW sample (Sample C). The red line is the best fitting of the experimental data and the best fit value of Bi composition is $4.0\pm 0.5\%$ . ....	66
Fig. 4.9 High resolution bright field cross-sectional TEM image of a GaAsBi/GaAs QW sample (sample C). Clear lattice image of the layers can be seen. ....	67

Fig. 4.10 EDS analysis of the GaAsBi/GaAs QW sample in GaAs cap layer (a), GaAs QW region (b), and GaAs buffer layer (c). The Bi peaks in (b) directly affirm the Bi's incorporation in GaAsBi QW region and the absence of Bi peak in (a) indicates that no detectable Bi is incorporated into the GaAs cap layer..... 68

Fig. 4.11 HRXRD (004)  $\theta$ -2 $\theta$  scan of the GaSb buffer layer grown on GaSb substrate, showing the unintentionally incorporated As in the GaSb buffer layer with As composition of 0.58%. ... 71

Fig. 4.12 A  $2 \times 2 \mu\text{m}^2$  AFM image a Ga(As,Sb,Bi) sample, showing the atomically flat surface without droplet..... 71

Fig. 4.13 HRXRD (004)  $\theta$ -2 $\theta$  scan of the Ga(As,Sb,Bi) sample grown on GaAsSb buffer at 320 °C, showing the additional peak to due to the effect of Bi. .... 72

Fig. 5.1 Band diagrams, growth temperature profiles and cross-sectional TEM images of sample A with separate confinement (a) and sample B without separate confinement (b). The upper AlGaAs barrier in sample A is grown at the GaAsBi growth temperature 320 °C. Reprinted with permission from [D. Fan, *et al.*, "Molecular beam epitaxy growth of GaAsBi/GaAs/AlGaAs separate confinement heterostructures", *Appl. Phys. Lett.*, vol. 101, pp. 181103, 2012]. Copyright [2012], American Institute of Physics. .... 79

Fig. 5.2 High-resolution x-ray diffraction patterns of  $\theta$ -2 $\theta$  scans from (004) planes of sample A and sample B. The red lines are the best fit models of the experimental data. Reprinted with permission from [D. Fan, *et al.*, "Molecular beam epitaxy growth of GaAsBi/GaAs/AlGaAs separate confinement heterostructures", *Appl. Phys. Lett.*, vol. 101, pp. 181103, 2012]. Copyright [2012], American Institute of Physics. .... 80

Fig. 5.3 High resolution bright field cross-sectional TEM image of sample A with separate confinement. Reprinted with permission from [D. Fan, *et al.*, “Molecular beam epitaxy growth of GaAsBi/GaAs/AlGaAs separate confinement heterostructures”, *Appl. Phys. Lett.*, vol. 101, pp. 181103, 2012]. Copyright [2012], American Institute of Physics. .... 81

Fig. 5.4 Photoluminescence spectra at RT: Sample A with separate confinement (blue curve) and Sample B without separate confinement (red curve). The photoexcitation density is  $1.4 \text{ W/cm}^2$  and the PL peak intensity of sample A is  $\sim 10$  times higher than that of sample B. Reprinted with permission from [D. Fan, *et al.*, “Molecular beam epitaxy growth of GaAsBi/GaAs/AlGaAs separate confinement heterostructures”, *Appl. Phys. Lett.*, vol. 101, pp. 181103, 2012]. Copyright [2012], American Institute of Physics. .... 82

Fig. 5.5 PL spectra of samples B, C, D, and E measured at 18 K: (a) Sample B (SQW reference sample); (b) Sample C (with a 7.5 nm-thick GaAs spacer); (b) Sample D (with a 15 nm-thick GaAs spacer); (d) Sample E (with 7.5 nm-thick GaAs spacer and reduced Bi flux for the second QW growth). Reprinted with permission from [D. Fan, *et al.*, “MBE Grown GaAsBi/GaAs Double Quantum Well Separate Confinement Heterostructures”, *J. Vac. Sci Technol. B*, vol. 31, pp. 03C105, 2013]. Copyright [2013], American Vacuum Society. .... 85

Fig. 5.6 PL spectra of DQW sample E at 18 K (black dash-line) and RT (red solid-line) to show that the sample exhibits a single PL peak at both temperatures. Reprinted with permission from [D. Fan, *et al.*, “MBE Grown GaAsBi/GaAs Double Quantum Well Separate Confinement Heterostructures”, *J. Vac. Sci Technol. B*, vol. 31, pp. 03C105, 2013]. Copyright [2013], American Vacuum Society. .... 88

Fig. 5.7 Schematic of cross-section with growth temperature profile and low magnification bright field cross-sectional TEM image of DQW SCH sample (sample F) to show smooth interfaces

between the different layers. Reprinted with permission from [D. Fan, <i>et al.</i> , “MBE Grown GaAsBi/GaAs Double Quantum Well Separate Confinement Heterostructures”, <i>J. Vac. Sci Technol. B</i> , vol. 31, pp. 03C105, 2013]. Copyright [2013], American Vacuum Society. ....	89
Fig. 5.8 A comparison of RT PL spectra of DQW SCH sample (sample F, red solid-line) and SQW SCH reference sample (sample A, black dash-line) to show high optical quality of the DQW SCH. Reprinted with permission from [D. Fan, <i>et al.</i> , “MBE Grown GaAsBi/GaAs Double Quantum Well Separate Confinement Heterostructures”, <i>J. Vac. Sci Technol. B</i> , vol. 31, pp. 03C105, 2013]. Copyright [2013], American Vacuum Society. ....	90
Fig. 5.9 PL comparison between a SQW GaAsBi sample (sample B) and an optimized GaAsSb SQW benchmark sample, indicating good properties of the GaAsBi sample. ....	91
Fig. 6.1 Schematic diagram of an edge emitter. ....	95
Fig. 6.2 Cross-sectional process flow diagram for edge emitters with oxide isolation. ....	96
Fig. 6.3 Optical microscope images of the sample after the lithography (a) and wet etching process (b) respectively. ....	98
Fig. 6.4 Optical microscope image of the sample after the p-metal deposition. ....	99
Fig. 6.5 Optical microscope image of the cleaved sample on the probe station. ....	100
Fig. 6.6 Mask designs for edge emitting laser diodes (a-d) and the corresponding image on wafer level (e). ....	101
Fig. 6.7 Mask of photo-detectors with different sizes. The MESA layer is in red and the metal layer is in blue. ....	102
Fig. 6.8 Schematic diagrams of vernier scale alignment marks. (a) Perfectly aligned; (b) misaligned by 3 $\mu\text{m}$ . ....	103

Fig. 6.9 An optical microscope image of the vernier scale in the processing of laser diodes. The center bars of the two layers are well aligned and the overlay error is within 1 $\mu\text{m}$ . .....	104
Fig. 6.10 Metal scales in mask design (a) and on wafer surface (b). The major ticks are placed every 100 $\mu\text{m}$ and four minor ticks are placed between the major ticks. ....	104
Fig. 6.11 Cross-sectional SEM image of a GaAs QW laser diode. ....	105
Fig 6.12 I-L curve of a RT CW operational GaAs QW laser diode. ....	106
Fig. 6.13 RT spectra of an InAs QD LED. The inset shows the AFM image of InAs QDs grown on nano-holes patterned GaAs substrate.....	107

## LIST OF TABLES

Table 1.1 Summary of the III-V bismide materials used for IR optoelectronics applications. ....	4
Table 1.2 Toxic gases with absorption lines in the MWIR range.....	5
Table 2.1 Bandgaps of binary alloys and bowing coefficients used in the $Ga_xIn_{1-x}Sb_y(As_zBi_{1-z})_{1-y}$ interpolation [2,106]. (Unit: eV).....	24
Table 2.2 VBOs of the binary alloys used in the linear interpolation of $Ga_xIn_{1-x}Sb_y(As_zBi_{1-z})_{1-y}$ .	24
Table 3.1: Summary of the layer stacks of the InAs QD samples, including the thickness and growth temperature of each layer. Sample A (the control sample) is grown without Bi (Bi-free). Sample B is grown with Bi (Bi-mediated). [D. Fan, <i>et al.</i> , “Bismuth surfactant mediated growth of InAs quantum dots by molecular beam epitaxy”, <i>J. Mater. Sci: Mater. Eletron.</i> , DOI: 10.1007/s10854-012-0987-z, 2012]. With kind permission from Springer Science and Business Media. ....	51

## LIST OF ACRONYMS

<b>AFM</b>	atomic force microscopy
<b>CHSH</b>	conduction-heavy hole and split-off hole-heavy hole
<b>CW</b>	continuous-wave
<b>DH</b>	double heterostructure
<b>DQW</b>	double quantum well
<b>EDS</b>	energy dispersive x-ray spectroscopy
<b>FWHM</b>	full width at half maximum
<b>HAADF</b>	high angle annular dark field
<b>HEMT</b>	high mobility electron transistor
<b>HMDS</b>	hexamethyldisiloxane
<b>HRXRD</b>	high resolution x-ray diffraction
<b>LED</b>	light emitting diode
<b>LIDAR</b>	light detection and ranging
<b>LPE</b>	liquid phase epitaxy
<b>LT</b>	low temperature
<b>LWIR</b>	long-wave infrared
<b>MBE</b>	molecular beam epitaxy
<b>MEE</b>	migration enhanced epitaxy
<b>MIM</b>	monolithic interconnected module

<b>MQW</b>	multiple quantum well
<b>MOCVD</b>	metalorganic chemical vapor deposition
<b>MOVPE</b>	metal organic vapor phase epitaxy
<b>MWIR</b>	mid-wavelength infrared
<b>NIR</b>	near-infrared
<b>PECVD</b>	plasma enhanced chemical vapor deposition
<b>PL</b>	photoluminescence
<b>PR</b>	photoreflectance
<b>QD</b>	quantum dot
<b>QW</b>	quantum well
<b>RBS</b>	Rutherford backscattering spectrometry
<b>RHEED</b>	reflected high energy electron diffraction
<b>RMS</b>	root mean square
<b>RT</b>	room temperature
<b>RTA</b>	rapid thermal annealing
<b>SCH</b>	separate confinement heterostructure
<b>SEM</b>	scanning electron microscopy
<b>SLT</b>	stoichiometric low temperature
<b>SQW</b>	single quantum well
<b>STEM</b>	scanning transmission electron microscopy



<b>SWIR</b>	short-wave infrared
<b>TEC</b>	thermo-electric cooler
<b>TEM</b>	transmission electron microscopy
<b>TLM</b>	transmission line method
<b>TPV</b>	thermophotovoltaic
<b>UHV</b>	ultra-high vacuum
<b>VBM</b>	valance band maximum
<b>VBO</b>	valence band offset
<b>VLWIR</b>	very-long wave infrared

## 1 INTRODUCTION

In last several decades, there has been incredible in the advancement of information technology which has made tremendous technological and social impact on people's lives. High performance personal computers, internet and smart phones exponentially increase the productivity of the whole society as well as revolutionarily facilitating the communication between people. The world has been connected in a way that is even hard to imagine before. The explosively evolved information technology not only relies on the aggressive development of the semiconductor industry but also relies on the fast development of the telecommunication industry. For example, the operation of the complicated programs such as Youtube and Skype is enabled by the high-speed integrated circuits in the personal computers, while the video and audio data have to be retrieved via high speed networks.

The main impulse to the development of telecommunication industry came from the innovation in optoelectronic devices, including laser diodes, light emitting diodes (LEDs) and photo-detectors. The optoelectronic devices are usually made of the III-V compound semiconductors due to their direct bandgaps [1]. The III-V compound semiconductor is composed of at least one group III element and one group V element, as shown in Fig. 1.1. The alloy can be categorized as nitride, phosphide, arsenide, antimonide and bismide according to the compositional group V elements. One great advantage of the III-V compound semiconductor is that it is possible to engineer its bandgap to tune the working wavelength of the optoelectronic devices. What's more exciting is that the engineering can be simply done by mixing the alloys with different bandgaps together. Fig. 1.2 shows the bandgaps of several binary alloys with different bandgaps and the lines between the binary alloys represents the possible bandgaps of

ternary alloys composed of the two binary alloys [2-3]. For example, the bandgap of  $\text{GaAs}_{1-x}\text{Sb}_x$  can be tuned between the bandgap of GaAs (1.423 eV) to the bandgap of GaSb (0.726 eV) along the line between the two alloys.

III	V		
5 <b>B</b>	7 <b>N</b>	Nitride:	GaN, AlGaN
13 <b>Al</b>	15 <b>P</b>	Phosphide:	InP, GaInP
31 <b>Ga</b>	33 <b>As</b>	Arsenide:	GaAs, InGaAs
49 <b>In</b>	51 <b>Sb</b>	Antimonide:	GaSb, GaAsSb
81 <b>Tl</b>	83 <b>Bi</b>	Bismide:	GaAsBi, InAsSbBi

Fig. 1.1 Group III and group V elements that compose compound semiconductor.

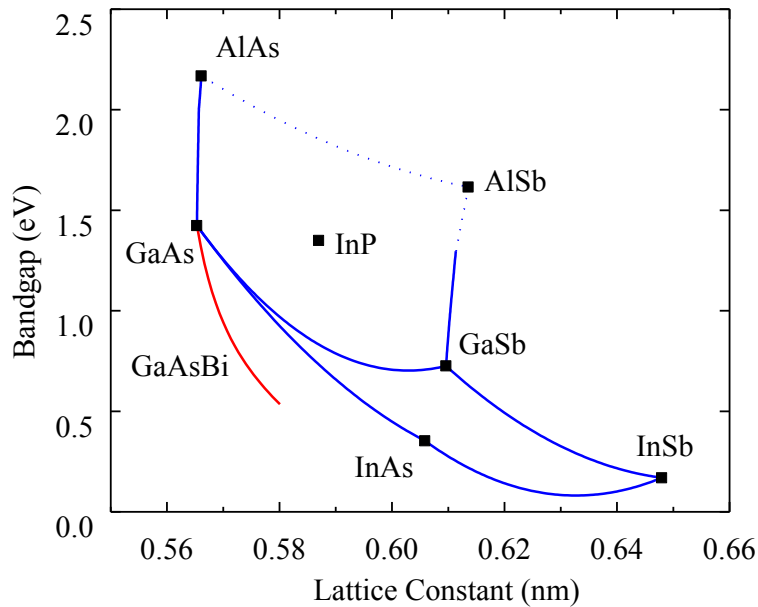


Fig. 1.2 Bandgaps and lattice constants of III-V materials.

Due to the wide range of the III-V compound semiconductor bandgaps, the optoelectronic devices are capable of covering a wide range of wavelength spectrum range including ultraviolet,

visible, near-infrared (NIR), short-wave infrared (SWIR), mid-wave infrared (MWIR), long-wave infrared (LWIR) and very-long wave infrared (VLWIR). The applications of the optoelectronic devices widely span from telecommunication to sensing and to imaging [4-7].

A lot of other III-V materials, such as nitride, phosphide and arsenide, have made huge success in research and commercialization. By contrast, the III-V bismide materials are much less explored and still remain in the preliminary research phase. The research on III-V bismide starts with  $\text{InSb}_{1-x}\text{Bi}_x$  material for LWIR applications in 8-12  $\mu\text{m}$ , which was first grown by Joukoff *et al.* in 1972 using Czochralski method [8]. About ten years later,  $\text{InSb}_{1-x}\text{Bi}_x$  was grown on InSb substrates using molecular beam epitaxy (MBE) by Oe *et al.* in 1981 and Noreika *et al.* in 1982 [9-10]. Six year later  $\text{InSb}_{1-x}\text{Bi}_x$  and  $\text{InAs}_{1-x-y}\text{Sb}_x\text{Bi}_y$  were demonstrated by Humphreys *et al.* using metalorganic chemical vapor deposition (MOCVD) on GaAs and InSb substrates with Bi composition up to 14% and 4% respectively [11]. In 1990, Ma *et al.* and Fang *et al.* have demonstrated  $\text{InAsBi}_x$  and  $\text{InAs}_{1-x-y}\text{Sb}_x\text{Bi}_y$  on InAs substrates with Bi composition up to 3.1% and characterized the photoluminescence (PL) of the materials [12-13]. In these studies, the bandgap of  $\text{InAs}_{1-x}\text{Bi}_x$  is reduced with the slope of -55 meV/Bi% and the bandgap of  $\text{InSb}_{1-x}\text{Bi}_x$  is reduced with the slope of -36 meV/Bi% [12-14]. In 1997, Lee *et al.* has demonstrated the cut-off wavelength of 9.3  $\mu\text{m}$  (at 77K) using MOCVD grown InSbBi on InSb substrates [15]; Du *et al.* has demonstrated the cut-off wavelength of 10.7  $\mu\text{m}$  (at 77K) using MBE grown GaInSbBi on InP substrates [16].

The second milestone of the III-V bismide material research is the achievement of  $\text{GaAs}_{1-x}\text{Bi}_x$  grown on GaAs substrates, which extends the applications of III-V materials to NIR and SWIR wavelength range. The  $\text{GaAs}_{1-x}\text{Bi}_x$  ternary material was first grown by Oe *et al.* using metal organic vapor phase epitaxy (MOVPE) in 1998 [17] and by Tixier *et al.* using MBE in

2003 [18], followed by a few of related works [19-29]. Recently, the GaAs lattice-matched GaNAsBi and BGaAsBi quaternary materials have been grown on GaAs substrates, which considerably extend the widespread use of GaAs-based bismide in long wavelength and solar cell devices [30-32].

In addition, InGaAsBi quaternary material has been proposed for MWIR applications and has been grown on InP substrates using MBE [33-35]. GaSbBi ternary material has been grown using liquid phase epitaxy (LPE) [36] and MBE [37,38]. Meanwhile, GaInAsSbBi quaternary material has been demonstrated by Sinel'nikov *et al.* on InSb substrates using temperature gradient float zoning [39]. The development of all abovementioned III-V bismide materials and their related applications are summarized in Table 1.1. In this work, aiming at the applications of III-V bismide materials in MWIR laser diodes and SWIR temperature insensitive laser diodes, we focus on the exploration of the GaSb-based GaInAsSbBi material and the GaAs-based GaAsBi material.

Table 1.1 Summary of the III-V bismide materials used for IR optoelectronics applications.

Substrate	SWIR	MWIR	LWIR
InP	-	InGaAsBi	GaInSbBi
InAs	-	-	InAsBi, InAsSbBi
InSb	-	-	InSbBi, InAsSbBi GaInAsSbBi
GaSb	-	GaSbBi, GaInAsSbBi	-
GaAs	GaAsBi, GaNAsBi, BGaAsBi	-	-

## 1.1 GaSb-based GaInAsSbBi MWIR laser diodes

Semiconductor MWIR laser diodes are highly attractive for gas sensing and environmental monitoring because many industrially and environmentally important gases have absorption lines within the 2-4  $\mu\text{m}$  wavelength region as shown in Table 1.2 [40,41]. Moreover, there is a water-absorption-free atmospheric transparency window in 3.5-4  $\mu\text{m}$ , which means such MWIR laser diodes have much potential to be used in free-space telecommunication and light detection and ranging (LIDAR).

Table 1.2 Toxic gases with absorption lines in the MWIR range

Gas	Wavelength ( $\mu\text{m}$ )
Methane	2.3, 3.3
ethylene	3.17
acetone	3.4
Nitrogen dioxide	3.9, 4.5
Sulfurous anhydride	4.0
Carbonic gas	4.27

Compared with other technologies, room temperature (RT) continuous wave (CW) operational GaSb-based type-I quantum well (QW) InGaAsSb laser diodes are the most promising candidates for MWIR lasers in the 2-4  $\mu\text{m}$  wavelength range because of the intrinsic advantages of the type-I active region designs [42,43]. High performance RT CW operational GaSb-based laser diodes have been demonstrated in the 2-3  $\mu\text{m}$  range in the last decade [44-49]. A lot of effort has been exerted to extend the wavelength beyond the 3  $\mu\text{m}$  bound using the

GaSb-based technology. However, the progress has been very slow, as summarized in the development track in Fig. 1.3 [42,43,50-58]. Since the first 3.04  $\mu\text{m}$  laser diode demonstrated by Lin *et al.* in 2004, the wavelength record has been extended at an average speed of less than 100 nm per year. Until recently have the 3.58  $\mu\text{m}$  and 3.73  $\mu\text{m}$  laser diodes been demonstrated by Vizbaras *et al.* in 2011 and 2012 respectively.

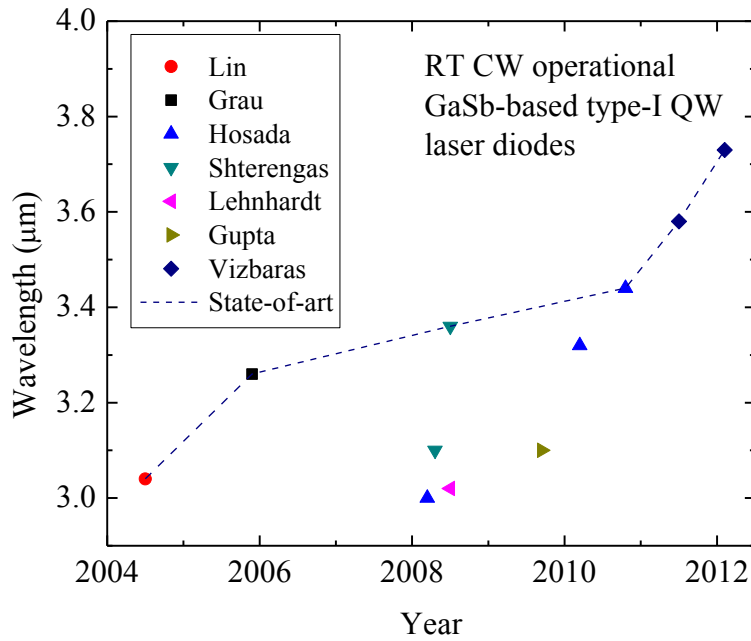


Fig 1.3 Development of GaSb-based type-I QW Mid-IR laser diodes in 3-4  $\mu\text{m}$  in last decade. The dashed line shows the state-of-art record of lasing wavelength of each year.

The slow progress reflects the increasing difficulties in extending the wavelength beyond 3  $\mu\text{m}$ . In this wavelength range, hole confinement is regarded as the most decisive factor to the performance of the GaSb-based laser diodes [52]. However, high In composition in the QW regions results in reduced hole confinement or even type-II band alignment, significantly deteriorating the performance of the laser devices. In order to improve the hole confinement, the

complex quinary AlGaInAsSb material have to be used in the barrier layers. Nevertheless, the growth of InGaAsSb QWs and AlGaInAsSb barriers with high In composition is not only plagued by the large miscibility gap of the alloys [60], but also by the thermally instability due to in-situ annealing effect during the growth [61]. Consequently, the development of the GaSb-based laser diodes is challenged by the intrinsic material growth issues as well as the device design issues [62].

In this work, a new 3-4  $\mu\text{m}$  GaSb-based type-I QW laser diode design has been proposed with the novel GaInAsSbBi material to be employed in the QW regions to replace the conventional InGaAsSb material. The bandgap and valance band maximum (VBM) is expected to be considerably reduced and raised respectively due to the incorporation of Bi in the GaInAsSbBi material. The unique capabilities of the III-V bismide material can bring several remarkable benefits compared with the conventional designs using InGaAsSb QW regions. First of all, our design not only effectively extends the wavelength up to 4  $\mu\text{m}$ , but also provides greatly enhanced hole confinement. Secondly, our design significantly reduces the content of In in the QW regions and avoids the alloy grown in the deep miscibility gap. Thirdly, our design only uses quinary GaInAsSbBi material in the thin QW regions (in tens of nanometers) hence prevents growing the thick lattice matched quinary AlGaInAsSb in the barrier layers (in hundreds of nanometers), which considerably simplifies the complexity of the material growth. Meanwhile, quasi-Al free laser diodes are possible to be achieved using the GaInAsSbBi/GaSb active regions and InGaAsSb cladding layers, which can intrinsically improve the reliability of the laser diodes. The proposed GaSb-based type-I QW laser diode designs with the novel GaInAsSbBi material open the opportunities to fill the 3-4  $\mu\text{m}$  wavelength gap for MWIR imaging, gas sensing, and telecommunication applications.



## 1.2 GaAs-based GaAsBi temperature insensitive IR laser diodes

In the present SWIR InGaAsP/InP laser diode used for telecommunication applications, the current threshold and the slope efficiency decrease dramatically as the increase of the temperatures [63,64]. At constant bias current, the optical output decreases as the increase of the temperature [63,64].

In order to address the challenges brought by the temperature dependent characteristics of such laser diodes, thermo-electric coolers (TECs) have been assembled into the laser diode assemblies to keep the laser diodes working at a steady temperature thus to stabilize the threshold current and the optical power output. However, the TECs not only largely increase the size, weight and cost of the laser diode assemblies, but also tremendously raise the energy consumption level of the assemblies. As an example, in a typical InGaAsP laser diode assembly, 10 mW is utilized by the laser diode to achieve lasing operation while 600 mW is consumed by the TEC to maintain the operation temperature [65]. The TEC consumes 30 times more power than the laser diode, which is a striking loss of the power efficiency.

The temperature dependence of the current threshold of the laser diodes is mainly caused by the conduction-heavy hole and split-off hole-heavy hole (CHSH) Auger process in the active region of the laser diodes, which is a non-radiative process and is very temperature sensitive [65,66]. In the CHSH process, energy released from recombination of an electron in the conduction band and a hole in the valence band excites an electron from the split-off band to the heavy hole band, as shown in Fig 1.4(a). It is alluring to suppress the CHSH Auger combination by engineering the bandgap and the spin-orbit splitting energy ( $\Delta_{SO}$ ) of the QW region material in the laser diodes to achieve the temperature insensitive characteristic.

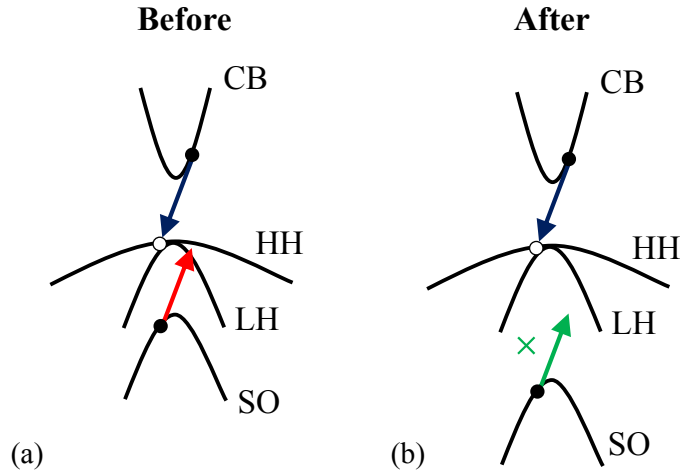


Fig. 1.4 (a) Schematic of the CHSH Auger process, (b) schematic of the suppression of the CHSH Auger process in the proposed GaAsBi alloys.

In GaAsBi material, the bandgap and the spin-orbit splitting energy ( $\Delta_{SO}$ ) can be engineered in a wide range, which makes a temperature insensitive laser diode of great possibility. The bandgap of GaAsBi material decreases dramatically as the increase of Bi composition ( $\sim 88$  meV/Bi%) [21]. A mechanism used to describe how Bi modifies the band structure of GaAs, and that is similar to that of Nitrogen, is the band anti-crossing model [67-70]. As shown in Fig. 1.5, the Bi 6p energy level is 80 meV below the VBM of GaAs. The resonant interaction between the Bi 6p level and the VBM of GaAs results in a narrower bandgap as the VBM is pushed up.

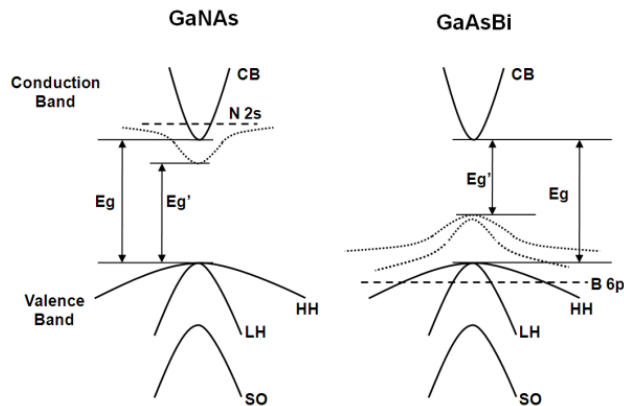


Fig. 1.5 Schematics of the band anti-crossing model for the GaAsN and GaAsBi.

Meanwhile, the  $\Delta_{SO}$  of GaAsBi material increases significantly as the increase of the Bi composition [71-75]. This is due to the large  $\Delta_{SO}$  of GaBi, as shown in Fig 1.6 [76]. Compared with the  $\Delta_{SO}$  of GaAs (0.34 eV), the  $\Delta_{SO}$  of GaBi is much bigger (2.15 eV) [76].

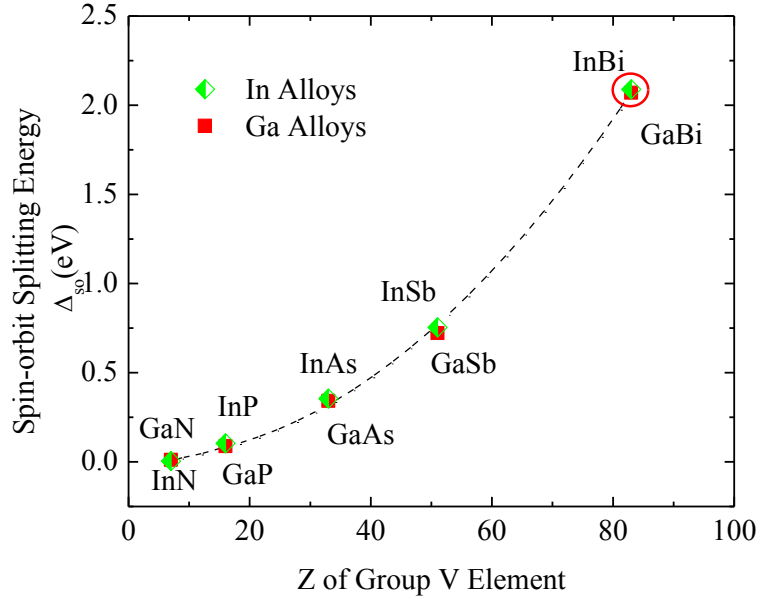


Fig 1.6 Spin-orbit splitting energy of Ga and In containing binary alloys, showing the bismide alloys possessing significantly higher spin-orbit splitting energies than other binary alloys.

As a result, when the Bi composition exceeds ~10.5% in GaAsBi material, the bandgap is in SWIR range and the  $\Delta_{SO}$  can be larger than the bandgap [74,75], as shown in Fig. 1.7. It also has been experimentally proven that the CHSH Auger process can be suppressed in such high Bi composition GaAsBi [75,77]. Therefore, when GaAsBi material is used in the QW region of the laser diodes in SWIR range, the CHSH Auger recombination process is expected to be effectively suppressed to realize the temperature insensitive laser diodes [65].

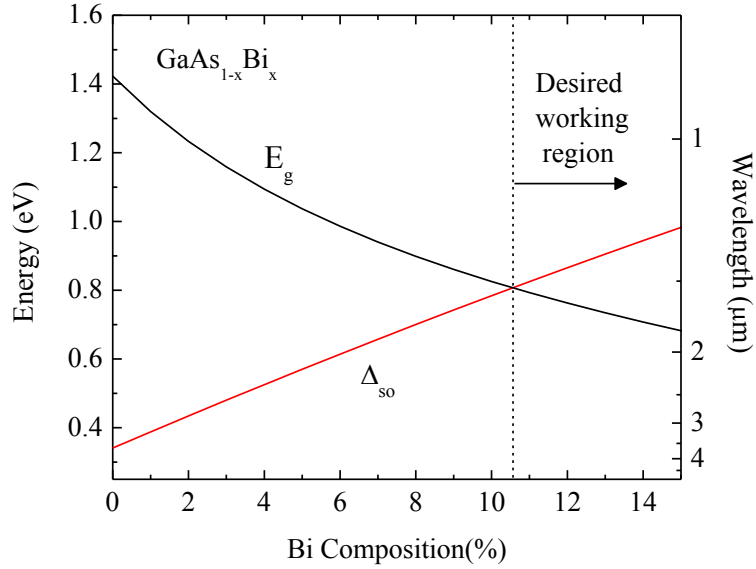


Fig. 1.7 Bandgap and spin-orbit splitting energy of GaAsBi alloys as a function of Bi composition, showing the spin-orbit splitting energy exceeds the bandgap at Bi composition of around 10.5%.

Since the debut of GaAsBi material in 1998, it has been systematically studied in the last decade. Unlike GaAs material, GaAsBi material is best grown at low temperatures from 280 °C to 400 °C and at low arsenic overpressure. GaAsBi bulks, GaAsBi/GaAs QWs and GaAsBi/AlGaAs superlattices have been developed using MBE and MOVPE by many groups [17-29, 78-81]. Bi composition is fit using high resolution x-ray diffraction (HRXRD) which is calibrated by Rutherford backscattering spectrometry (RBS) [82-84]. Among these works the highest Bi composition is reported as ~11% [24]. The optical properties of the alloys have been extensively investigated using PL and photoreflectance (PR) [85-87] and type-I band alignment between GaAs and GaAsBi material has been experimentally confirmed [75,86,88].

Moreover, it has been reported that the temperature dependence of the PL peak energy of GaAsBi material is only 1/3 of that of the GaAs material [89-92]. It is interpreted as the

combination of the negative gap-efficient semiconductor (GaAs) and the positive gap-efficient semimetal (GaBi) [93].

Carrier transport properties of the GaAsBi alloys have been studied using Hall measurement and time-resolved terahertz spectroscopy [94-99]. The electron and hole mobility of GaAsBi alloys are only slightly degraded by the incorporation of the Bi atoms, which suggests that the GaAsBi alloys are suitable to be used in applications demanding high performance optoelectronic devices.

In the device fabrication aspect, LEDs and optically pumped lasers have been successfully demonstrated using GaAsBi/GaAs QWs and bulk double heterostructures (DHs) respectively [100-103]. However, electrically pumped RT CW operational laser diodes have not been realized yet. The development of the GaAsBi optoelectronic devices is bottlenecked by the lack of high quality separate confinement heterostructures (SCHs) which may make the electrical pumped laser diodes possible. The growth of GaAsBi/GaAs/AlGaAs SCHs is challenged by the incompatibility of the optimal growth temperatures of the AlGaAs barriers ( $\sim 610$  °C) and the optimal growth temperatures of GaAsBi QWs ( $\sim 300$  °C). A solution is highly desired to promote the development of GaAsBi/GaAs optoelectronic devices.

In this work, we systematically study the MBE growth of GaAsBi material and investigate the effects of Bi atoms in the growth. The morphological, structural and optical properties of the GaAsBi bulk and QW samples are thoroughly analyzed using atomic force microscopy (AFM), PL, HRXRD, transmission electron microscopy (TEM) and energy dispersive X-ray spectroscopy (EDS). Furthermore, we propose Bi surfactant mediated growth of high quality AlGaAs barriers at low temperatures around 300 °C and successfully obtain the high quality

GaAsBi/GaAs/AlGaAs single quantum well (SQW) and double quantum well (DQW) SCHs. The surfactant effect of Bi is evidenced by the presence of a  $(1 \times 3)$  surface reconstruction throughout the growth of the upper AlGaAs barriers at low temperatures. The growth of the high quality DQW SCH integrates the DQW and SCH designs into the GaAsBi/GaAs device structure and enables the further development of GaAsBi/GaAs material system towards high performance optoelectronic devices.

### **1.3 Scope of this dissertation**

This dissertation begins with the modeling of novel GaInAsSbBi quinary material used in GaSb-based type-I QW MWIR laser diodes in 3-4  $\mu\text{m}$  wavelength range. Thermophotovoltaic (TPV) devices using lattice-matched GaInAsSbBi material are proposed as well. The experimental techniques using MBE and surfactant mediated growth are discussed in Chapter 3. The material growth of GaAsBi/GaAs bulks and QWs is explored in Chapter 4 in detail. The extensive characterization of the bulk and QW samples using AFM, TEM, HRXRD, PL, and EDS is also investigated in Chapter 4. The surfactant effect of Bi during the growth of GaAsBi QW samples is thoroughly studied and the acquired knowledge is utilized for the development of high quality GaAsBi/GaAs SCH DQWS, which is further investigated in Chapter 5. In Chapter 6, fabrication of optoelectronic device is discussed and the process and photomask designs are presented. High performance GaAs QW laser diodes demonstrate the excellent quality of the process and mask designs. The last chapter concludes this dissertation and discusses the future works and opportunities enlightened by this work.

## **2 GASB-BASED GAINASSBBI FOR MWIR LASER DIODE AND TPV APPLICATIONS**

### **2.1 GaInAsSbBi for MWIR laser diodes**

In this chapter, the current technologies used in the RT CW operational GaSb-based type-I QW MWIR laser diodes are thoroughly analyzed to figure out the factors that limit the performance of the laser diodes. Accordingly, a new 3-4  $\mu\text{m}$  GaSb-based type-I QW laser diode design is proposed with the novel GaInAsSbBi material to be employed in the QW regions to replace the conventional InGaAsSb materials. The new design possesses tremendous advantages over the conventional designs, such as enhanced hole confinement, extended emission wavelength, eased material growth complexity and elevated device reliability.

#### **2.1.1 InGaAsSb/AlGaAsSb strained QW laser diodes**

A schematic band diagram of a typical type-I InGaAsSb/AlGaAsSb QW laser diode grown on GaSb substrate is shown in Fig. 2.1. In this device, compressively strained InGaAsSb layers sandwiched in AlGaAsSb waveguide layers are used as the active region of the laser diodes. Wide QWs are usually used to lower the quantized energy levels so as to extend the lasing emission wavelength. The InGaAsSb alloy has a direct bandgap for all alloy compositions while The AlGaAsSb alloy has a larger bandgap and lower refractive index than the InGaAsSb alloy. Therefore, lattice-matched AlGaAsSb alloy with low Al composition (25% - 40%) is usually used as the waveguide layers for good carrier confinement and lattice-matched AlGaAsSb with high Al composition ( $\sim 90\%$ ) is usually used as the cladding layers to provide good optical confinement.

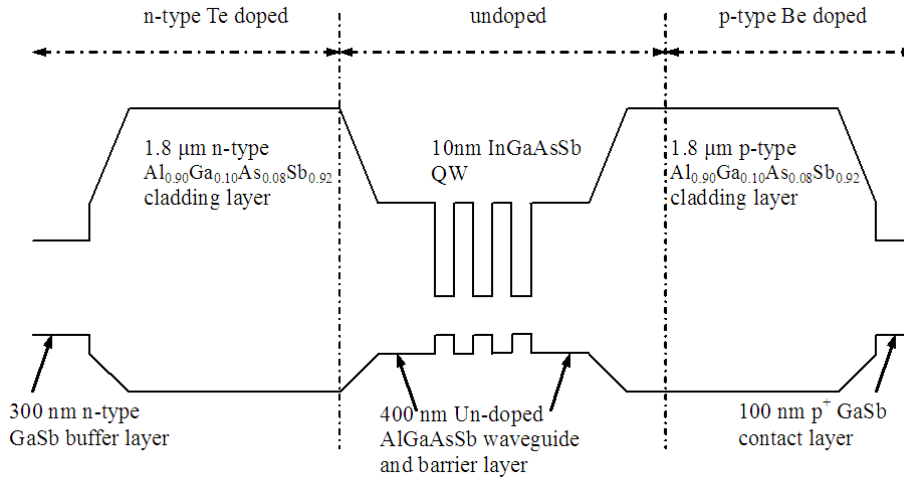


Fig. 2.1 Schematic band diagram of a typical GaSb-based InGaAsSb QW laser diode. The bandgaps and band offsets of the materials are drawn to scale.

The bandgaps of the InGaAsSb alloys lattice-matched with GaSb vary between 0.72 eV (1.72  $\mu\text{m}$ ) and 0.29 eV (4.3  $\mu\text{m}$ ) at RT. However, it remains challenging to achieve such high performance laser diodes in 3-4  $\mu\text{m}$  wavelength range. This is mainly due to the rapid decrease of the valence band offset (VBO) between the InGaAsSb QW regions and the AlGaAsSb waveguide layers. As shown in Fig. 2.2, as the increase of the lasing wavelength, the VBM of InGaAsSb material decrease dramatically, which leads to insufficient hole confinement. As a result, when the VBM of AlGaAsSb barrier layer is decreased by increasing the Al composition to keep the hole confinement, the conduction band discontinuity will be increased more rapidly since the energy bandgap offset between InGaAsSb and AlGaAsSb occurs mostly in the conduction band.



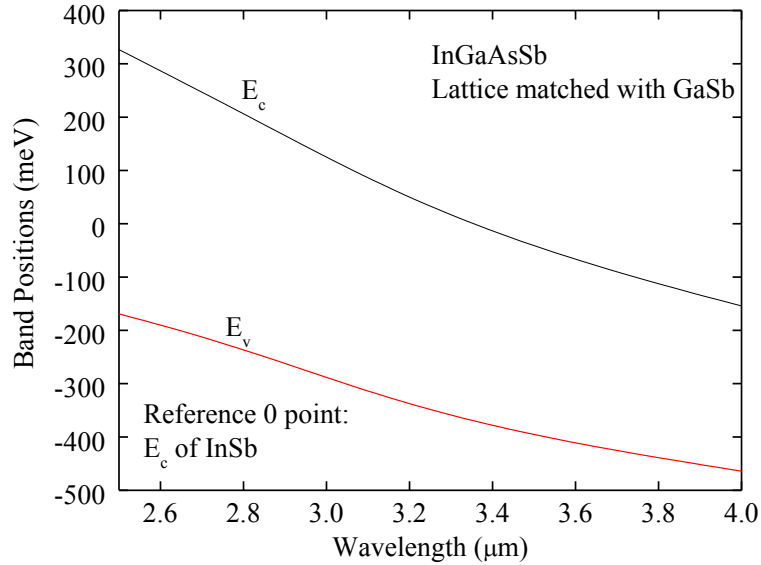


Fig. 2.2 Band positions of lattice-matched InGaAsSb as a function of wavelength.

The valence band of InSb is used as the reference position. The VBM of InGaAsSb decreases dramatically as the increase of wavelength.

As an example, the electron confinement and hole confinement between  $\text{In}_{0.5}\text{Ga}_{0.5}\text{As}_{0.23}\text{Sb}_{0.77}$  QWs (with 1.5% compressive strain) and lattice matched AlGaAsSb barriers are displayed in Fig 2.3 [104]. This structure is also used in work [50] to achieve the lasing wavelength of 3.04 μm. It can be clearly seen that the electron confinement rises much faster than the hole confinement with increasing Al composition in the AlGaAsSb barrier layers. When Al composition is at 30%, the hole confinement is relatively small (64 meV) while the electron confinement is much bigger (655 meV) than the optical transition of the laser diode (408 meV).

Since the major bandgap offset between the InGaAsSb QW regions and the AlGaAsSb barriers lies in the conduction band side, the performance of the laser devices are deteriorated by the serious electron inhomogeneous injection and the hot electron injection. In addition, the

increase of Al composition in AlGaAsSb barrier layer can lead to the decrease of the waveguide refractive index, reducing the optical mode confinement of the devices.

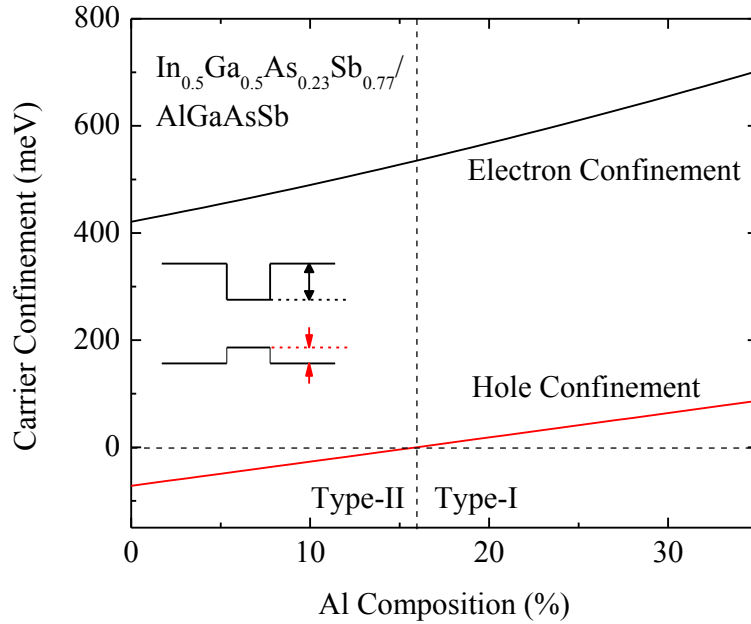


Fig. 2.3 Carrier confinement between the  $\text{In}_{0.5}\text{Ga}_{0.5}\text{As}_{0.23}\text{Sb}_{0.77}$  QW regions and the lattice-matched AlGaAsSb barriers. As the increase of Al composition, the electron confinement rises much faster than the hole confinement does.

### 2.1.2 Current solution: Quaternary AlGaInAsSb barriers

The current solution for the poor hole confinement is to use quaternary AlGaInAsSb material to replace the quaternary AlGaAsSb material in the barrier layers [43,52-59]. This approach means to lower the VBM of the barrier layer so that the hole confinement can be improved without the penalty of significantly increased electron confinement. Meanwhile, the quaternary barrier lowers the In composition gradient at the well-barrier interface and thus reduces the intermixing between the well and barriers. With this quaternary barrier layer, the wavelength has been extended from  $3.1 \mu\text{m}$  [51] to  $3.73 \mu\text{m}$  [43].

Although this solution sounds encouraging, the demonstrated device performance such as the peak output power  $P_{\max}$  and characteristic temperature  $T_0$  are still poor because of a series of fundamental issues:

1) Insufficient hole confinement: Poor hole confinement is a major issue for InGaAsSb/AlGaInAsSb material system and a decisive factor to the performance of the laser devices. The shallow hole well structure can easily cause many problems such as reduced material gain (due to small wave function overlap), low injection efficiency (due to hole leakage and thermionic escaping from the well), increased free carrier absorption under high injection (due to accumulated carriers in the waveguide layer), and increased Auger recombination (due to increased carrier density in QWs to obtain threshold gain) to dramatically deteriorate the device performance.

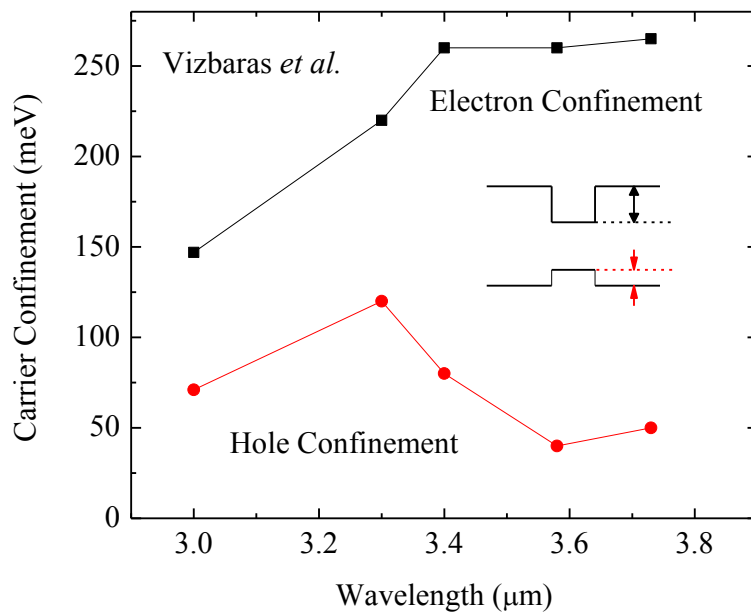


Fig. 2.4 Electron and hole confinement of InGaAsSb/AlGaInAsSb active regions in the RT CW operational laser diodes made by Vizbaras *et al.*. As the increase of wavelength, there is a clear trend of decreased hole confinement.

Fig. 2.4 shows the hole confinement of InGaAsSb/AlGaInAsSb active region in the RT CW operational laser diodes working at different emission wavelengths, which have been demonstrated by a prominent group in this area who holds the world record of lasing wavelength since 2011 [43]. Even with the advanced quaternary barrier technology applied in the device designs, the hole confinement still keeps at a very low level. At the wavelength of 3.58  $\mu\text{m}$  and 3.73  $\mu\text{m}$ , the hole confinements are 40 meV and 50 meV respectively, which are insufficient for enhanced performance.

2) Limited lasing wavelength: The decrease of the hole confinement as the increase of the lasing wavelength shown in the Fig 2.4 suggests the hole confinement will be even smaller than 50 meV when the lasing wavelength exceeds 3.73  $\mu\text{m}$ . The lack of hole confinement could limit the development of GaSb-based type-I QW laser diode working at a longer wavelength. Moreover, InGaAsSb quaternary alloys with high In composition has become difficult to grow because the alloys become metastable due to a miscibility gap of In composition between 0.18 to 0.84 [60]. In addition, it has been reported that the InGaAsSb alloys with high In compositions are thermally unstable and show blue-shifting of wavelength during the in-situ annealing [61]. As shown in Fig. 2.5, the current solutions of extending the lasing wavelength are at the expense of pushing the InGaAsSb alloys deeper into the miscibility gap, which greatly increases the growth complexity and possibly brings serious reliability issues. For example, the current world record 3.73  $\mu\text{m}$  laser diode is achieved by using  $\text{Ga}_{0.28}\text{In}_{0.72}\text{As}_{0.44}\text{Sb}_{0.56}/\text{Al}_{0.3}\text{Ga}_{0.2}\text{In}_{0.5}\text{As}_{0.46}\text{Sb}_{0.54}$  active region, in which not only the QW regions use the highest reported In composition (72%) but also the barrier layers use high In composition (50%). The In compositions in the QWs and barriers are expected to be even higher in the next world record wavelength even though it is doubtful if the associated growth complexity is affordable.

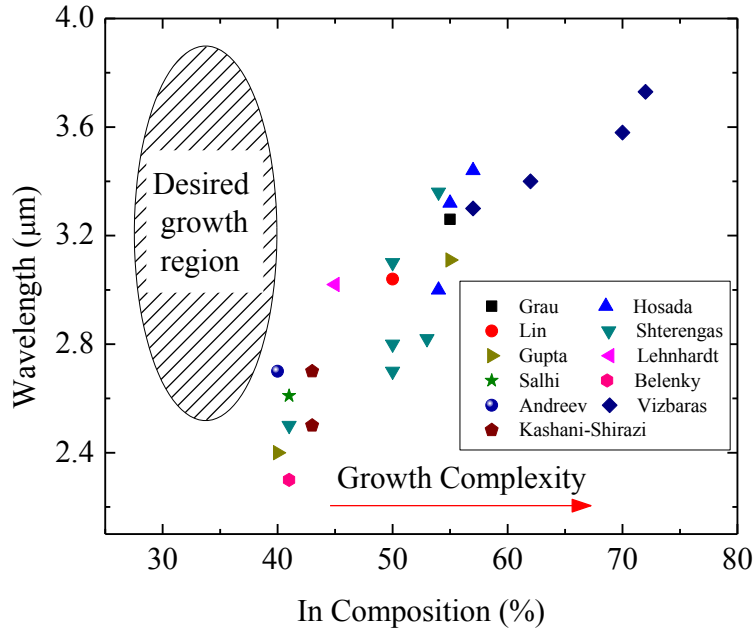


Fig. 2.5 The wavelengths and In compositions of RT CW operational GaSb-based type-I InGaAsSb QW laser diodes. The wavelength is extended at the expense of increasing growth complexity to push the InGaAsSb alloys into deeper miscibility.

3) Potential reliability issue: The laser devices that contain high composition Al in the AlGaAsSb cladding layers tend to be susceptible to performance degradation due to oxidation of the AlGaAsSb layers. After oxidation, the Sb atoms will segregate and form a floating metal thin film [105] which enhances non-radiative recombination and local heating hence probably causes severe reliability problem such as catastrophic optical damage. This restricts the devices within low power sensing applications and limits their high power applications.

In general, the approach using quinary barrier layers have successfully pushed the lasing wavelength from 3.1 μm to 3.73 μm. However, it haven't perfectly solved the preexisting issues for example the lack of hole confinement and limited lasing wavelength. A new approach is desperately expected to address these issues to make the devices working in longer wavelengths.

### 2.1.3 Our approach: Quinternary GaInAsSbBi QWs

In this work we propose a novel GaSb-based GaInAsSbBi alloy to be used in the QW region which offers extended wavelengths and enhanced hole confinement. In previous GaAsBi works, the effect of Bi in GaAsBi alloys is interpreted by the band anti-crossing model that the resonant interaction between the Bi 6p level and the VBM of GaAs results in reduced bandgap as the VBM is pushed up, as shown in Fig. 1.4. Since the Bi 6p level is below all of the VBMs of GaAs, GaSb, InAs, and InSb (see Fig. 2.6) [68], it is expected that a similar bandgap reduction and VBM uplifting would occur when Bi is added to the GaInAsSb material system. In 2012, GaSbBi has been successfully grown by Das *et al.* using LPE and by Song *et al.* using MBE [36,37]. It also has been confirmed that adding a small amount of Bi reduces the bandgap of the GaSb effectively [36]. InAsBi and InSbBi alloys have also been investigated as promising narrow bandgap materials [11-14]. Therefore, it is worthy to explore the capability of InGaAsSbBi alloys towards the applications for long-wavelength optoelectronic devices.

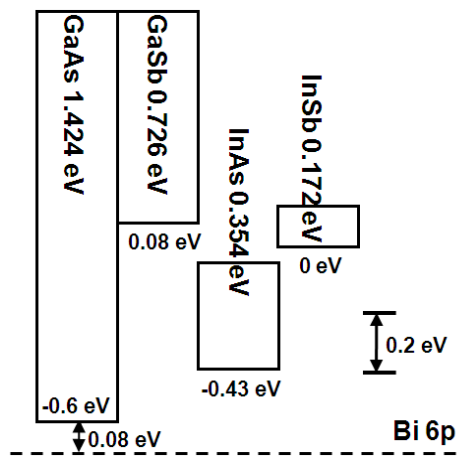


Fig. 2.6 Bi 6p energy level relative to the band alignments of GaAs, GaSb, InAs, and InSb.

The bandgap energies of GaSb-lattice-matched GaInAsSbBi are calculated by using a biquadratic interpolation algorithm proposed by Donati *et al.* in 2003 [106]. In this interpolation, the GaInAsSbBi can be denoted as  $\text{Ga}_x\text{In}_{1-x}\text{Sb}_y(\text{As}_z\text{Bi}_{1-z})_{1-y}$ , as shown in Fig. 2.7.

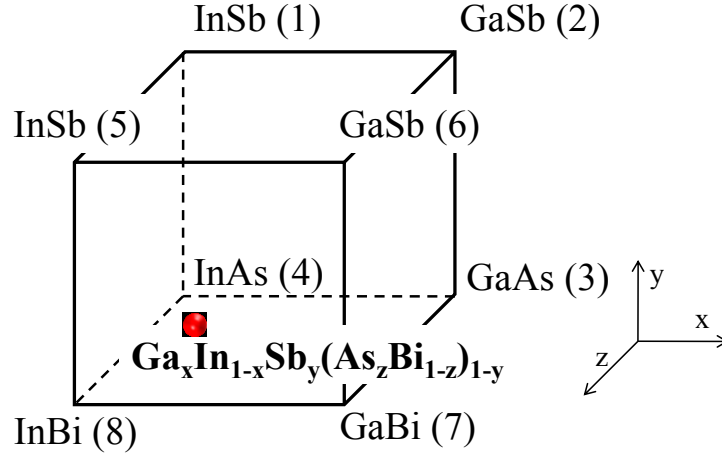


Fig. 2.7 Schematic of the bandgap interpolation of  $\text{Ga}_x\text{In}_{1-x}\text{Sb}_y(\text{As}_z\text{Bi}_{1-z})_{1-y}$  alloys.

When the GaInAsSbBi alloys are lattice-matched with GaSb substrates, the relationship between the material compositions can be calculated by using Vegard's law:

$$z = \frac{0.5901 - 0.362x - 0.2066y - 0.0215xy}{(0.6277 + 0.04305x)(1 - y)} \quad (2.1)$$

The bandgap of the  $\text{Ga}_x\text{In}_{1-x}\text{Sb}_y(\text{As}_z\text{Bi}_{1-z})_{1-y}$  alloys can then be obtained by a third rank tensor contraction which is given by:

$$E_g(x, y, z) = P_{ijk} \mathbf{x}^i \mathbf{y}^j \mathbf{z}^k \quad (2.2)$$

Where  $P_{ijk}$  contains 27 components, including 8 binary values of the III-V material, 12 ternary bowing coefficients, 6 quaternary bowing coefficients and 1 quinary bowing coefficient. The material parameters and bowing coefficients used in this model are listed in

Table 2.1[2,106]. The bowing coefficients are taken as zeros for the III-V bismide materials such as InAsBi, InSbBi, GaAsBi, GaSbBi, InGaSbBi, InGaAsBi, GaAsSbBi, and InAsSbBi, since there is no such set of data available so far. The model can be promisingly improved when these parameters are fit from experiments in the future.

Table 2.1 Bandgaps of binary alloys and bowing coefficients used in the  $Ga_xIn_{1-x}Sb_y(As_zBi_{1-z})_{1-y}$  interpolation [2,106]. (Unit: eV)

B1, B5 (InSb)	0.172	C12,C56	-0.415	C37	0	D1234	-0.01
B2, B6 (GaSb)	0.726	C23	-1.43	C48	0	D1256	0
B3 (GaAs)	1.424	C34	-0.477	C67	0	D2673	0
B4 (InAs)	0.354	C14	-0.67	C78	0	D3487	0
B7 (GaBi)	-1.45	C15	0	C58	0	D1485	0
B8 (InBi)	-1.63	C26	0	D5678	0	E	0

The VBOs of  $Ga_xIn_{1-x}Sb_y(As_zBi_{1-z})_{1-y}$  alloys are calculated using linear interpolation approach. The VBOs the binary alloys used in this work are listed in Table 2.2 [2,3]. The VBO of InBi is not available yet so it is taken as the same value as GaBi for 0.8 eV.

Table 2.2 VBOs of the binary alloys used in the linear interpolation of  $Ga_xIn_{1-x}Sb_y(As_zBi_{1-z})_{1-y}$ .

Material	VBO (eV)	Material	VBO (eV)
InSb	0	InAs	-0.59
GaSb	-0.03	GaBi	0.8
GaAs	-0.80	InBi	0.8



Fig. 2.8 shows the optical transition wavelength contours of GaInAsSbBi QWs with 1.5% compressive strain to GaSb substrates at different In and Bi compositions. For a given wavelength in this figure, the In composition decreases dramatically as the increase of Bi composition. For instance, when there is no Bi introduced, nearly 80% In composition is required to achieve the optical transition wavelength of 4.0  $\mu\text{m}$ . However, when 10% Bi composition is used in the alloys, less than 40% In composition is needed to realized the same 4.0  $\mu\text{m}$  optical transition wavelength, which greatly lower the growth complexity caused by growing the high In composition alloys in the miscibility gap. Compared with the bandgap reduction mechanism in InGaAsSb which is mainly due to the narrow bandgaps of InAs (0.417 eV) and InSb (0.236 eV), the bandgap reduction mechanism in GaInAsSbBi is primarily due to the negative bandgaps of the semimetal materials GaBi and InBi, which are -1.45 eV and -1.55 eV respectively [3,67,68].

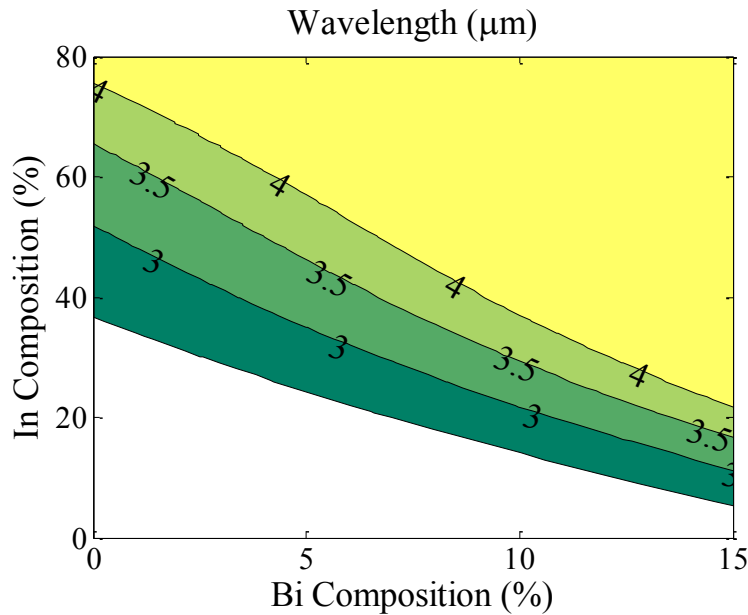


Fig. 2.8 Optical transition wavelength contours of GaInAsSbBi QWs (with 1.5% compressive strain) at different In and Bi compositions. For a given wavelength, In composition decreases dramatically as Bi composition increases.

In previous works, GaAsBi material with more than 10% Bi composition has been successfully demonstrated using MBE growth [24]. It is expected to obtain even higher Bi composition in the GaInAsSbBi alloys since the difference in the atom radius of Bi and Sb is smaller than that of Bi and As. Therefore, GaInAsSbBi material is a more promising candidate to extend the light emission wavelength up to 4  $\mu\text{m}$ .

More importantly, the proposed GaInAsSbBi alloys can substantially improve the VBOs of the QW regions. Fig. 2.9 displays the contour plot of VBOs of the GaInAsSbBi QWs with 1.5% compressive strain to GaSb substrates. The VBOs are improved considerably as the decrease of In composition and the increase of Bi composition.

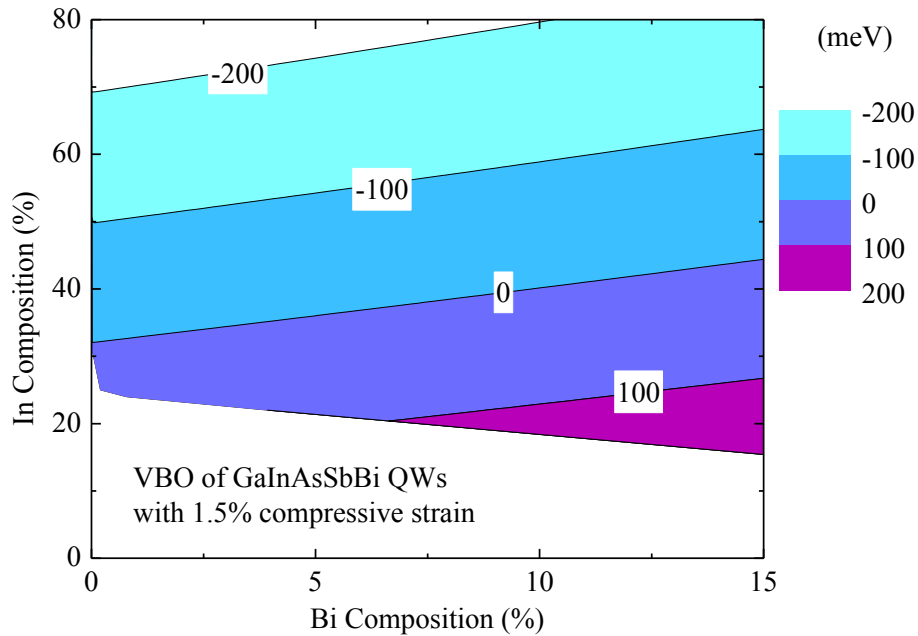


Fig 2.9 Contour plot of VBOs of GaInAsSbBi QWs with 1.5% compressive strain, showing the considerable increase of VBO as the decrease of In composition and the increase of Bi composition.

Fig 2.10 shows the As composition and VBO in the GaInAsSbBi QWs with 1.5% compressive strain and 4  $\mu\text{m}$  optical transition wavelength. As can be seen, the increase of Bi composition reduces the As composition significantly. This is because Bi is more effective than In in reducing the bandgaps of GaInAsSbBi alloys. When Bi composition is increased, much lower In composition is required in order to achieve the 4  $\mu\text{m}$  optical transition wavelength. Hence, much lower As is required to meet the constraint of lattice constant (1.5% compressive strain to GaSb). The reduction of As composition consequently results in the enhancement of the VBO of the alloys since the antimonide and bismide alloys have much larger VBOs than those arsenide alloys, as shown in Table 2.2.

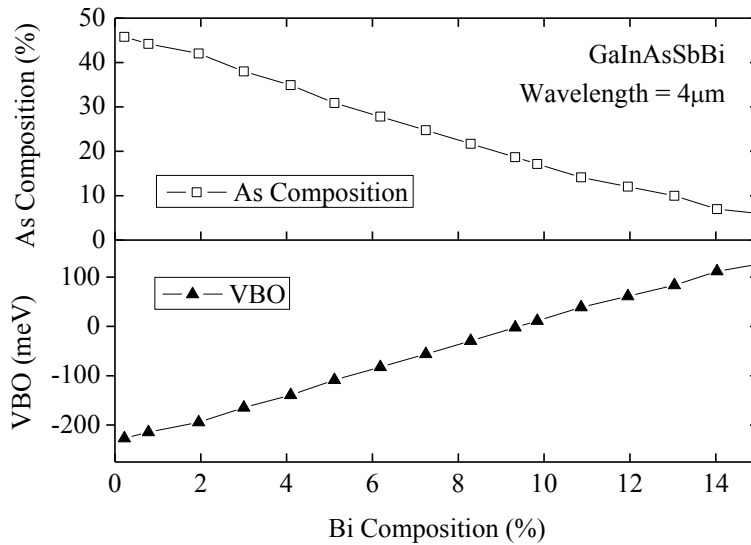


Fig. 2.10 As composition and VBO as a function of Bi composition in the GaInAsSbBi QWs with 1.5% compressive strain and 4  $\mu\text{m}$  optical transition wavelength.

When lattice-matched AlGaAsSb is used as the barrier layers in the active regions of MWIR laser diodes, a much enhanced hole confinement and a balanced hole-electron confinement can be achieved in a wide Al composition range. Fig. 2.11 shows the carrier confinement between

the  $\text{Ga}_{0.7}\text{In}_{0.3}\text{As}_{0.11}\text{Sb}_{0.77}\text{Bi}_{0.12}$  QWs (with 1.5% compressive strain) and the lattice-matched AlGaAsSb barrier layers. Compared with the band alignment of InGaAsSb/AlGaAsSb in Fig. 2.3, the band alignment of this active region is type-I in full Al composition range. Better confinement can be obtained even at low Al composition. For instance, 10% Al composition in the AlGaAsSb barrier gives a 142 meV hole confinement and a 388 meV electron confinement, which is much improved by  $\sim 100$  meV for hole confinement compared with the world record devices using InGaAsSb/AlInGaAsSb active regions ( $\sim 50$  meV at  $3.73 \mu\text{m}$ ) as shown in Fig. 2.4.

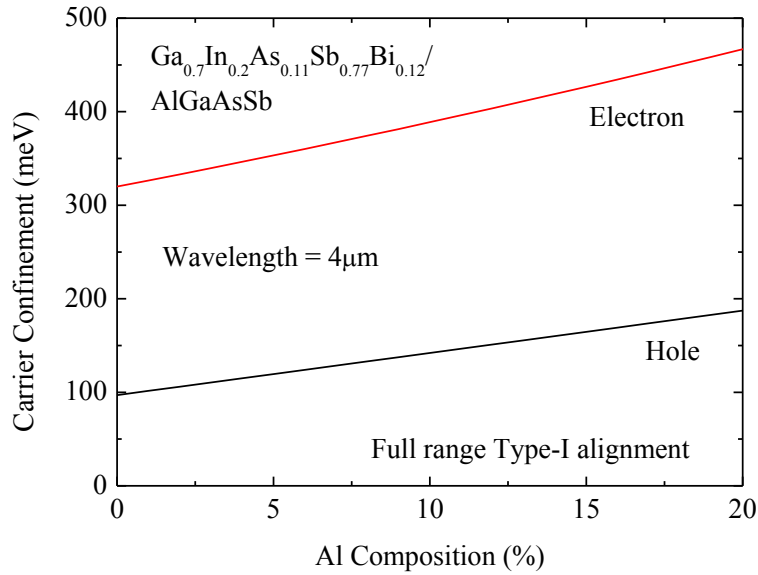


Fig. 2.11 Carrier confinement between  $\text{Ga}_{0.7}\text{In}_{0.3}\text{As}_{0.11}\text{Sb}_{0.77}\text{Bi}_{0.12}$  QW and lattice-matched AlGaAsSb barrier layer. The QW region has 1.5% compressive strain and the expected wavelength is  $4 \mu\text{m}$ . Balanced electron-hole confinement is obtained in a large Al composition range.

It's very interesting to note that in Fig 2.11 when the Al composition is zero the carrier confinement represents the type-I band alignment between the GaInAsSbBi QW regions and the GaSb barrier layers. The hole confinement and electron confinement are well balanced at 97

meV and 320 meV respectively. By achieving this, the Al-free active region is realized, which has been desired for a long time and until now only has been demonstrated at the emission wavelength of 3.04  $\mu\text{m}$  using InGaAsSb/GaSb active region design [50]. Fig. 2.12 shows the carrier confinements of GaInAsSbBi/GaSb active regions with 4  $\mu\text{m}$  optical transition wavelength and 1.5% compressive strain in the QWs. Type-I alignment is achieved when the Bi composition exceeds 8% and the carrier confinement can be controlled by varying the Bi composition. As a result, the design and growth of the laser structure have been greatly simplified by adopting these binary barrier layers.

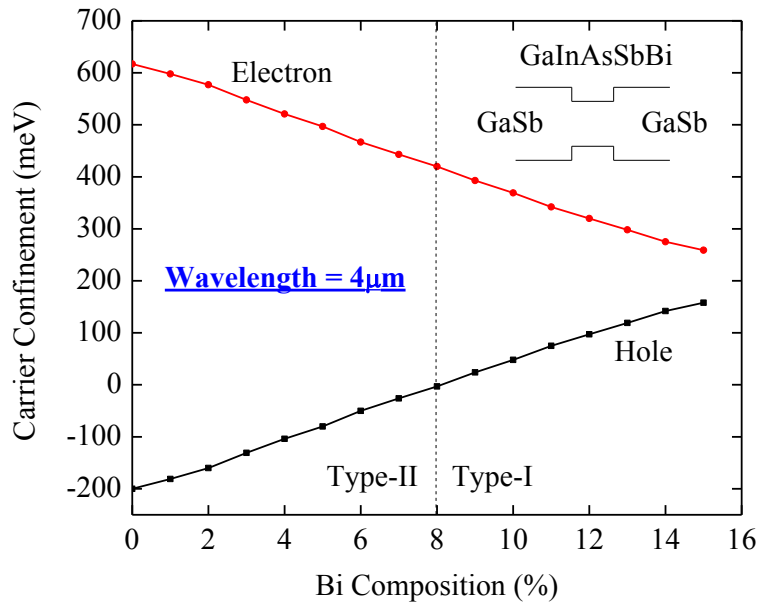


Fig. 2.12 Carrier confinements of GaInAsSbBi/GaSb active regions with 4  $\mu\text{m}$  optical transition wavelength and 1.5% compressive strain in the QWs. Type-I band alignment is achieved in the Al-free active region when Bi composition exceeds 8%.

Fig. 2.13 shows an example of the laser diode band structure design using the proposed Al-free GaInAsSbBi/GaSb active region. Only one QW region is drawn in the diagram for

illustrative purpose. The QW region uses  $\text{Ga}_{0.76}\text{In}_{0.24}\text{As}_{0.07}\text{Sb}_{0.79}\text{Bi}_{0.14}$  alloy with 1.5% compressive strain and the optical transition wavelength is 4  $\mu\text{m}$ . GaSb (with large refractive index) is used as the waveguide layers and the narrow bandgap  $\text{In}_{0.3}\text{Ga}_{0.7}\text{As}_{0.26}\text{Sb}_{0.74}$  (with small refractive index) is used as the cladding layers. The  $\text{In}_{0.3}\text{Ga}_{0.7}\text{As}_{0.26}\text{Sb}_{0.74}$  and GaSb layers have type-II band alignment and therefore a thin layer of  $\text{Al}_{0.2}\text{Ga}_{0.8}\text{As}_{0.02}\text{Sb}_{0.98}$  is inserted for an enhanced carrier confinement in the waveguide layers, which helps to realize the “Quasi-Al-free” design in the laser structure. The optical confinement calculation using the RSoft software indicates good optical confinement of the laser structure, as displayed in Fig. 2.14. This design only requires the growth of binary GaSb material for waveguide layers, which not only significantly simplifies the MBE growth but also improves the material quality of the layers due to its ease of growth. Moreover, no Al is used in the active region and in cladding layers and only two thin layers of AlGaAsSb are used as the carrier barriers where the optical field intensity is weak, which prevents device failures caused by the oxidation of high Al composition AlGaAsSb layers. The device reliability is thus expected to be substantially improved by such quasi-Al-free design compared with the existing InGaAsSb/AlGaInAsSb QW lasers.

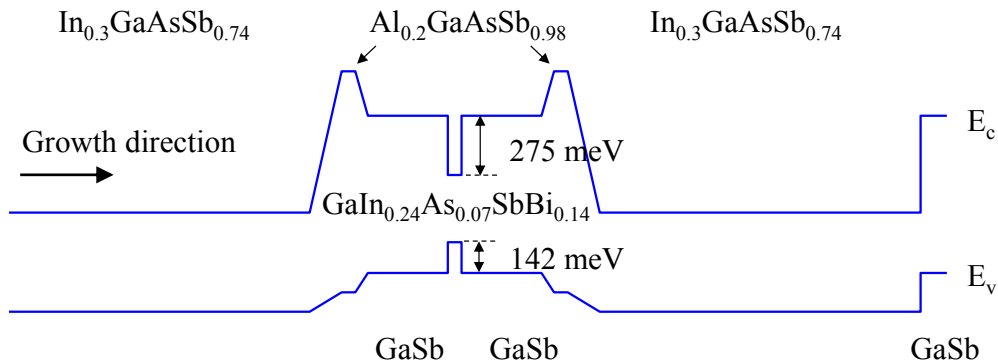


Fig. 2.13 Laser structure design with 1.5% strain in the GaInAsSbBi QW region.

The optical transition wavelength is 4  $\mu\text{m}$ .

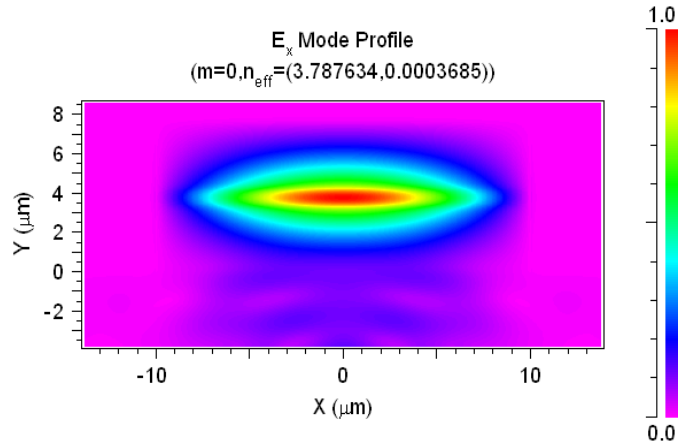


Fig. 2.14 Good optical confinement of the proposed laser structure shown in Fig. 2.13 calculated by using Rsoft software.

In summary, the GaSb-based quinary GaInAsSbBi alloys are really promising candidates to be used in the QW regions to realize high performance 3-4  $\mu\text{m}$  MWIR laser diodes. Compared with the currently technologies using quinary AlGaInAsSb barriers, our proposed technology has several distinguished advantages:

1) Enhanced hole confinement: Hole confinement is the most critical factor for the performance of the GaSb-based laser diodes working at 3-4  $\mu\text{m}$  wavelengths. However, the hole confinement is only about 50 meV at 3.73  $\mu\text{m}$  using the conventional InGaAsSb/AlGaInAsSb active region and expected to be even lower at the increased wavelength. By using the GaInAsSbBi/AlGaAsSb or GaInAsSbBi/GaSb active regions, the hole confinement is substantially improved by more than 100 meV even at the optical transition wavelength of 4  $\mu\text{m}$ .

2) Extended wavelength: The current world record lasing wavelength of the RT CW operational GaSb-based laser diodes is 3.73  $\mu\text{m}$  achieved by using  $\text{Ga}_{0.28}\text{In}_{0.72}\text{As}_{0.44}\text{Sb}_{0.56}$  /  $\text{Al}_{0.3}\text{Ga}_{0.2}\text{In}_{0.5}\text{As}_{0.46}\text{Sb}_{0.54}$  active region. With the proposed GaInAsSbBi/AlGaAsSb or

GaInAsSbBi/GaSb active regions, the optical transition wavelength can be extended up to 4  $\mu\text{m}$  easily with enhanced hole confinement and balanced electron-hole confinement at the same time.

3) Eased growth complexity: The current InGaAsSb/AlGaInAsSb designs involve the growth of high In composition alloys in the miscibility gap, with the In composition over 70% in the QW regions and over 50% in the barrier layers, which considerably increases the growth complexity. By contrast, the GaInAsSbBi/GaSb designs not only significantly decreases the In composition used in the QW regions to below 40%, but also avoids growing high In composition barriers. In addition, thick AlGaInAsSb barrier layers have to be grown lattice-matched to GaSb substrates in conventional InGaAsSb/AlGaInAsSb designs, while no such requirements are in the proposed GaInAsSbBi/GaSb designs.

4) Elevated device reliability: The reliability of the GaInAsSbBi QW devices is improved in two ways. Firstly, the high In composition alloys which are thermally unstable are replaced by GaInAsSbBi alloys with much lower In composition. Secondly, the GaInAsSbBi alloys enable the realization of the quasi-Al-free laser diode designs, which fundamentally improves the reliability of the laser devices.

Additionally, the benefits brought by the novel GaInAsSbBi material are most likely underestimated. In the interpolation of the bandgaps, the bowing coefficients of bismide alloys such as GaAsBi, InAsBi, GaSbBi, InSbBi and etc, have been taken as zeros since there is no such set of data available for the time being. However, from the preliminary experimental bandgap measurements on GaAsBi alloys [26,77], there is a giant bowing in the bandgaps of GaAsBi. As shown in Fig 2.15, the experimentally fit bandgaps of GaAsBi alloys decrease



much faster than the linear estimation. In this fitting, the bowing coefficient is Bi composition related and the bandgaps are fit as [26]:

$$E_g(\text{GaAsBi}_x) = 1.423(1 - x) - 0.36x - x(1 - x) \frac{9.5}{1 + 10.4x} \quad (2.3)$$

At Bi composition of 10%, the bandgap of GaAsBi<sub>0.1</sub> is underestimated by 0.31 eV (1.14 eV vs. 0.83 eV) by using linear interpolation, which is almost equal to the optical transition energy of the 4 μm laser diodes.

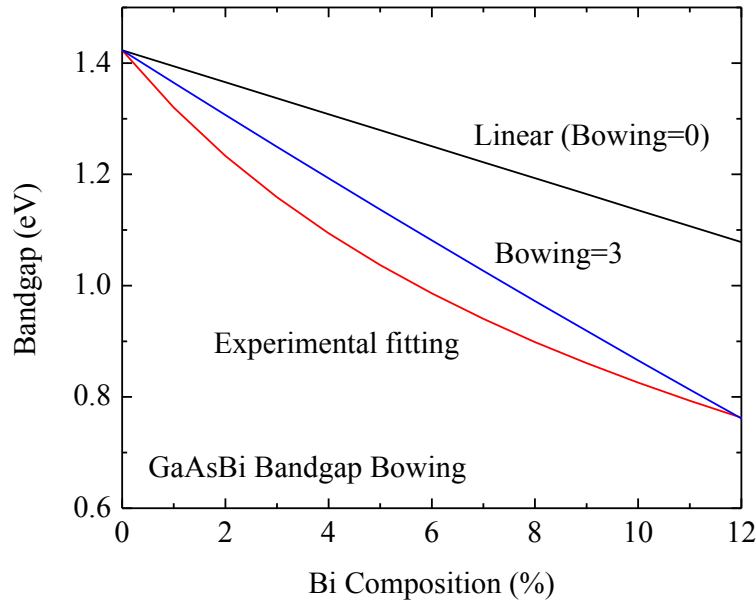


Fig. 2.15 The effect of bowing coefficient on the bandgaps of GaAsBi alloys, showing the bandgap reduction is much underestimated by using linear interpolation.

Here we use a constant bowing coefficient 3 to replace the previously used linear interpolation to evaluate the effect of the bowing coefficient of the GaAsBi alloys on the

bandgap interpolation of GaInAsSbBi alloys. The bandgaps are still underestimated but much closer to the actual values, as shown in Fig 2.15.

$$E_g(\text{GaAsBi}_x) = 1.423(1 - x) - 1.45x - 3x(1 - x) \quad (2.4)$$

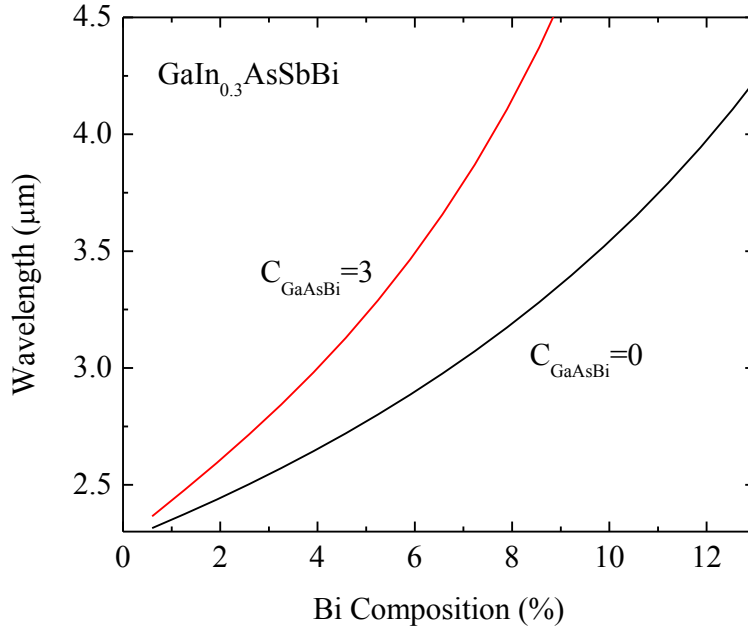


Fig. 2.16 The effect of the GaAsBi bowing coefficient on the optical transition wavelengths of the GaIn<sub>0.3</sub>AsSbBi QWs (with 1.5% compressive strain).

With this constant bowing coefficient of GaAsBi alloys used, significant bandgap reduction and wavelength extension can be achieved in the bandgap interpolation of GaInAsSbBi alloys. Fig. 2.16 shows the effect of the GaAsBi bowing coefficient on the optical transition wavelengths of the GaIn<sub>0.3</sub>AsSbBi QWs (with 1.5% compressive strain). When the bowing coefficient of GaAsBi is taken as 0, 12% Bi composition is required to achieve the 4 μm optical transition wavelength. However when the bowing coefficient is taken as 3, only 8% Bi composition is needed to achieve the same 4 μm wavelength, which means a ~33% decrease of the Bi composition.

Due to the similarity among the bismide alloys, it is expected that the bowing effect will occur in other bismide alloys as well. With accurate bowing coefficients applied in the interpolation model, the advantages of GaInAsSbBi alloys could be even greater. As the development of III-V bismide materials, the interpolation model is expected to be refined in accordance with the experimentally measured data.

## 2.2 GaInAsSbBi alloys for TPV devices

### 2.2.1. Introduction

TPV devices directly generate electricity from heat differentials via photons, which can be either from the combustion of fuels or from the waste heat of other energy sources. TPV energy conversion is of great interest as the power generators for space, military, underwater, and automobile applications because of its fuel diversity, high power output, silent operation, independence of sun light, and low maintenance cost [107-111]. A typical TPV system consists of four main components: a heat source in the 1000 – 1800 K range, a selective emitter and filter for spectral control, a photovoltaic diode cell, and a cell cooling system, as shown in Fig. 2.17.

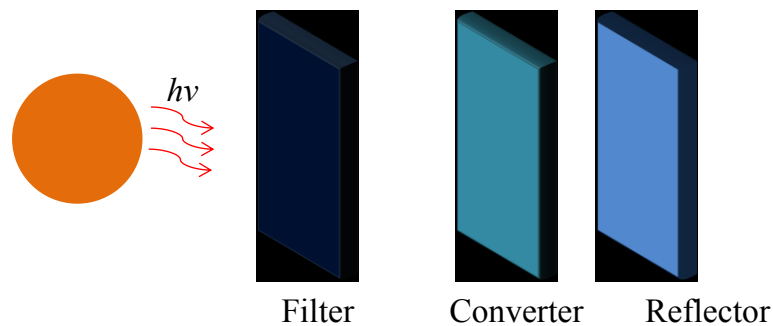


Fig 2.17 Schematic diagram of a typical TPV, including a heat source, a selective emitter and filter for spectral control, a photovoltaic diode cell (converter), and a reflector.

The major differences between a TPV device and a conventional solar cell lie in two aspects. Firstly, the distance between the photovoltaic diode cell and heat source in a TPV device (1-10 cm [112]) is much closer than that in a solar cell ( $1.496 \times 10^8$  km [113]), which results in a much higher incident power density in a TPV system. For example, the 1400 K blackbody radiation spectrum has a power density of  $21.8 \text{ W cm}^{-2}$ , while the air mass 0 (AM 0) only has a power density of  $0.1 \text{ W cm}^{-2}$ . Secondly, the heat source temperature (1000 – 1800 K) for a TPV device is much lower than that for a solar cell (5800 K). This means the peak energies in TPV source spectra are much lower than the energy peak in solar spectrum (see Fig 2.18), which requires the photovoltaic diode cells in TPVs to have much smaller bandgaps. Theoretical calculated results suggest that for blackbody radiation of 1000-1800 K the optimal bandgaps of the TPV cells are in the range of 0.25 – 0.5 eV, which is more close to the GaSb-based low bandgap compound semiconductors.

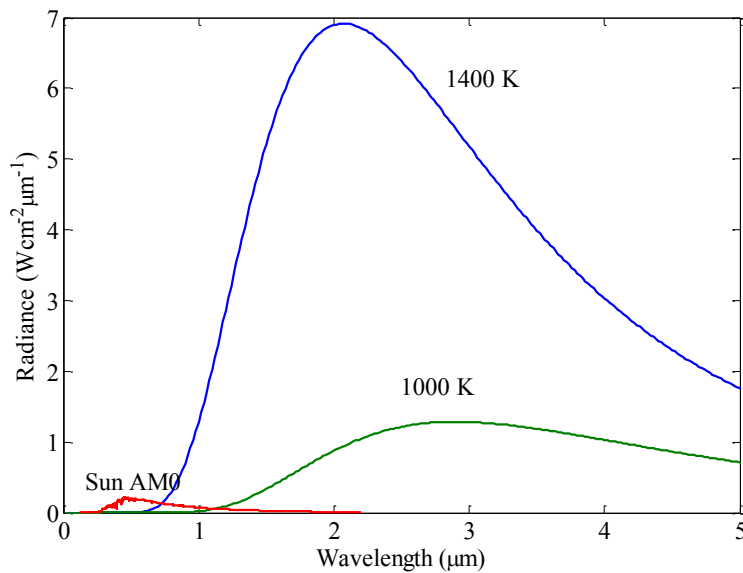


Fig. 2.18 Comparison of the solar extraterrestrial AM0 spectrum with the 1000K and 1400 K blackbody radiation spectra, showing the blackbody radiation spectra possessing much higher incident powers and much longer wavelength peaks.

### 2.2.2 Thermodynamic limit of single junction TPV

In this section, thermodynamic model is used to calculate the efficiency of single junction TPV devices. The thermodynamic model only considers radiative recombination so that the calculated efficiency sets an ideal upper limit for the practical cases [112,114]. Though the ideal efficiency is degraded in practice due to many factors such as non-radiative recombination, it is full of significance to provide guidelines on material selection and performance estimation for TPV designs. In our evaluation, the characteristics of TPVs are evaluated at typical source temperatures of 1000 K, 1400 K, and 1800 K. The incident power on the cells is assumed to be emitted from a planar blackbody source [112] and the cell temperature is set to room temperature 300 K. No spectral control is used in this model.

The efficiency and the power output of the TPV cells under a range of blackbody sources are shown in Fig. 2.19 and Fig. 2.20 respectively. The increase of source temperature results in the energy spectrum shifting to the high energy end and makes more power fall into the convertible range ( $h\nu > E_g$ ). The decrease of cell bandgap, on the other hand, is capable of absorbing more portion of the spectrum during the conversion. In both case, the efficiency and power output substantially increase.

Fig. 2.19 also shows that with the source temperatures varying in the range of 1000 - 1800 K the bandgaps for optimal efficiency and power output are required to be 0.25-0.4 eV, which are considerably lower than those in most conventional TPVs (0.53-0.72 eV). This is a real inspiration that, if the bandgap of the TPV cell is reduced, the efficiency of the TPV can be significantly improved. For example, reducing the bandgap from 0.5 eV to 0.35 eV can increase the efficiency by 5% for a 1400 K source and by 10% for a 1000 K source.

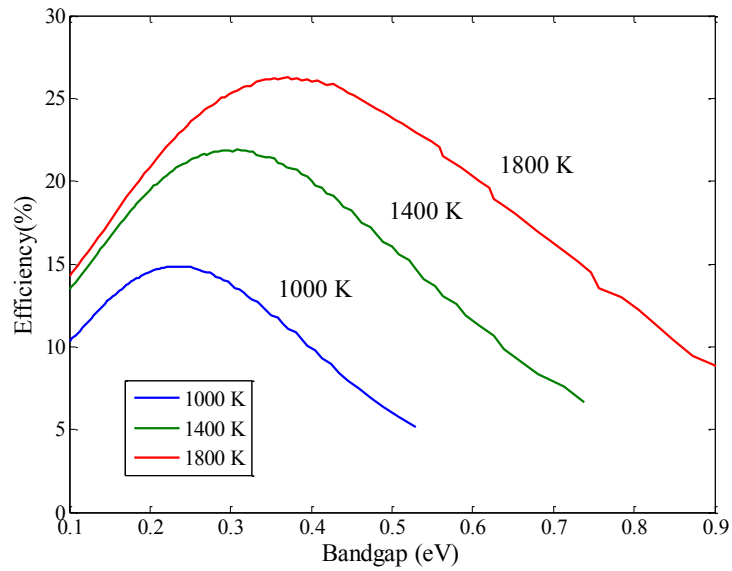


Fig. 2.19 Efficiency as a function of the bandgap with source temperatures varying from 1000K to 1800 K.

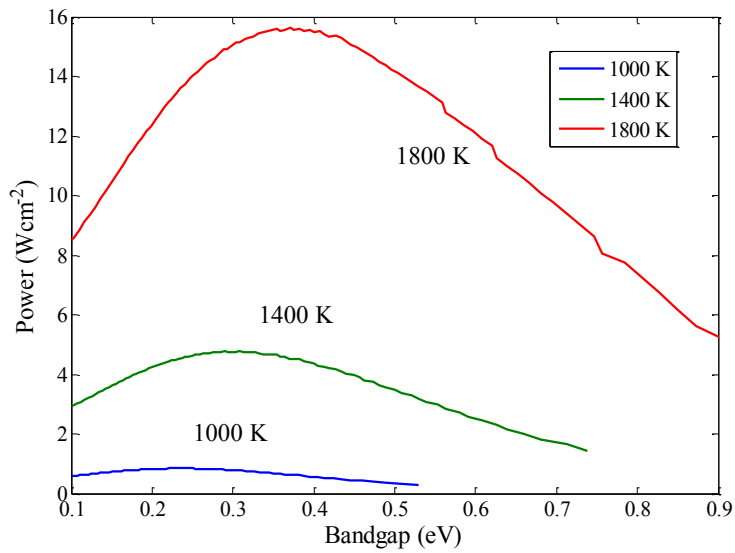


Fig. 2.20 Power output as a function of the bandgap with source temperatures varying from 1000K to 1800 K.

### 2.2.3 Multi-junction TPV

In the single junction TPV system the energy conversion efficiency is relatively low, which is limited by the inability of a single bandgap to match the broad radiation spectrum. From one side, the photons that are below the cell bandgap ( $h\nu < E_g$ ) cannot be absorbed in the conversion. Therefore, the smaller the bandgap, the more the photons can be absorbed. However, from the other side, although the photons with the energy above the cell bandgap ( $h\nu > E_g$ ) can be absorbed, the carriers generated by photon absorption immediately lose almost all energy in excess of  $E_g$  when the carriers relax to energies near the band edges. As a result, in single junction TPV diodes, a trade-off has to be made between the two effects, as shown in Fig. 2.19. In the large bandgap end the narrow spectrum coverage is the largest contributor to the efficiency loss while in the small bandgap end the carrier relaxation dominates the decrease of efficiency. An ideal case is expected where a boarder spectrum can be absorbed and the high energy carrier relaxation can be minimized.

The dilemma can be solved by using multi-junction TPV design, in which several photovoltaic junctions are connected in tandem to improve the efficiency [114]. This concept can be illustrated by the graphical analysis of the efficiency of the TPV cells using single-junction, double-junction and triple-junction TPV cells, as shown in Fig. 2.21. For example, in the triple-junction TPV cell, incident radiation first encounters the diode with the largest bandgap. The photons with the energies higher than the bandgap of the first diode is absorbed and the rest photons pass through the first diode and enter the second one. Similar absorption and transmission process occur in the second and third diodes in the multi-junction TPV cell. Most importantly, the generated carriers in each diode relax to their own band edges and mitigate the

decrease of efficiency as a result of carrier relaxation through the single band edge. The efficiency of the TPV cell is consequently considerably improved.

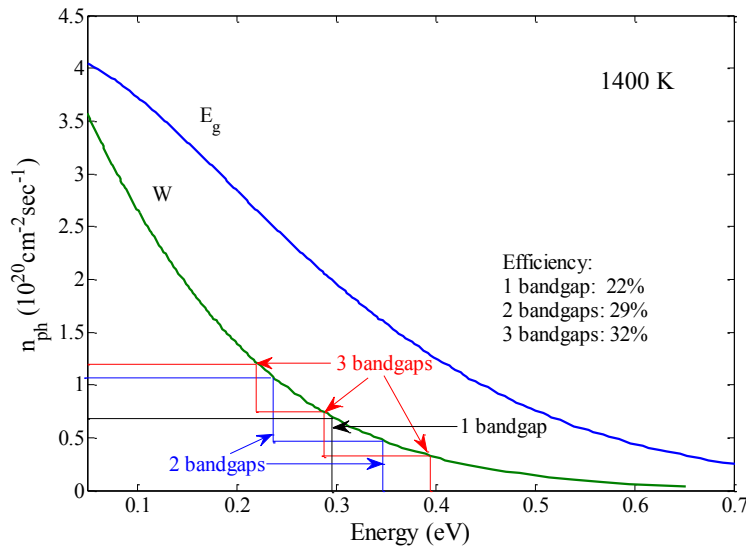
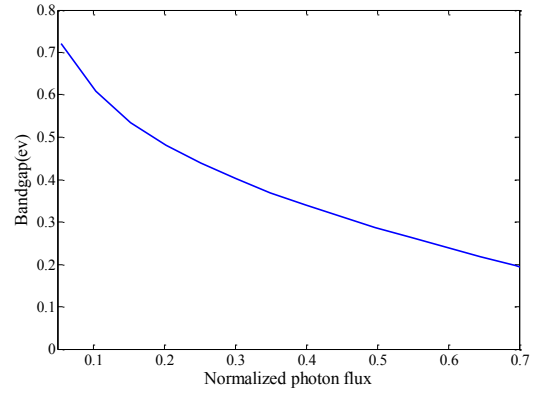
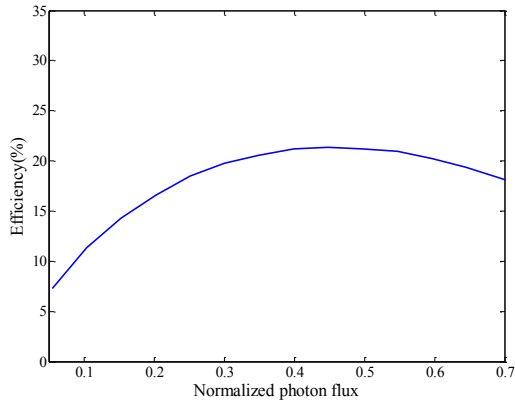


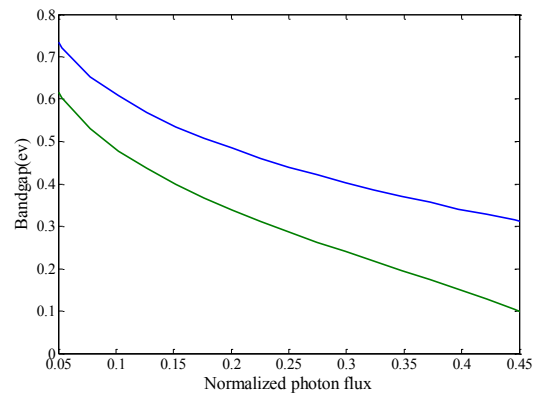
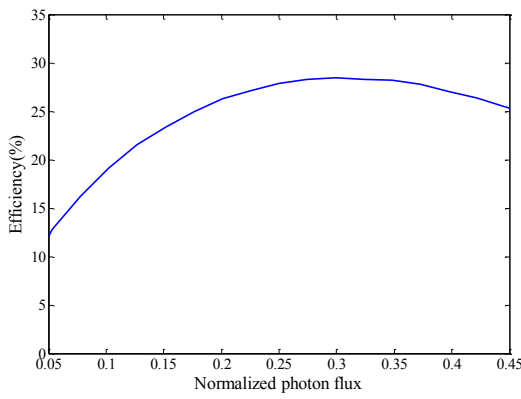
Fig. 2.21 Graphical analysis of the efficiencies of single-junction, double-junction and triple-junction TPV cells.

In the multi-junction TPV cell, the currents flowing through a string of photovoltaic junctions connected in series are identical. Hence, the photons absorbed in each component photovoltaic junction ( $\Delta_{nph}$ ) should be the same. The efficiencies of the multi-junction TPV cells can be calculated by using graphical calculation method [114]. Fig. 2.22 shows the optimum bandgaps for single-junction, double-junction and triple-junction TPV cells working under 1400 K blackbody radiation and their corresponding efficiencies. The optimal efficiency of the TPV cells can be improved from 21.5% (single-junction, 0.31 eV) to 28.5% (double-junction, 0.42 eV and 0.26 eV) and 31.9% (triple-junction, 0.46 eV, 0.31 eV and 0.20 eV) respectively.

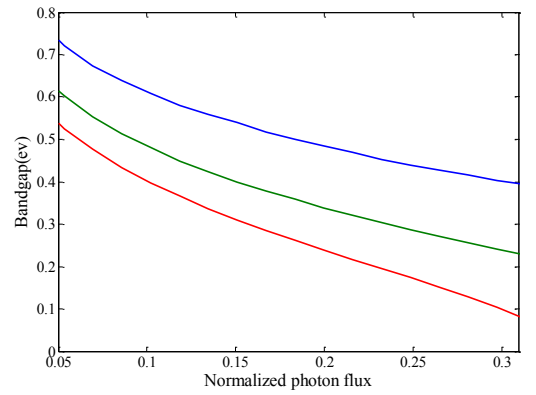
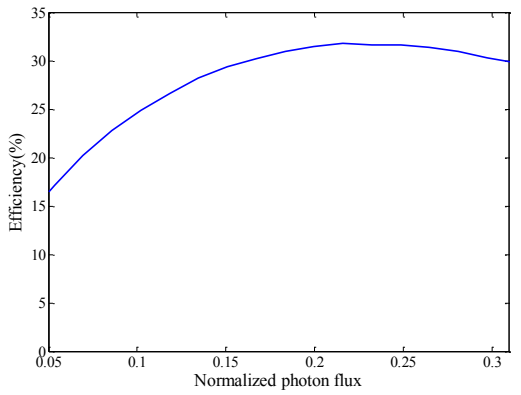




(a) single-junction



(b) double-junction



(c) triple-junction

Fig. 2.22 Efficiencies of multi-junction TPVs under 1400 K blackbody radiation. (a) single-junction; (b) double-junction; (c) triple-junction. The efficiency of the TPV cell is improved from 21.5% (single-junction) to 28.5% (double-junction) and 31.9% (triple-junction) respectively.

#### 2.2.4 GaInAsSbBi TPV cells

Since its invention in 1956 [115], TPV energy conversion systems have made significant progress over the years, which is attributed to the rapid advances in the emitters, bandpass filters, III-V epitaxial growth techniques for ternary and quaternary compound semiconductors, and monolithic interconnected modules (MIMs) [107-110].

Three leading material systems have been used to fabricate high efficiency TPV devices. The first one is to use Zn-diffused GaSb wafers [116,117], which is the most cost effective one since no expensive epitaxy process is used. The first commercial propane-fired TPV system was developed by JX Crystal Inc. using GaSb TPV cells ( $E_g = 0.72$  eV) and the overall efficiency of the TPV system is about 10% [118]. In order to lower the bandgap of the photoactive area to improve the efficiency, epitaxial InGaAsSb alloys that are lattice matched with GaSb were developed using LPE, MOCVD, and MBE [119-121]. Even MOCVD and MBE growth are at non-equilibrium conditions and can produce metastable alloys, permitting the growth of InGaAsSb with composition in miscibility regions, experimental results show that the metastable alloys tend to degrade when operating under high current density [122]. Thus, when taking the miscibility region into account, the lowest bandgap of the InGaAsSb alloy is about 0.50 eV (2.5  $\mu\text{m}$ ) [120]. The best reported TPV efficiency of InGaAsSb/GaSb diodes is 19.7% ( $E_g = 0.53$  eV) under 950 °C illumination [121]. The third approach is using lattice matched or lattice mismatched InGaAs grown on InP substrates [123-125]. The unique advantage of InP based TPV cells over the GaSb-based ones is that semi-insulating InP substrates are available so that monolithic interconnected modules (MIMs) are possible for InP based TPVs [124,125]. The best reported efficiency using this technology is 23%, which was achieved by a double-junction TPV device ( $E_{g1} = 0.72$  eV,  $E_{g2}=0.6$  eV) under 1000 °C illumination [126]. Recently, GaInAsSbP on

InAs substate has been reported to be used in TPV cells to obtain a lower bandgap of  $\sim 0.35$  eV [127].

According to the efficiency analysis of the multi-junction TPV cells, it is desirable to make use of narrow bandgap materials (0.25 – 0.5 eV) to achieve high efficiency TPV devices. In the previous section GaSb-based GaInAsSbBi material has been proposed to achieve MWIR laser diodes in 3-4  $\mu\text{m}$ . Correspondingly this alloy can be used to achieve high efficiency TPV cells as well. Fig 2.23 shows the bandgap contour of GaSb-based lattice-matched GaInAsSbBi at different In and Bi compositions, which shows the material broadly covers the desired bandgaps from 0.2 eV to 0.5 eV. Compared with InGaAsSb material (where Bi=0%, y-axis), GaInAsSbBi material is capable of achieving the same bandgap but with much lower In composition. Thus, it prevents the material to be grown in the deep miscibility gap and therefore fundamentally improve the reliability of the devices.

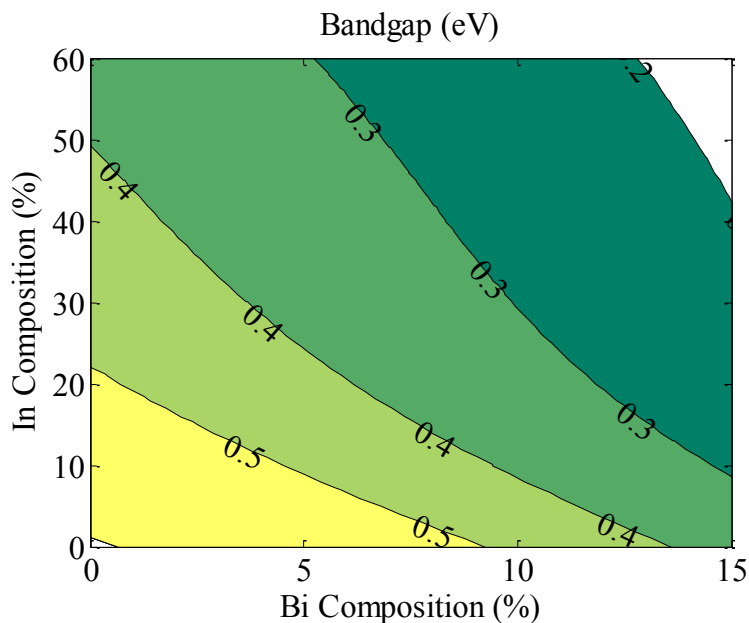


Fig. 2.23 Bandgap contours of GaInAsSbBi material (lattice-matched with GaSb) at different In and Bi compositions.

In addition, due to the extraordinarily large  $\Delta_{SO}$  of GaBi and InBi [76], the  $\Delta_{SO}$  of GaInAsSbBi is expected to be considerably enhanced to suppress the CHSH Auger recombination in the TPV devices, which becomes increasingly important with the decrease of TPV bandgaps [112,121].

Fig.2.24 shows a schematic diagram of triple-junction TPV cell, containing three GaInAsSbBi alloys with different bandgaps of 0.50 eV, 0.35 eV and 0.25 eV. Based on theoretical calculation, this structure is expected to achieve the highest efficiency 31% so far.

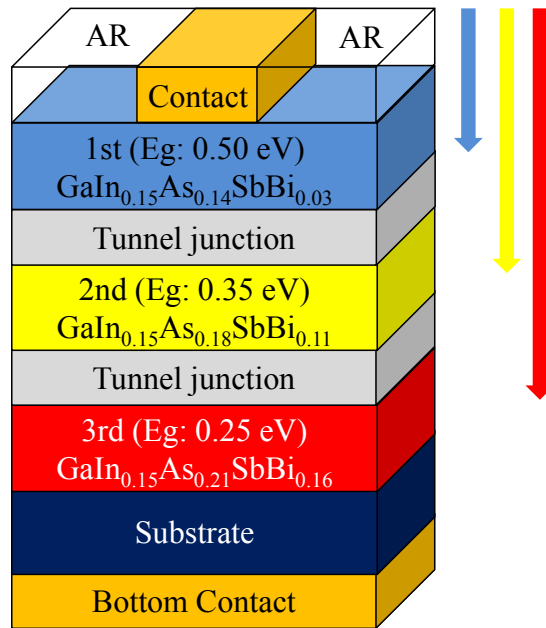


Fig. 2.24 Schematic diagram of a three junction TPV cell which contains three diodes with different bandgaps connected in tandem.

The narrow bandgap GaInAsSbBi material enables the development of multiple-junction TPV devices to achieve optimal energy conversion efficiency. The enhanced  $\Delta_{SO}$  of GaInAsSbBi material is promising for enhanced performance of the devices due to suppression of non-radiative process.

## 2.3 Summary

In this chapter, the current technologies used in RT CW operational GaSb-based type-I QW MWIR laser diodes in the 3-4  $\mu\text{m}$  wavelength range have been thoroughly analyzed to identify their limitations such as insufficient hole confinement ( $\sim 50$  meV), restricted emission wavelength (with a record of 3.73  $\mu\text{m}$ ) and intrinsic reliability issues due to high In ( $>70\%$ ) and Al ( $\sim 30\%$ ) composition in the active regions. To address these issues, we have proposed using novel GaInAsSbBi alloys to replace the InGaAsSb alloys in the QW regions to achieve a longer optical transition wavelength up to 4  $\mu\text{m}$ . In the extensive exploration of the novel alloys, we have demonstrated their capability and flexibility in tuning the optical transition wavelength and band alignment in a wide range. Less than 12% Bi composition and less than 40% In composition in the GaInAsSbBi alloys are required to achieve the laser diodes with 4  $\mu\text{m}$  optical transition wavelength and  $\sim 150$  meV hole confinement. Moreover, quasi-Al-free laser structures can be realized by using GaInAsSbBi/GaSb active regions and InGaAsSb cladding layers consequently significantly improve the reliability of the laser devices. Compared with the currently used technologies, our proposed technology achieves enhanced hole confinement, extended wavelength, eased growth complexity and elevated device reliability. In addition, we have proposed the GaInAsSbBi alloys to be used in high efficiency multi-junction thermophotovoltaic devices. Compared with traditionally used InGaAsSb alloys, GaInAsSbBi alloys provide much narrower bandgaps (below 0.5 eV), which result in broader spectrum coverage and considerably improved efficiency. The advantages of the novel GaInAsSbBi alloys greatly promote the development of the III-V bismide material towards high performance optoelectronic devices.



### 3 MOLECULAR BEAM EPITAXY AND SURFACTANT MEDIATED GROWTH

MBE, invented and developed by A. Y. Cho in Bell labs in late 1960s and early 1970s [128-130], is an epitaxial growth technique which deposits thermal molecular beams onto heated crystalline substrate under ultra-high vacuum (UHV) conditions. This growth technology has promoted the development of various electronic and photonic devices such as QW laser diodes [131,132] and high mobility electron transistors (HEMTs) [133], which are widely applied in cellular phones, CD players, high-speed communications, etc.

#### 3.1 Brief introduction of molecular beam epitaxy

Since its invention MBE has been utilized to grow a variety of materials including III-V, II-VI, Si/Ge, oxide materials because of its superior characteristics [134-136]. It is largely differentiated itself from other material evaporation techniques by the *in-situ* surface characterization using reflected high energy electron diffraction (RHEED). In RHEED system, the high energy electron beam is directed to the sample at the grazing angle and collected at the other end using a phosphor screen, as shown in Fig. 3.1.

Due to the grazing angle incidence ( $\sim 1^\circ$ ) of the electron beam, the penetration depth of the electron beam is limited to the first several atomic layers of the growing surface. Hence, the RHEED system only collects information from the growing surface of the sample, making it a perfect *in-situ* characterization tool to monitor and control the MBE growth. In this dissertation, the most frequently used information obtained from RHEED system is the growth rate and the surface reconstruction.

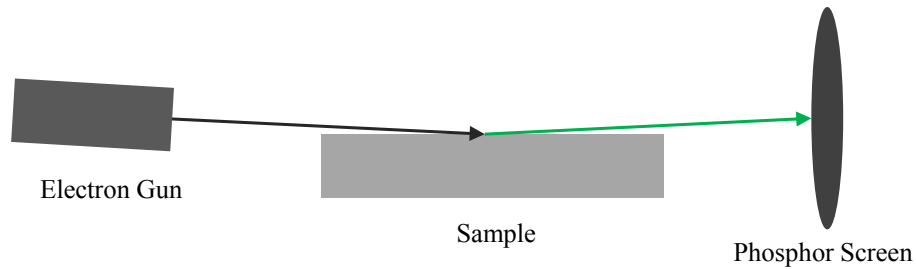


Fig. 3.1 Schematic diagram of a RHEED system.

The growth rate of the MBE growth can be easily calculated from the RHEED oscillation. It has been found that the RHEED oscillation results from the surface roughness oscillation of the growth front and the oscillation period of RHEED intensity is equal to the time of depositing one monolayer of material [137]. In this work, GaAs material is typically grown at one monolayer/s (ML/s), which is about 1  $\mu\text{m}$  per hour.

Surface reconstruction, on the other hand, plays a critical role of monitoring the surface structures, surface topography, and to a certain extent, the surface composition [138]. For example, in GaAs growth, a  $(2\times 4)$  reconstruction represents an As rich growth condition while a  $(4\times 2)$  reconstruction represents a Ga-rich condition. Moreover, the substrate temperature can be effectively calibrated by the transition of the RHEED reconstruction patterns. For instance, the accurate substrate temperature is difficult to obtain in the MBE growth of GaSb since the bandgap of GaSb at high temperature is beyond the cut-off wavelength of the InGaAs detector used in the BandiT optical band gap thermometry which relies on the detection of the optical absorption edge of the substrate to fit the temperature. In this case, the substrate temperature is usually calibrated using the surface reconstruction transition from  $(1\times 3)$  to  $(1\times 5)$  [139,140].

In general, compared with other growth techniques, the MBE growth technique has many outstanding advantages:



First of all, MBE growth technique can provide precise control on film thickness to sub-monolayer level. This is because the thin film is usually grown at the growth rate about  $\sim 1$  ML/s and when the shutter of the beam is shut off, the beam flux can be turned off almost instantly. The sub-monolayer precision enables the growth of complicated quantum nanostructures with abrupt interfaces such as QWs and quantum dots (QDs).

Secondly, the purity of the material grown by MBE is superior since its UHV environment ( $\sim 10^{-10}$  Torr) minimizes the contamination of the growing surface. In the UHV environment, the beam atoms molecules have mean free paths on the order of meters which are much bigger than the distance between the cells and the substrate ( $\sim 30$ - $50$  cm). Consequently, the beam atoms and molecules travel in virtually collision-free paths until they arrive the substrate or the liquid-nitrogen-cooled cryopanel where the residual atoms and molecules condense and are removed from the UHV environment. The excellent material quality with extremely low density impurity offers the high performance devices with low defect density.

Thirdly, as a non-equilibrium growth technique, MBE growth is capable of growing thermodynamically metastable alloys within the miscibility gap. For example, the GaSb-based  $\text{In}_x\text{Ga}_{1-x}\text{As}_y\text{Sb}_{1-y}$  material system, which has the miscibility gap of In composition from 0.18 to 0.84 [60], has been successfully grown using MBE with the In composition up to 0.72 [43].

### **3.2 Bi surfactant mediated growth**

Surfactants are a kind of elements that tend to segregate and float on the growth surface and exercise an influence on the surface properties [141,142] by interacting with the adatom species present on the surface. At the same time, the surfactants usually have negligible solubility to the host material. Bi is the heaviest group V element and highly tends to segregate on the growing

surface, which makes it a perfect surfactant for the MBE growth. Although Bi alloys with III-V materials at low growth temperatures ( $< 400$  °C) during MBE growth, it is hard to alloy with others at high temperatures [143]. Therefore, Bi has been chosen as a surfactant to promote layer-by-layer growth, reduce interface roughness, and improve the PL efficiency in GaAs, InGaAs, AlGaAs, InGaNAs, and GaInP growth, either using MBE or MOCVD [144-153].

In order to demonstrate the effect of Bi as the surfactant on surface migration of the adatoms and the optical quality of the material, we investigate the Bi surfactant mediated growth of InAs QDs using MBE [154]. In the experiment, two types of InAs QD samples, Bi-free and Bi-mediated, were grown on Si-doped n-type (001) GaAs substrates using a Riber-32P MBE system equipped with effusion cells for Ga, In, and Bi, and a two-zone valved cracker cell for As. Sample A refers to the Bi-free growth, where the Bi shutter was closed during growth. Sample B refers to the Bi-mediated growth, where the Bi and In shutters were opened and closed simultaneously during the growth. The beam equivalent pressure of Bi flux was set to  $8 \times 10^{-8}$  Torr. For both samples, the formation of InAs QDs was confirmed by the transition of the RHEED pattern from streaky 2D growth to spotty 3D growth. A growth interruption of 30 seconds was introduced after the InAs deposition followed by a 10 nm-thick GaAs layer grown at 480 °C and an additional 90 nm-thick GaAs layer grown at 580 °C. The substrate temperature was then ramped down to 480 °C to duplicate the InAs QD structures for the purpose of surface morphology measurements, after which the samples were rapidly cooled to preserve the surface morphology to the maximum extent. Table 3.1 summarizes the layer structures and growth temperature profiles of both samples.

Table 3.1: Summary of the layer stacks of the InAs QD samples, including the thickness and growth temperature of each layer. Sample A (the control sample) is grown without Bi (Bi-free). Sample B is grown with Bi (Bi-mediated). [D. Fan, *et al.*, “Bismuth surfactant mediated growth of InAs quantum dots by molecular beam epitaxy”, J. Mater. Sci: Mater. Eletron., DOI: 10.1007/s10854-012-0987-z, 2012]. With kind permission from Springer Science and Business Media.

Layer	Thickness	Temp.(°C)	Sample A	Sample B
InAs QDs	2.5 MLs	480	Bi off	Bi on
GaAs cap	90 nm	580	Bi off	Bi off
GaAs cap	10 nm	480	Bi off	Bi off
InAs QDs	2.5 MLs	480	Bi off	Bi on
GaAs buffer	400 nm	580	Bi off	Bi off
GaAs sub	350 $\mu\text{m}$	N/A		

Fig. 3.2(a) shows a  $1 \times 1 \mu\text{m}^2$  AFM image of traditional Bi-free InAs QD structures with a density of  $4.1 \times 10^{10} \text{ cm}^{-2}$ . The size distribution of QDs shown in Fig. 3.2(c) exhibits a bimodal characteristic with peak heights of 5.6 nm and 4.1 nm. The bimodal distribution is ascribed to the dissolve of a certain fraction of InAs QDs during the growth interruption to facilitate the growth of other QDs [155]. Fig. 3.2(b) shows a similar  $1 \times 1 \mu\text{m}^2$  AFM image of the Bi-mediated InAs QD growth with a density of  $2.0 \times 10^{10} \text{ cm}^{-2}$ , which is reduced by half compared with the Bi-free sample. The size distribution of the Bi-mediated QDs also exhibits a bimodal characteristic (see Fig. 3.2(c)) with peak heights of 7.3 nm and 5.8 nm. The increased QD height peaks reveal a significant increase of In surface diffusion during the growth [156]. The reduction

of the QD density combined with the increased QD sizes validates our expectation that Bi increases the surface diffusion of In adatoms during InAs QD growth. Bi-mediated growth hence provides an effective approach to control the density of InAs QDs besides the traditional ways by varying growth temperature and/or growth rate.

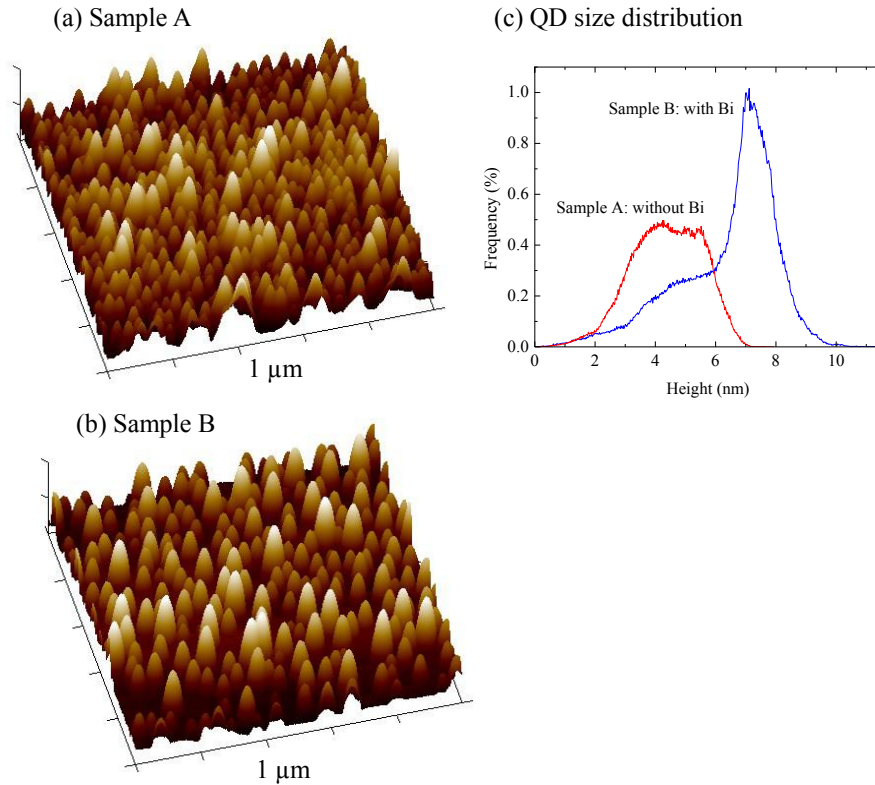


Fig 3.2 (a)  $1 \times 1 \mu\text{m}^2$  AFM image of the sample A (Bi-free) with the density of  $4.1 \times 10^{10} \text{ cm}^{-2}$ ; (b)  $1 \times 1 \mu\text{m}^2$  AFM image of the sample B (Bi-mediated) with the density of  $2.0 \times 10^{10} \text{ cm}^{-2}$ ; (c) Height histograms of samples A and B: the size distribution of sample B is shifted to the larger size direction. [D. Fan, *et al.*, “Bismuth surfactant mediated growth of InAs quantum dots by molecular beam epitaxy”, *J. Mater. Sci: Mater. Electron.*, DOI: 10.1007/s10854-012-0987-z, 2012].

With kind permission from Springer Science and Business Media.

In addition, the PL intensity of the Bi-mediated sample is also improved. As shown in the inset of Fig. 3.3, the PL peak intensity of sample B has been improved by  $\sim 2.1$  times over sample A at the excitation intensity of  $0.02 \text{ W/cm}^2$  at 16 K. Moreover, Fig. 3.3 shows the photoexcitation intensity dependence of wavelength-integrated PL intensity of InAs QD samples, which is measured at 16 K with the optical excitation intensity varying in the range of  $10^{-3} - 10^3 \text{ W/cm}^2$ . The linear dependence of the integrated PL on the photoexcitation intensity indicates low defect and dislocation densities of the samples [157].

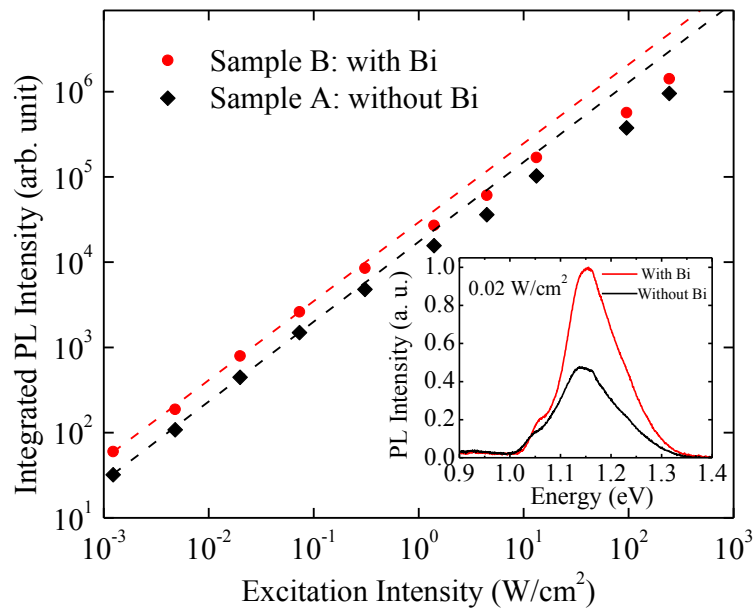


Fig. 3.3 Excitation intensity dependence of the wavelength-integrated PL intensity for Sample A grown without Bi (black diamonds) and Sample B grown with Bi (red circles). The measurement is performed at 16 K. The inset shows the spectra of the two samples at excitation intensity of  $0.02 \text{ W/cm}^2$ . [D. Fan, *et al.*, “Bismuth surfactant mediated growth of InAs quantum dots by molecular beam epitaxy”, *J. Mater. Sci: Mater. Electron.*, DOI: 10.1007/s10854-012-0987-z, 2012].

With kind permission from Springer Science and Business Media.

The experimental results have demonstrated that Bi-mediated growth can provide improved control over the MBE growth of InAs QDs, by not only decreasing the density of InAs QDs but also improving the PL intensity, which is very useful for the applications that require high optical quality and low QD density. Bi as a surfactant provides a simple and effective method to enhance diffusion length and improve the optical quality of III-V material during the MBE growth.

### **3.3 Summary**

In this chapter, we have discussed the MBE growth and the *in-situ* monitoring technique using RHEED system. With the real time monitoring capability, the MBE growth exhibits its superior performance on growing abrupt heterostructures, ultralow impurity materials and thermodynamically metastable alloys. Meanwhile, we have demonstrated the effectiveness of Bi as a surfactant using the Bi mediated growth of InAs QDs. The Bi surfactant greatly improves the optical properties of the InAs QDs and opens up new opportunities for the III-V bismide research.

## 4 MBE GROWTH OF GAASBI ALLOYS

III-V bismide material systems have increasingly drawn attention in the optoelectronics field because of the effectiveness of the Bi in reducing the bandgaps, lifting-up the VBMs and increasing the  $\Delta_{SO}$  in the III-V material systems. The previously discussed GaAs-based temperature insensitive SWIR laser diodes and GaSb-based MWIR laser diodes are two notable examples in this field. However, the growth of the III-V bismide materials remains challenging due to their low growth temperature and narrow growth windows. For example, GaAs material is conventionally grown at  $\sim 580$  °C and at non-stoichiometric As rich condition, while the GaAsBi material is best grown at  $\sim 280$ - $400$  °C and at the near stoichiometry of the As:Ga [26]. The stringent control over the stoichiometry leads straight to a narrow growth window and low repeatability of the growth. Therefore, it is of great significance to examine the exact mechanism of the III-V material growth to better control the growth process to achieve the desired material properties for device development.

In this chapter, we study the MBE growth of GaAsBi alloys and investigate the effects of the Bi flux and substrate temperature on the incorporated Bi composition and material properties. Structural and optical properties of the material are extensively characterized to get in-depth knowledge of the growth process. In particular, we explore the behavior of Bi during the growth of GaAsBi alloys and make some important discoveries about the great impact of the surfactant effect of Bi in the low temperature growth. Based on these important discoveries, a new growth scheme to grow high quality GaAsBi/GaAs/AlGaAs SCHs at low temperatures are successfully demonstrated [158], which is further discussed in detail in Chapter 5. Furthermore, the Bi mediated growth also opens the possibilities to grow high quality III-V materials on Si substrates at low temperatures, as will be elaborated in Chapter 7.

#### 4.1. GaAsBi/GaAs material growth

In this section, GaAsBi/GaAs bulk and QW samples were grown on semi-insulating GaAs (001) substrates using a Riber-32P MBE system equipped with effusion cells for Ga, Bi and a two-zone valved cracker cell for As. A *kSA* BandiT optical band gap thermometry was used to monitor the substrate temperature during the growth. The oxide desorption was performed at 610 °C for 10 minutes followed by a 400 nm GaAs buffer layer grown at 580 °C at the growth rate of 1 ML/s. For bulk samples, a 20 minutes growth interruption was then applied to decrease the growth rate to 0.1 ML/s and lower the substrate temperature to desired values (320°C - 370°C), followed a 300 nm GaAsBi layer without GaAs cap layer. For QW samples, no growth interruption is used in the growth to prevent contamination precipitation in the MBE chamber to improve the interface quality. The substrate temperature was decreased to 320 °C and Ga flux reduced to 0.35 ML/s respectively without growth interruption, after which the GaAsBi QW with desired width (5 nm – 20 nm) and a 23 nm GaAs cap layer were successively grown. Near stoichiometry of III/V and normal As rich condition were used for GaAsBi QW region and GaAs cap layer respectively. The structural diagram, temperature profile and cross-sectional scanning transmission electron microscopy (STEM) image for a typical GaAsBi/GaAs QW sample is displayed in Fig. 4.1. A (2 × 1) RHEED reconstruction pattern was observed in the growth of GaAsBi bulk and GaAsBi QW region while a (1 × 3) pattern was observed in the growth of GaAs cap layer, as shown in Fig. 4.2.



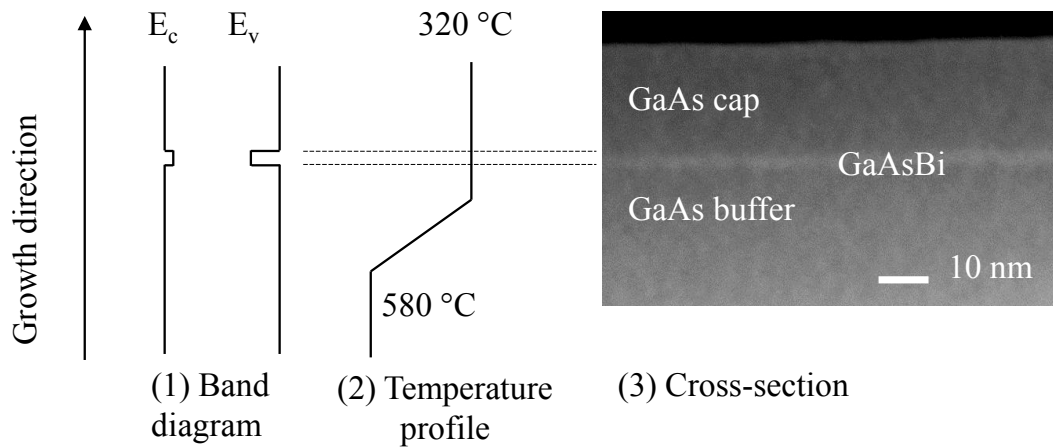


Fig. 4.1: Band diagram, growth temperature profile and cross-sectional STEM image of a typical GaAsBi/GaAs QW sample.

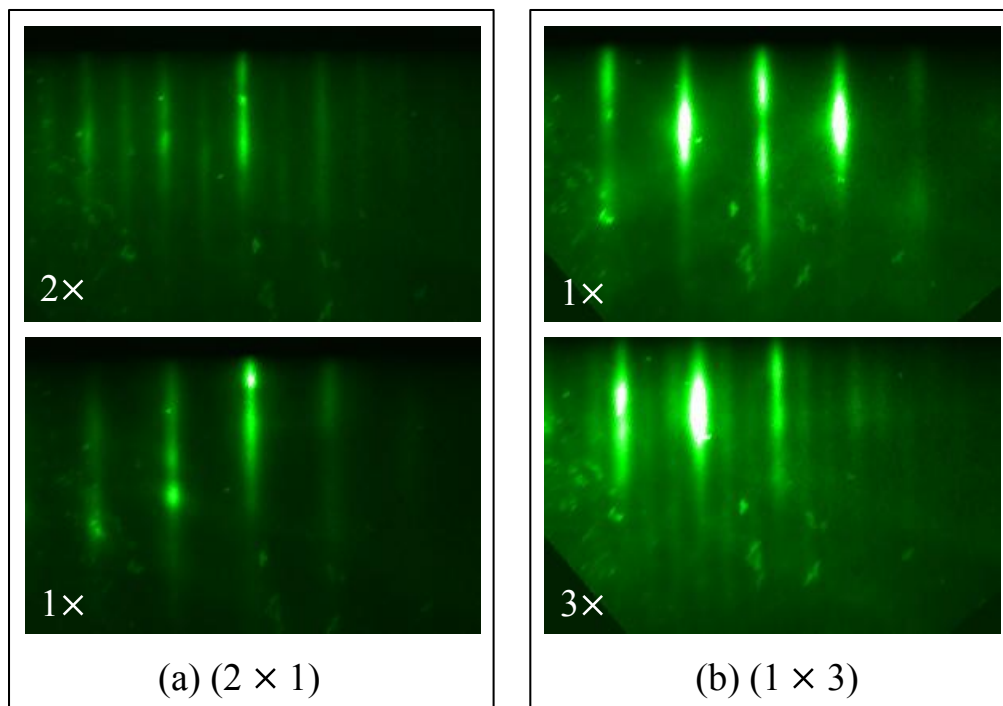


Fig. 4.2:  $(2 \times 1)$  RHEED reconstruction pattern in the growth of GaAsBi QW region (a) and  $(1 \times 3)$  pattern in the growth of GaAs cap layer (b).

## 4.2 Effects of Bi flux on morphological and optical properties of GaAsBi

Six GaAsBi/GaAs QW samples (sample A – sample F) are grown at 320 °C under the same growth condition except that the Bi flux is varied during the growths of GaAsBi QW regions from  $2.2 \times 10^{-9}$  to  $7.3 \times 10^{-8}$  Torr. The surface morphology of the samples is studied using AFM in tapping mode and the AFM images are displayed in Fig 4.3. The samples have smooth surfaces with low root mean square (RMS) surface roughness from 0.318 nm to 0.560 nm, which are attributed to the Bi's surfactant effect during the growth of GaAs cap layers. As the Bi flux increases, the samples gradually show elongated features in the  $[01\bar{1}]$  direction on the surface (see Fig 4.3 (e) and (f)). Meanwhile, Bi droplets will form on the surface with the increase of the Bi flux. Fig 4.4 (b) shows the density of Bi droplets as a function of the Bi flux. Samples A and B show zero droplet density and perfect mirror surface. When the Bi flux reaches  $9.0 \times 10^{-9}$  Torr ( $\frac{1}{2}$  on the x-axis), Bi droplets start to appear on the surface. The density of the droplets increases approximately linearly with the increase of the Bi flux. It is interpreted as the Bi atoms incident to the sample surface have not been fully incorporated into the GaAs lattice during the growth of GaAsBi QW regions and the surplus Bi atoms instead accumulate on the surface to form droplets.

The optical properties of the samples are investigated using PL measured at 18 K. The optical excitation is provided by a 532 nm Nd:YAG laser, and the PL signal is detected using a liquid nitrogen cooled InGaAs photodiode array. Low density excitation of  $1.4 \text{ W/cm}^2$  is used to ensure the spectra from the ground-state transitions. PL peak wavelengths of the samples and Bi compositions in the GaAsBi QW regions are displayed in Fig. 4.4 (c) and (d) respectively. In low Bi flux range ( $< 1$  in the x-axis), the peak wavelength increases rapidly with the increase of

Bi flux. However, in high Bi flux range ( $> 1$  in the x-axis), the increase of the peak wavelength shows a much slower upward tendency, which applies to the Bi composition similarly.

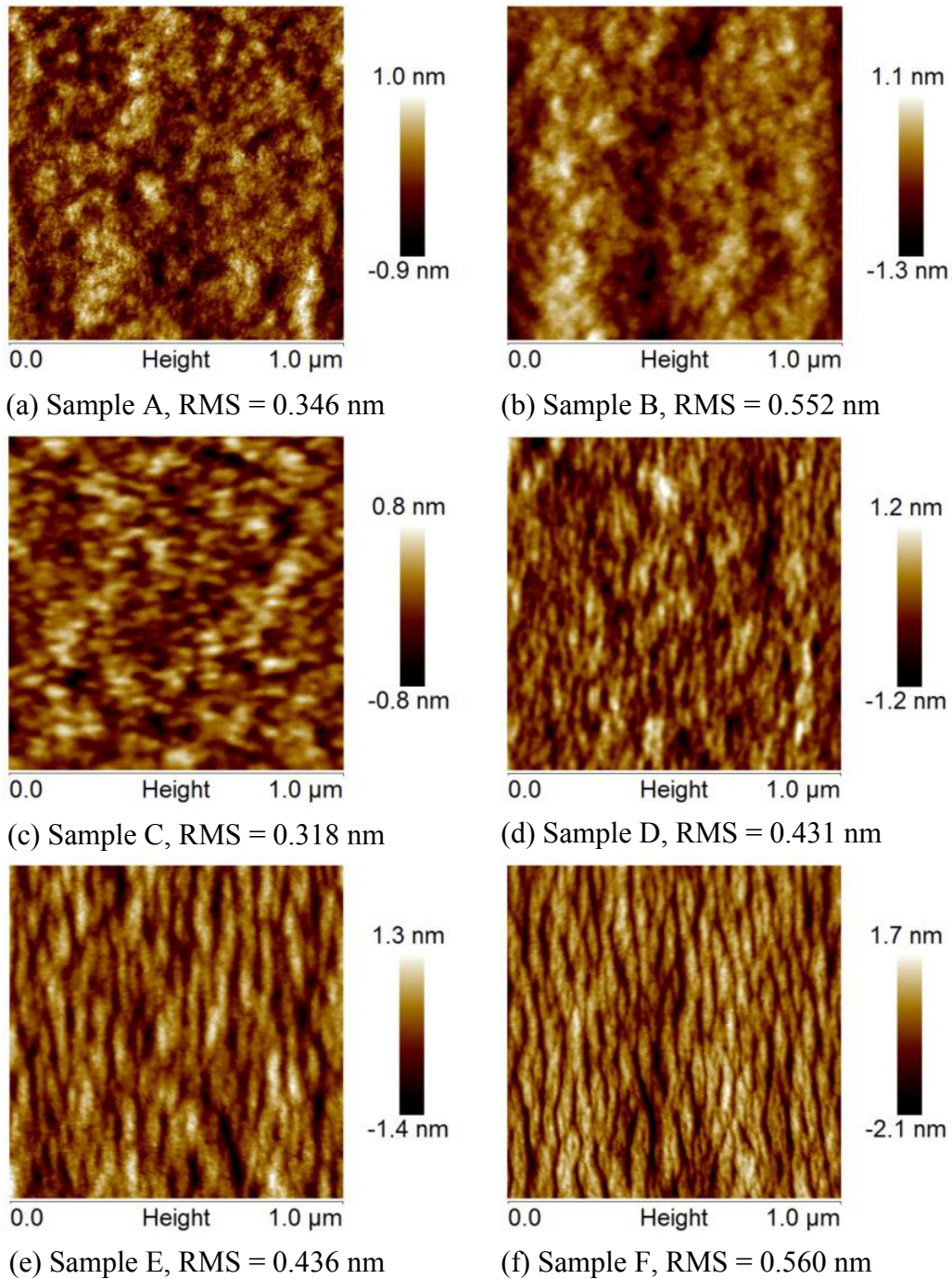


Fig 4.3 AFM images of the six GaAsBi/GaAs QW samples grown at the same condition but with increasing Bi fluxes from (a) to (f).

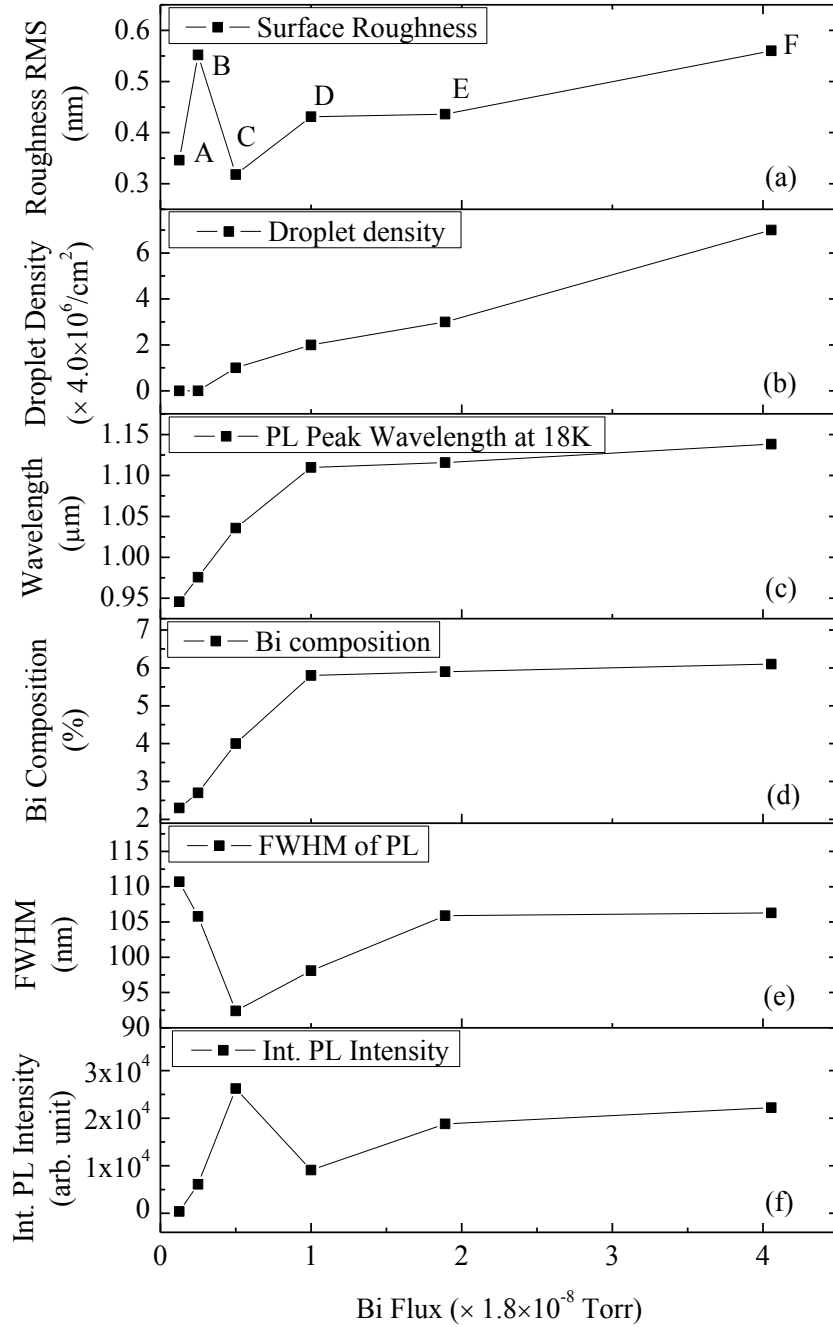


Fig. 4.4: The effect of Bi flux on the morphology and optical properties of GaAsBi/GaAs QW samples A-F: (a) surface roughness, (b) density of Bi droplets, (c) PL peak wavelength, (d) Bi content, (e) FWHM of the PL spectra, and (f) integrated PL intensity.

The slowed increasing tendency in PL peak wavelength and Bi composition is explained by the gradual saturation of the Bi atoms in the GaAsBi regions. There are two opposite processes evolved in the growth of GaAsBi QW regions: the first one is the Bi atoms at the growing surface being incorporated into the GaAs lattice; the second is the Bi atoms in the lattice segregating onto the surface. The desorption of Bi atoms from the growing surface is neglected here since the Bi desorption rate at the growth temperature is negligible [10]. The incorporation rate depends on the competition between the As and Bi atoms. Consequently, the bigger the Bi flux, the higher the incorporation rate. Accordingly, the segregation rate depends on the ability of the Bi atoms to escape from the lattice and segregate on the surface. The higher the growth temperature and Bi content in the lattice, the higher the segregation rate will be. As a result, at low Bi flux, the segregation process is negligible and the incorporation process plays the leading role, which results in the linear increase of the Bi composition with increasing Bi flux. At higher Bi flux, the segregation process is gradually aggravated by the increased Bi composition and becomes comparable with the incorporation process. At last, a balance is reached between the two processes, which results in the saturation of the Bi composition. It turns out that at a certain growth temperature, the Bi composition can only be effectively tuned by the Bi flux within the saturation limit. That is to say, other growth parameters have to be adjusted, such as lowering the substrate temperature, in order to achieve the Bi composition beyond the saturation limit at that temperature.

The full widths at half maximum (FWHMs) of the samples are shown in the Fig 4.4 (e). With the increase of the Bi flux, the FWHM decreases from 110.7 nm to 92.4 nm in low flux range and increase back to 106.3 in high Bi flux range. The integrated PL intensities of the samples are depicted in Fig 4.4 (f). In low Bi flux range, the intensity increased sharply as the

increase of the Bi flux. This is not only because of the increased confinement of the GaAsBi QW due to its reduced bandgap, but also because of the improved material quality due to the surfactant effect of Bi in the growth of GaAs cap layer. The intensity then decreases slightly with the further increasing Bi flux, which may be caused by the increased density of Bi droplets. As a result, as shown in Fig 4.5(a), at 18K sample C with intermediate Bi flux ( $9.0 \times 10^{-9}$  Torr) shows the smallest FWHM and highest integrated PL, yet the sample has Bi droplets on the surface with the density of  $4.0 \times 10^6/\text{cm}^2$ . However, at RT the PL peak intensity of sample C is outpaced by  $\sim 10$  times by sample D which has 2 times higher Bi flux than sample C, as shown in Fig 4.5(b).

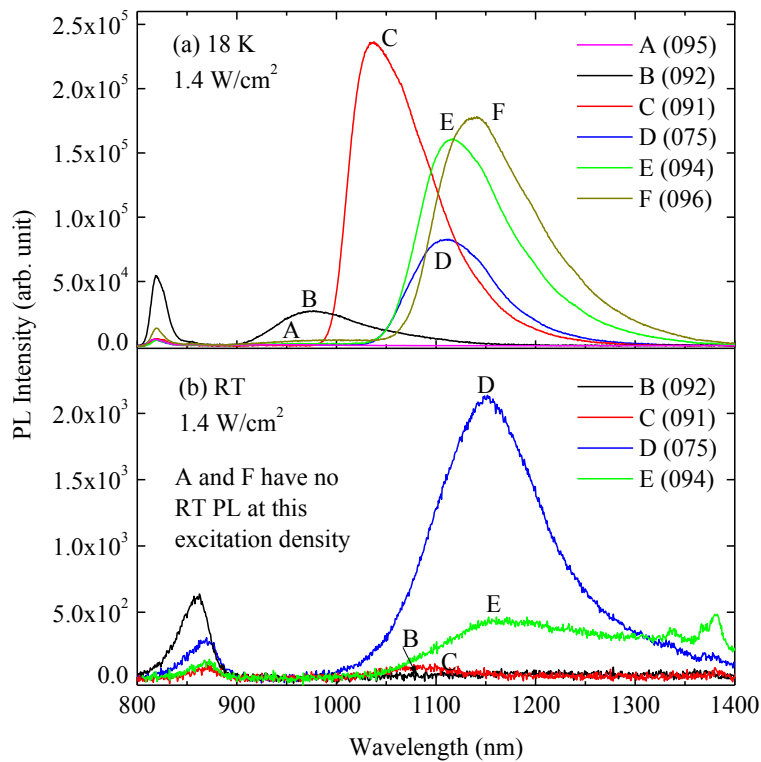


Fig. 4.5 PL spectra of the GaAsBi/GaAs QW samples measured at 18 K (a) and RT (b). The samples with intermediate Bi fluxes show best optical properties.

Compared with the spectra in Fig 4.5(a), this discrepancy of PL intensity reveals the effect of Bi to improve material quality by lower the non-radiative recombination centers that become activated at RT temperature. Moreover, at RT sample A with the lowest Bi flux and sample F with the highest Bi flux don't show PL peaks at this excitation density ( $1.4 \text{ W/cm}^2$ ), indicating poor material quality due to high density of non-radiative recombination centers in the samples. The PL spectra of the samples at low temperature and RT clearly exhibit the beneficial effect of Bi as a surfactant to improve material quality and the detrimental effect of Bi droplets to deteriorate the material quality. It is discovered for the first time that there is an optimal Bi flux range for the optical properties of the GaAsBi QW samples. Too low Bi flux would not be able to provide enough Bi surfactant atoms for the following growth of GaAs cap layer while too high Bi flux results in massive Bi droplets on the sample surface. The presence of Bi on the surface is not only evidenced by the Bi droplets in the ex-situ AFM measurement, but also evidenced by an *in-situ* ( $1 \times 3$ ) surface reconstruction persisting throughout the growth of GaAs cap layer. The growth of high quality GaAsBi/GaAs QWs depends upon the proper control of the Bi flux during the growth.

### 4.3 Effects of substrate temperature on the Bi composition

Fig 4.6 shows the PL peak wavelengths of GaAsBi bulk samples grown at the same condition but with different growth temperature. As can be seen, the peak wavelength considerably increases as the decrease of the substrate temperature. By properly controlling the growth temperature and Bi flux, the Bi composition can be effectively tuned in a wide range. As shown in Fig. 4.7, the bulk samples also show good optical properties at both low temperature and room temperature.

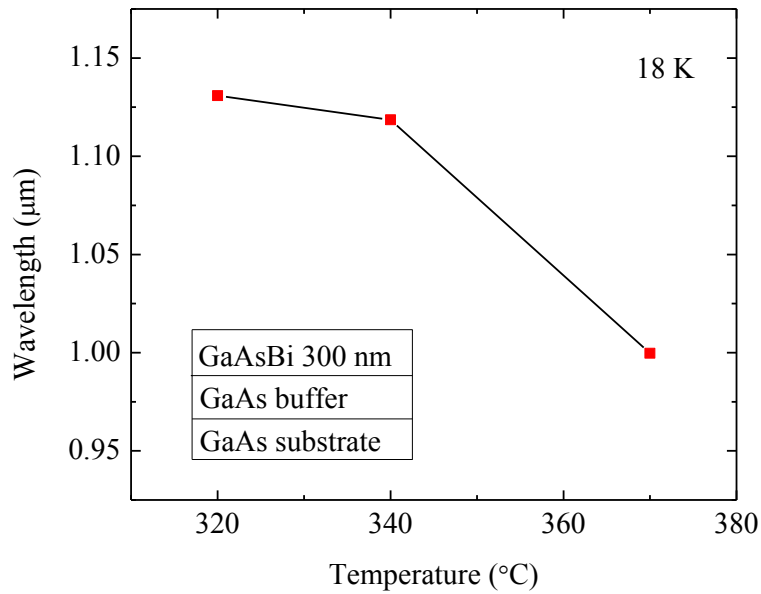


Fig. 4.6 PL peak wavelength of GaAsBi bulk samples grown at the same condition but with different growth temperatures. The emission wavelength increases steadily as decreasing temperatures.



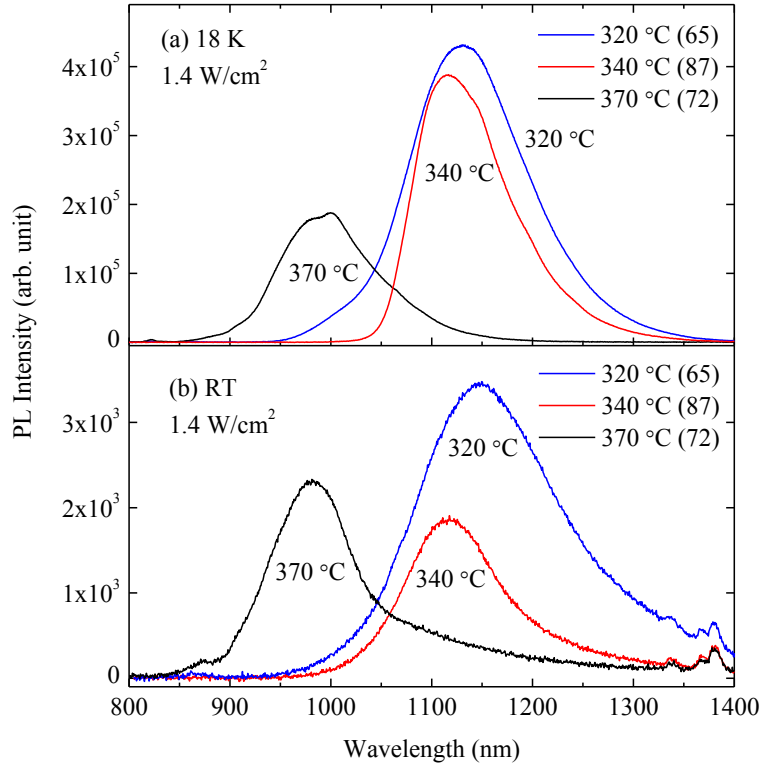


Fig. 4.7 PL spectra of the GaAsBi bulk samples measured at 18 K (a) and RT (b). The samples are grown at the same growth condition except with different Bi flux. The samples show good optical properties at both low temperature and room temperature.

#### 4.4 Structural Characterization of the GaAsBi/GaAs

The Bi composition and the layer thickness of the GaAsBi samples are determined by fitting the HRXRD (004)  $\theta$ - $2\theta$  scans using *Epitaxy and Smoothfit* software from *PANalytical Inc.* The parameters of Bi element and GaBi material have to be added into the database of the software in order to fit the rocking curves [159,160]. Since GaBi has not yet been synthesized, the crystal structural parameters of GaBi remain unknown. A generally accepted GaBi lattice constant of 6.324 Å is used in the database [3]. Fig. 4.8 shows the HRXRD (004)  $\theta$ - $2\theta$  scan of the

GaAsBi/GaAs QW sample with the best optical properties at 18 K (Sample C). The best fit value for the Bi composition is  $4.0\pm 0.5\%$ .

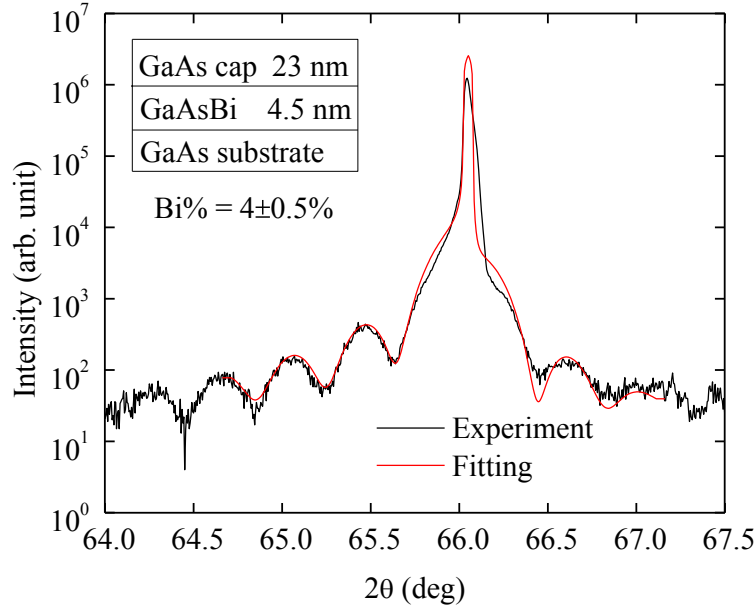


Fig. 4.8 HRXRD (004)  $\theta$ - $2\theta$  scan of a GaAsBi QW sample (Sample C). The red line is the best fitting of the experimental data and the best fit value of Bi composition is  $4.0\pm 0.5\%$ .

Cross-sectional TEM measurements are performed to investigate the structural properties of the sample. The low magnification high angle annular dark field (HAADF) STEM image of the sample in Fig. 4.1(3) shows smooth interfaces between the GaAsBi QW region and the GaAs layers. Moreover, clear lattice image of the layers can be seen in the high magnification bright field image of the sample as shown in Fig. 4.9, which demonstrates the good structural properties of the sample. The thickness of each layer in the sample agrees well with the HRXRD fitting.

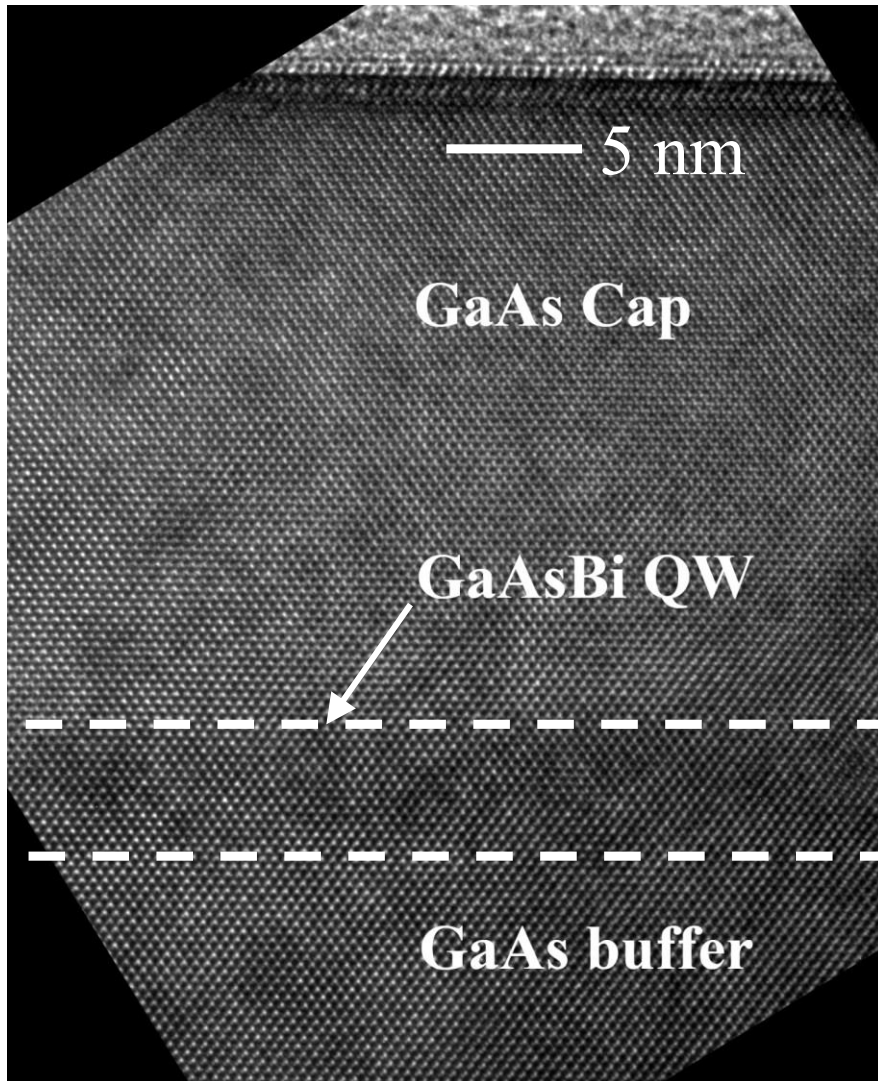


Fig. 4.9 High resolution bright field cross-sectional TEM image of a GaAsBi/GaAs QW sample (sample C). Clear lattice image of the layers can be seen.

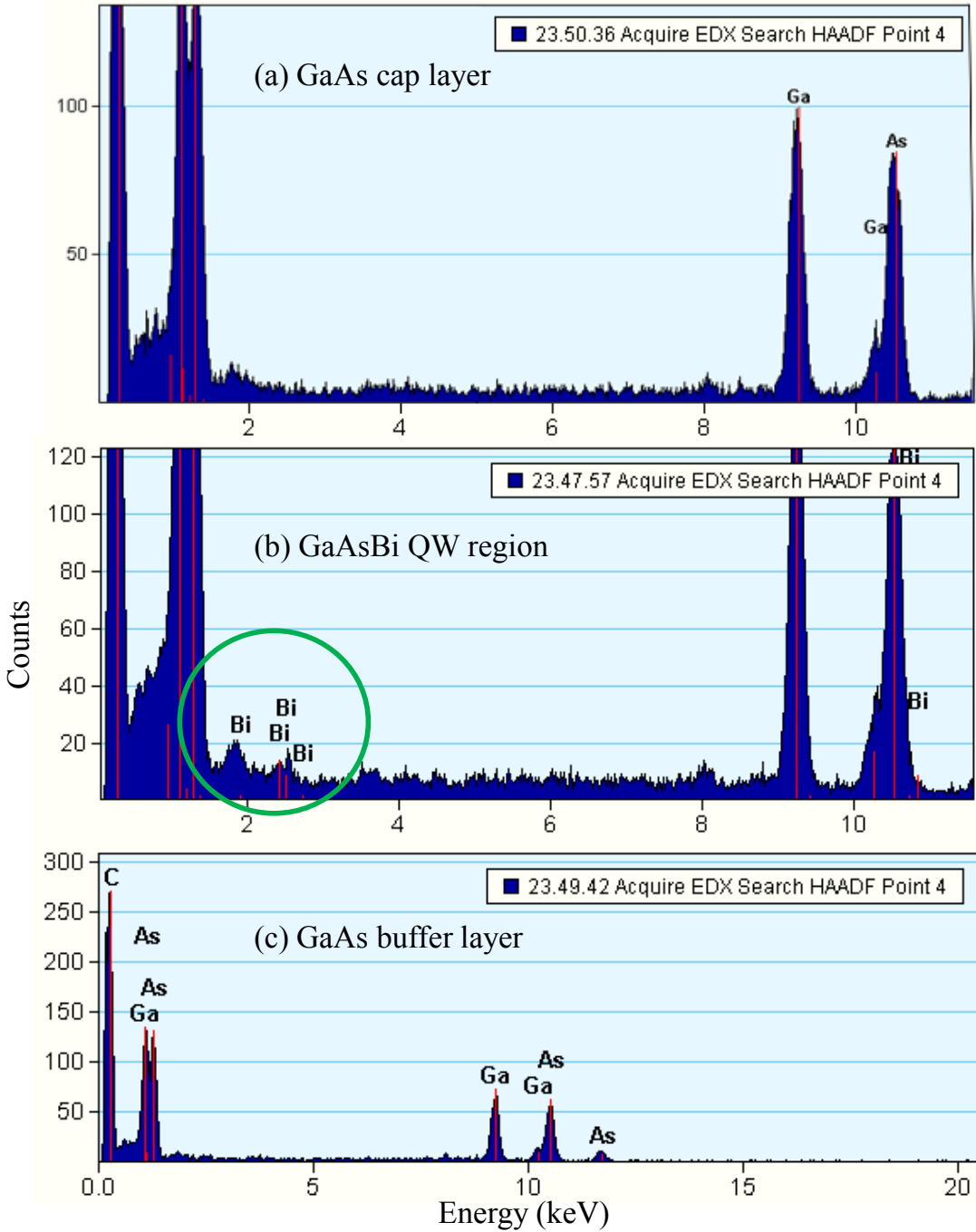


Fig. 4.10 EDS analysis of the GaAsBi/GaAs QW sample in GaAs cap layer (a), GaAs QW region (b), and GaAs buffer layer (c). The Bi peaks in (b) directly affirm the Bi's incorporation in GaAsBi QW region and the absence of Bi peak in (a) indicates that no detectable Bi is incorporated into the GaAs cap layer.

In addition, the energy dispersive X-ray spectroscopy (EDS) is used to characterize the GaAsBi/GaAs QW sample (sample C). Fig. 4.10 (c) shows the results of the GaAs buffer layer, which is used as the baseline in the following analyses. In the GaAsBi QW region, the Bi peaks can be clearly seen at the energy levels around 2 keV, as highlighted by the green circle in Fig. 4.10 (b). However, in the GaAs cap layer, no Bi peak is found in the analysis, as shown in Fig. 4.10 (a). The EDS analysis not only straightly affirms the Bi incorporation into GaAs in GaAsBi QW region, but also experimentally proves that no detectable Bi is incorporated in the GaAs cap layer. This direct evidence on the Bi distribution in the GaAsBi/GaAs QW sample leads to the discovery of the growth mechanism of Bi in the GaAsBi/GaAs QW growth. Considering the fact that the sample also has Bi droplets with the density of  $4.0 \times 10^6/\text{cm}^2$  left of on the surface, it is inferred that after the growth of GaAsBi QW region the surplus Bi atoms are floating on the growing surface rather than incorporating into the lattice until the end of GaAs cap layer growth, serving as the surfactant during the growth. The understanding and controlling of the roles of Bi during the growth of GaAsBi/GaAs QWs (incorporation vs. surfactant) enables the further development of quantum nanostructures toward high performance optoelectronic devices.

#### **4.5 Discussion of the growth of GaSbBi material**

GaSbBi material has been grown using MBE by Graf *et al.* [37] and Song *et al.* [38]. In Graf's work, up to 3% Bi has been achieved in GaSbBi alloys. More than 100 meV bandgap reduction has been confirmed by the red-shifted PL peaks [37]. In Song's work, only morphological and structural properties of the GaSbBi samples have been measured and no PL characterization has been reported [38]. It is particular interesting that the GaSbBi alloys show smaller lattice constants than GaSb ("lattice contraction"), which is explained by vacancies at group-V sites caused by Bi segregation [38].

The knowledge obtained in the growth of GaAs-based GaAsBi material can be used to grow GaSbBi material on GaSb substrates. Several guidelines should be followed in the growth of GaSbBi material such as near stoichiometry of V/III fluxes and low growth temperatures. In addition, several other factors should be carefully considered.

Firstly, the accurate substrate temperature is difficult to obtain in the MBE growth of GaSb material since the bandgap of GaSb is beyond the cut-off wavelength of the InGaAs detector used in the BandiT optical band gap thermometry. Therefore, the substrate temperature needs to be calibrated using the surface reconstruction transition from  $(1 \times 3)$  to  $(1 \times 5)$  [139,140].

Secondly, unintentional As incorporation during the growth of GaSbBi alloys should be taken into account due to the background As pressure. For example, a GaSb buffer layer was grown on Te doped n-type GaSb (001) substrates using a Riber-32P MBE system equipped with Ga effusion cells and a two-zone valved cracker cell for Sb. The oxide desorption was performed at 510 °C for 10 minutes followed by a 400 nm GaSb buffer layer grown at 480 °C at the growth rate of 0.5 ML/s. A  $(1 \times 3)$  RHEED reconstruction pattern was observed in the growth of GaSb buffer layers. Fig. 4.11 shows the HRXRD (004)  $\theta$ - $2\theta$  scan of the GaSb buffer layer grown on GaSb substrate. The buffer peak is clearly shown on the right side of the substrate peak, which indicating a smaller lattice constant of the buffer layer. It is attributed to the unintentionally incorporation of As during the buffer growth. Fitting of HRXRD scan suggests 0.58% As in the GaAsSb buffer layer. During the growth of GaSbBi, the effect of As atoms should also be considered.

The Ga(As,Sb,Bi) bulk samples were grown at 320 °C on the top of the GaAsSb buffer layers at the same growth rate (0.5 ML/s). Bi flux was kept at  $2.5 \times 10^{-7}$  Torr. During the MBE

growth, bright (1×3) surface reconstruction could be seen all the time. Fig 4.12 shows a  $2 \times 2 \mu\text{m}^2$  AFM image a Ga(As,Sb,Bi) sample, showing the atomically flat surface without droplet.

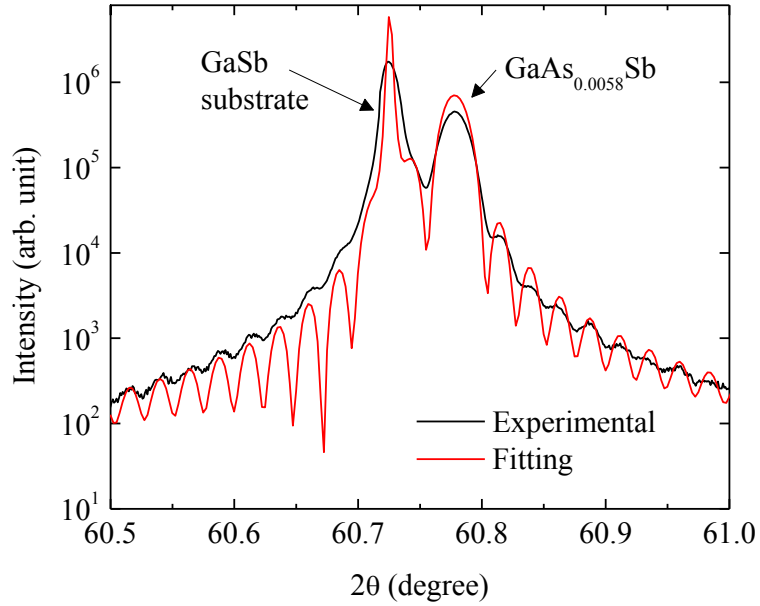


Fig. 4.11 HRXRD (004)  $\theta$ - $2\theta$  scan of the GaSb buffer layer grown on GaSb substrate, showing the unintentionally incorporated As in the GaSb buffer layer with As composition of 0.58%.

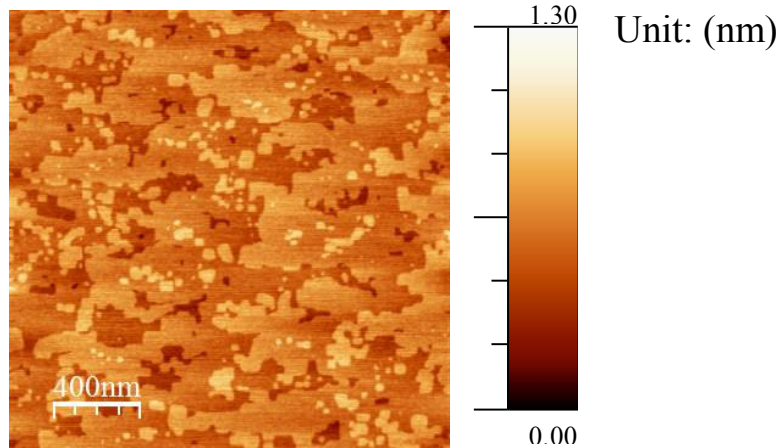


Fig. 4.12 A  $2 \times 2 \mu\text{m}^2$  AFM image a Ga(As,Sb,Bi) sample, showing the atomically flat surface without droplet.

Fig. 4.13 shows the HRXRD (004)  $\theta$ - $2\theta$  scan of the Ga(As,Sb,Bi) sample. An additional peak can be seen to the right of the GaAsSb buffer peak. Due to the defect induced lattice constraction of the GaSbBi alloys observed in previous research [37,38], it is hard to fit the HRXRD pattern using the normally used lattice constant for GaBi. Further characterization such as RBS or SIMS should be used to confirm the incorporation of Bi.

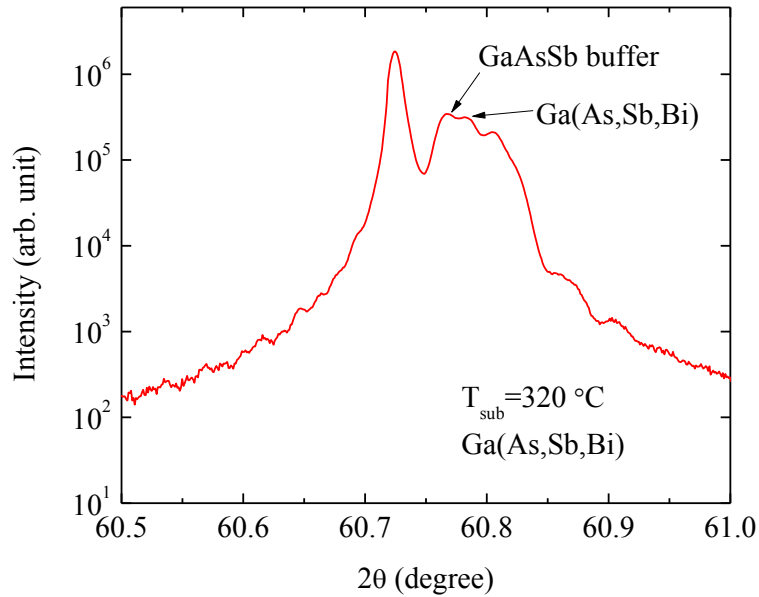


Fig. 4.13 HRXRD (004)  $\theta$ - $2\theta$  scan of the Ga(As,Sb,Bi) sample grown on GaAsSb buffer at 320 °C, showing the additional peak to due to the effect of Bi.

#### 4.6 Summary

In summary, the MBE growth of GaAsBi/GaAs material has been systematically studied under a variety of growth parameters. The effects of Bi flux and growth temperature on the properties of the material are extensively investigated. It is revealed that at certain temperature the Bi composition in GaAsBi/GaAs QW region increases linearly with the increase of Bi flux before reaching the saturation limit. On the other hand, the saturation limit increases with the



decreasing growth temperature. Therefore, by properly setting the Bi flux and the growth temperature, the Bi composition can be effectively tuned in a wide range. Moreover, it is discovered that Bi flux plays a critical role on the optical properties of the GaAsBi/GaAs QW structures. Too little Bi flux Bi won't provide enough surfactant effect for the following GaAs cap layer growth while too much Bi flux will results in massive droplets on the surface. In both cases, the optical properties would be deteriorated. As a result, the best growth condition lies in the intermediate Bi flux range before reaching the saturation limit. In our experiments, the samples grown under the optimal growth conditions show excellent structural properties in the HRXRD, TEM and EDS measurements and excellent optical properties by exhibiting strong RT PL. The successful growth of high quality GaAsBi/GaAs material system enables the further development of this material system towards high performance optoelectronic devices.



## 5 GAASBI SEPARATE CONFINEMENT HETEROSTRUCTURES

### 5.1 Motivation

Due to the great potential of GaAsBi/GaAs material system in the applications for long-wavelength optoelectronic devices, a lot of nanostructures, such as GaAsBi/GaAs SQWs, GaAsBi/GaAs multiple quantum wells (MQWs), and GaAsBi/AlGaAs MQWs, have been grown using MBE or MOVPE at low temperatures ( $\sim 280$  °C to 400 °C) [17-29, 78-81]. In device development aspect, LEDs and optically pumped lasers have been fabricated using GaAsBi/GaAs SQW structures and bulk double heterostructures respectively [100-103]. However, GaAsBi/GaAs laser diodes have not been realized yet.

In order to obtain lasing characteristics in the devices, it is highly desirable to incorporate SCHs and MQWs into the active regions. SCHs have been widely used in laser diode designs to achieve the highest device performance [161,162]. In GaAs-based SCH designs, AlGaAs is typically used as the barrier material because it is not only lattice matched to GaAs, but also has a wider bandgap and smaller refractive index, which are favorable for device applications [2,163].

On the other hand, MQWs are often used in the device designs to increase the modal gain. The gain of the GaAsBi/GaAs material system, which is similar to GaAsSb/GaAs material system [164-166], is very likely restricted by a less than ideal electron-hole wave-function overlap due to the weak confinement of electrons and strong confinement of holes. This is ascribed to the weak type-I band alignment between GaAsBi and GaAs [77,86,88]. Moreover, compared with SQW designs, MQW designs are capable of achieving lower carrier density in QW regions to minimize the Auger recombination, which is especially favorable for light

emitting devices working in long wavelength range where the device performance is afflicted by severe Auger recombination [167].

The growth of the GaAsBi/GaAs/AlGaAs SCH, however, is challenging because the typical growth temperatures of GaAsBi (~300 °C) is far below that of AlGaAs (~610 °C). In SCH growth, if the top AlGaAs barrier is grown at an elevated temperature after the growth of GaAsBi QW, the GaAsBi region will be annealed at the high temperature, which would degrade the optical quality of the GaAsBi QW due to Bi inter-diffusion and segregation. The growth temperature of AlGaAs is thus restricted by the temperature at which the GaAsBi material can be annealed without quality degradation. It has been reported that the optimal rapid thermal annealing (RTA) temperature of GaAsBi QWs decreases with the increase of Bi composition, where, for instance, at Bi composition of 6.5% the optical properties degrade at temperatures above 600 °C [168]. In fact, the growth temperature for the top AlGaAs layer should be much lower than the optimal RTA temperature of the GaAsBi QW because the growth time of a typical AlGaAs cladding layer is much longer than the duration of a RTA process. The annealing duration in a RTA cycle, for example, is typically within one minute, while the duration of growing the top AlGaAs cladding layer of a device structure is often longer than an hour. The annealing effect on GaAsBi material caused by the high temperature AlGaAs cladding growth is therefore substantially severe than that caused by RTA. As a result, in the GaAsBi/GaAs/AlGaAs SCH, the top AlGaAs barrier has to be grown at a much lower temperature to avoid the annealing effect caused by high temperature growth.

However, when GaAs and AlGaAs are grown at temperatures below 450 °C under conventional As-rich conditions, the optical and electrical properties of both degrade drastically due to the formation of Ga-vacancy complex defects [169,170]. In fact, at growth temperatures

below 300 °C, AlGaAs and GaAs grown under As-rich conditions are nonstoichiometric with excess As incorporated as arsenic antisite defects and gallium vacancies, which makes AlGaAs and GaAs optically and electrically inactive [171,172].

Several methods have been developed to grow high optical and electrical quality AlGaAs and GaAs at low temperatures, including migration enhanced epitaxy (MEE) and stoichiometric low temperature (SLT) MBE growth. In MEE growth, group III elements (Ga and/or Al) and Group V element (As) are supplied to the growing surface alternately under ultrahigh vacuum [173]. When group III elements are deposited under As-free condition or at an extremely low As pressure, the average times for Ga and Al atoms on the growth surface before reacting with As become much longer than those under a high As pressure condition, which leads to longer migration lengths of Ga and Al atoms [174]. Thus Ga vacancies and arsenic antisite defects are prevented. As a result, the optical properties of the material grown by MEE are improved. Nevertheless, this method not only requires a specially designed shutter in the MBE chamber to ensure the alternate deposition of group III and group V elements without flux leakage [174], but also has very low growth rate [173], which limits its throughput and applicability. In SLT MBE growth, on the other hand, the As pressure is significantly reduced to a value near the stoichiometry of group III and group V elements to suppress the excess As incorporation [175,176]. Although good optical properties have been achieved using SLT MBE, this technique requires stringent control of the As/Ga flux since even a small As flux deviation from near stoichiometry can lead to excess As incorporation in quantities comparable to that of high flux ratios [171]. The small growth window and low repeatability of this approach therefore limit the growth technique from being widely used.

In this work, we propose to use Bi surfactant mediated growth to grow high quality AlGaAs at low temperatures around 300 °C. Although Bi has been widely used as a surfactant to promote 2D layer-by-layer growth, reduce interface roughness, and improve PL efficiency in GaN, GaNAs, InGaAs, and GaInP growth [143-154], its effect has not been explored at temperatures as low as ~300°C. The role of Bi as a surfactant can be interpreted as increasing the diffusion length of the adatoms on the growth surface, which is similar to the effect of MEE and makes it possible to grow high quality material at lower growth temperatures. Typically the GaAsBi material is grown at low temperatures (280 °C to 400 °C) and near stoichiometry of the As:Ga ratios to facilitate Bi to incorporate. In the non-stoichiometric (As rich) condition, the presence of excess As on the surface prevents Bi from incorporating into the lattice, which results in Bi segregating on the growth surface and serving as the surfactant during the growth. Moreover, even after the Bi flux is closed, the Bi atoms would remain on the growth surface for a very long time (> 10 minutes at temperature < 420 °C [10]) due to the low desorption rate, which can be confirmed by the (1 × 3) surface reconstruction during the growth. The characteristics of Bi as a surfactant have thrown great light on the growth of high quality GaAsBi/GaAs/AlGaAs SCHs.

## **5.2 SQW SCH development**

In our experiment, both the SCH sample (sample A) and the single QW control sample without separate confinement (sample B) are grown on semi-insulating GaAs (001) substrates using MBE. The structural diagrams and temperature profiles of both samples are displayed in Fig. 5.1.

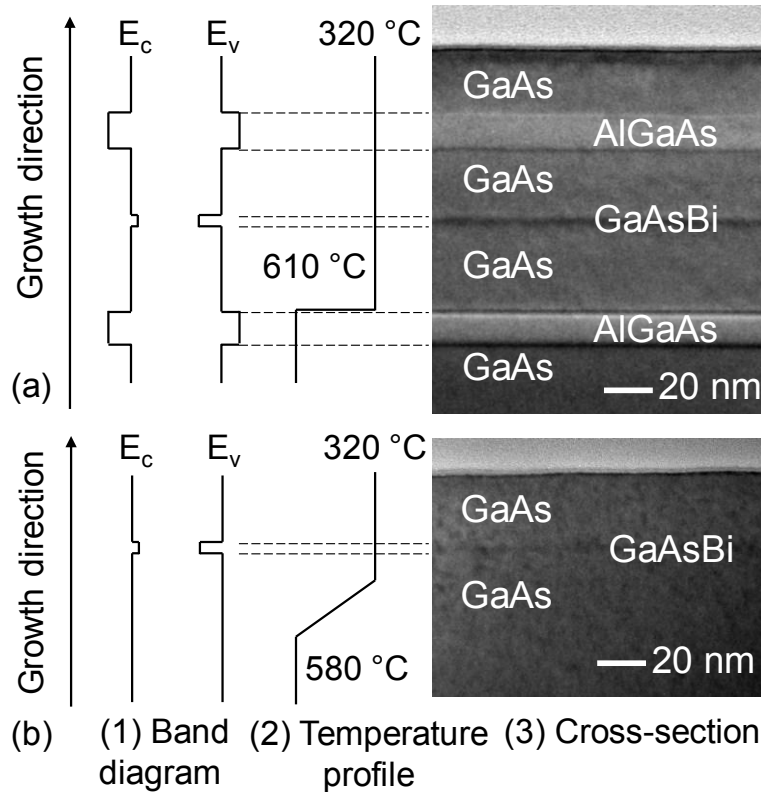


Fig. 5.1 Band diagrams, growth temperature profiles and cross-sectional TEM images of sample A with separate confinement (a) and sample B without separate confinement (b). The upper AlGaAs barrier in sample A is grown at the GaAsBi growth temperature 320 °C. Reprinted with permission from [D. Fan, *et al.*, “Molecular beam epitaxy growth of GaAsBi/GaAs/AlGaAs separate confinement heterostructures”, *Appl. Phys. Lett.*, vol. 101, pp. 181103, 2012]. Copyright [2012], American Institute of Physics.

To grow sample A, firstly the oxide desorption is performed at 610 °C for 10 minutes followed by a 400 nm GaAs buffer layer and 12 nm  $\text{Al}_{0.3}\text{Ga}_{0.7}\text{As}$  barrier layer grown at 610 °C. A growth interruption of 20 minutes is then utilized to decrease the substrate temperature to 320 °C and Ga flux to 0.35 ML/s. After which a 30 nm GaAs barrier, a 5 nm GaAsBi QW, a 23

nm GaAs layer, a 12 nm AlGaAs barrier and a 23 nm GaAs cap layer are successively grown without growth interruption to avoid any consequence of increasing the growth temperature after the GaAsBi QW region is grown. A  $(2 \times 1)$  RHEED reconstruction pattern is observed during the growth of GaAsBi while a  $(1 \times 3)$  pattern is observed for the layers after the GaAsBi QW region. For comparison, the control sample, sample B, consisting of a 5 nm GaAsBi QW region and a 23 nm GaAs cap layer on top of a 400 nm GaAs buffer layer, is grown under the same growth conditions as SCH sample A.

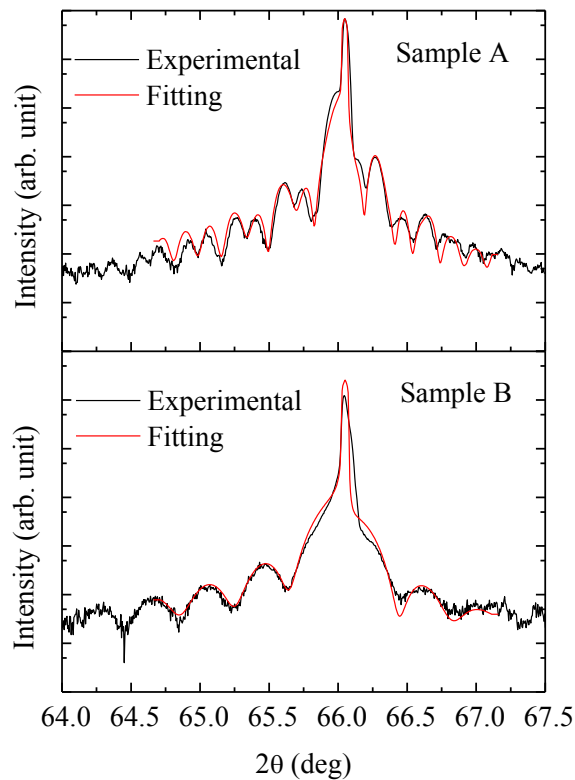


Fig. 5.2 High-resolution x-ray diffraction patterns of  $\theta$ - $2\theta$  scans from (004) planes of sample A and sample B. The red lines are the best fit models of the experimental data. Reprinted with permission from [D. Fan, *et al.*, “Molecular beam epitaxy growth of GaAsBi/GaAs/AlGaAs separate confinement heterostructures”, *Appl. Phys. Lett.*, vol. 101, pp. 181103, 2012]. Copyright [2012], American Institute of Physics.



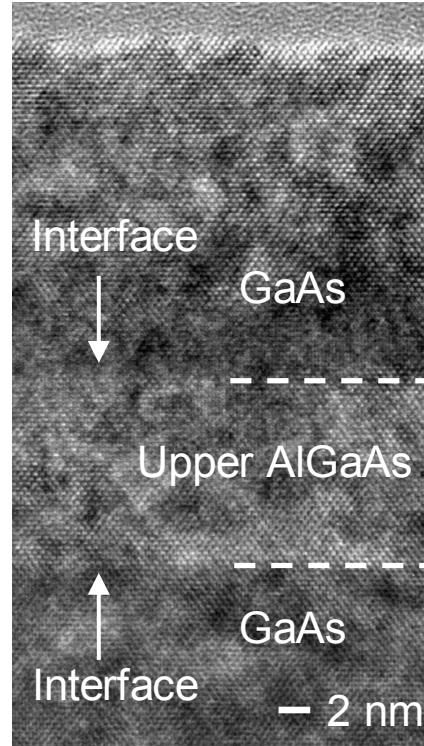


Fig. 5.3 High resolution bright field cross-sectional TEM image of sample A with separate confinement. Reprinted with permission from [D. Fan, *et al.*, “Molecular beam epitaxy growth of GaAsBi/GaAs/AlGaAs separate confinement heterostructures”, *Appl. Phys. Lett.*, vol. 101, pp. 181103, 2012]. Copyright [2012], American Institute of Physics.

The  $\theta$ - $2\theta$  scans of the (004) HR XRD pattern of samples A and B are shown in Fig. 5.2. The best fit values for the Bi concentration of both samples are  $4.0 \pm 0.5\%$  (see solid red curve in Fig. 5.2). Cross-sectional TEM measurements are used to investigate the structural properties of the samples. The low magnification TEM image of sample A in Fig. 5.1 (a) indicates a smooth interface between the upper AlGaAs barrier and GaAs layers. The thickness of each layer in sample A agrees well with the XRD fitting. Clear lattice image of the upper AlGaAs layer can be seen in the high magnification bright field image of sample A (see Fig. 5.3). Sharp interfaces

between AlGaAs and GaAs layers are displayed as well, which is expected since the inter-diffusion between the layers is substantially reduced because of the low growth temperature.

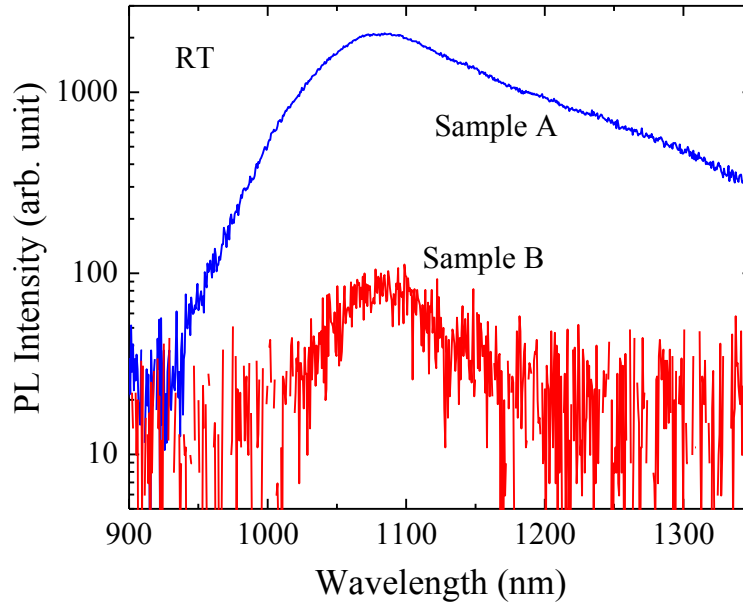


Fig. 5.4 Photoluminescence spectra at RT: Sample A with separate confinement (blue curve) and Sample B without separate confinement (red curve). The photoexcitation density is  $1.4 \text{ W/cm}^2$  and the PL peak intensity of sample A is  $\sim 10$  times higher than that of sample B. Reprinted with permission from [D. Fan, *et al.*, “Molecular beam epitaxy growth of GaAsBi/GaAs/AlGaAs separate confinement heterostructures”, *Appl. Phys. Lett.*, vol. 101, pp. 181103, 2012]. Copyright [2012], American Institute of Physics.

PL is used to study the optical properties of the samples. The photoexcitation density used is  $1.4 \text{ W/cm}^2$ . As shown in Fig. 5.4, the PL intensity of sample A at RT is more than 10 times higher than that of sample B. This is interpreted as the increased carrier injection due to the SCHs. The pumping radiation intensity in the samples can be expressed as  $I = I_0 e^{-\alpha z}$ , where  $I_0$  is the intensity on the sample surface,  $\alpha$  is the absorption coefficient, and  $z$  is the distance from

the surface into the sample. The absorption coefficient of GaAs is taken as  $8.0 \times 10^4 \text{ cm}^{-1}$  at the excitation laser wavelength in this PL measurement [177,178].

In sample B which has single QW structure, only ~3% of the pump radiation that enters into the sample is absorbed in and near the 5 nm-thick quantum well region and recombine radiatively. Most of the carriers generated in the GaAs cap layer are wasted by combining through nonradiative recombination centers on the sample surface. Whereas in sample A, which has separate confinement, much more photo-generated carriers would be confined between the two  $\text{Al}_{0.3}\text{Ga}_{0.7}\text{As}$  layers because the band alignment offsets of GaAs/ $\text{Al}_{0.3}\text{Ga}_{0.7}\text{As}$  are relatively big (0.22 eV for electrons and 0.16 eV for holes [2]), which prevents the carriers recombining nonradiatively through defect states on the sample surface. The absorbed pumping radiation in GaAs/GaAsBi/GaAs region is about ~28% of the total radiation that enters the sample and increases ~9.3 times as much as that of simple QW sample B, which results in a much higher carrier injection level.

The significant enhancement of the PL of sample A confirms the high optical quality of the top AlGaAs barrier even though its growth temperature is as low as 320 °C. This can be explained as follows: After the growth of GaAsBi QW, there are still lots of Bi atoms on the growing surface, which significantly affect the growth of the subsequent GaAs and AlGaAs layers before they fully desorb from the surface or incorporate into the lattice. However, during the growth of GaAs and AlGaAs layers, Bi atoms are less competitive than As atoms in incorporating into GaAs lattice since the As flux is increased by 2.4 times after the growth of GaAsBi QW, which substantially reduces the Bi incorporation. Meanwhile, at the growth temperature of 320 °C the surface residence time of the Bi atoms is so long that the competitive desorption of Bi can be ignored [10]. As a result, the Bi atoms remain on the growing surface

during the low temperature growth of GaAs and AlGaAs as indicated by the  $(1 \times 3)$  RHEED pattern, acting as the surfactant to increase the diffusion length of Ga and Al atoms, which promotes layer by layer growth and improves the optical properties of the layers.

### **5.3 Double quantum well development**

This section studies the MBE growth of GaAsBi/GaAs DQWs. Structural properties of the samples are investigated using HRXRD and TEM. Optical properties of the samples are studied using low temperature and RT PL. We demonstrate the feasibility of growing identical QWs in the DQW structure without growth interruption by investigating the behavior of Bi during the DQW growth. The elimination of growth interruption in the QW regions prevents the contamination precipitation in the MBE chamber and improves the interface quality. This approach can be further extended to grow MQWs that contain more identical QWs for higher modal gain.

In our experiment, samples are grown on semi-insulating GaAs (001) substrates using MBE. For the SQW reference sample (sample B) and DQW samples (sample C, sample D, and sample E), GaAsBi QWs, GaAs spacers, and GaAs cap layers are all grown at 320 °C without growth interruption. The GaAsBi QW regions of all samples have a nominal thickness of 7 nm and are grown without any growth interruption to prevent contamination precipitation in the MBE chamber to improve the interface quality. In order to investigate the controllability and tunability of Bi compositions and well widths in the two individual QWs in DQW structures, two DQW samples are grown at the same growth condition except that sample C is with 7.5 nm-thick GaAs spacer layer while sample D is with 15 nm-thick GaAs spacer layer. The same Bi flux is used for the two QW regions in samples C and D.

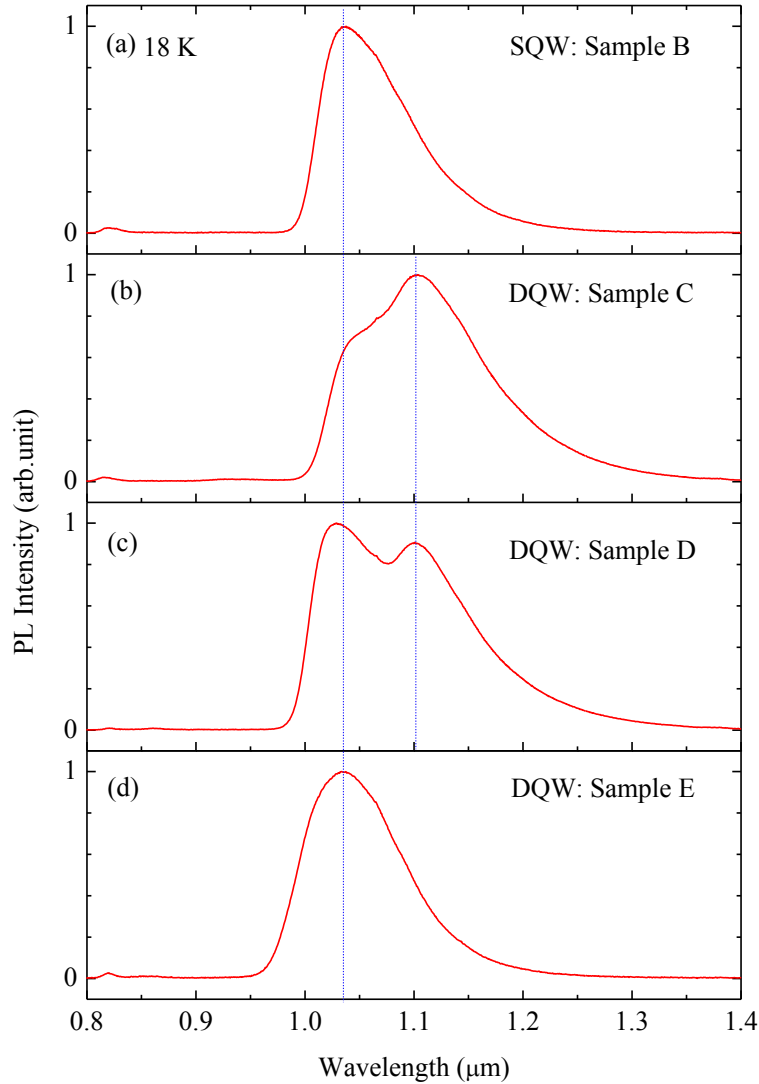


Fig. 5.5 PL spectra of samples B, C, D, and E measured at 18 K: (a) Sample B (SQW reference sample); (b) Sample C (with a 7.5 nm-thick GaAs spacer); (b) Sample D (with a 15 nm-thick GaAs spacer); (d) Sample E (with 7.5 nm-thick GaAs spacer and reduced Bi flux for the second QW growth). Reprinted with permission from [D. Fan, *et al.*, “MBE Grown GaAsBi/GaAs Double Quantum Well Separate Confinement Heterostructures”, *J. Vac. Sci Technol. B*, vol. 31, pp. 03C105, 2013]. Copyright [2013], American Vacuum Society.

Fig. 5.5 displays the PL spectra of the samples at 18 K. Low-density excitation is used in the PL measurements to ensure the spectra from the ground-state transitions. It can be seen that samples C and D show two peaks, suggesting that the two QWs in the samples have different ground-state transition energies. Compared with SQW sample B, samples C and D have additional peaks at a longer wavelength around 1102 nm. This indicates that the second QWs in the DQW structures have lower ground-state transition energies than those of the first QWs and the two QWs in the DQW structures are not identical.

Fittings of the  $\theta$ - $2\theta$  scans of the (004) HRXRD patterns of samples C and D show that the widths of the first QWs are 2.5 nm thinner than expected and those of the second ones agree with the nominal value. The second QWs, however, have 0.5 % higher Bi composition than the first ones, which explains the red-shifting of the PL peaks of the second QWs. The inconsistent Bi compositions and QW widths can be explained as follows: When Bi shutter is opened to grow the GaAsBi layer under near stoichiometry of group III and group V atoms, it takes some time for the Bi atoms to accumulate on the surface before being incorporated into the GaAs lattice, which results in reduced QW width than expected. After the growth of GaAsBi QW region, As flux is increased by 2.4 times, which effectively suppresses Bi incorporation due to non-stoichiometry of group III and group V atoms. The  $(1 \times 3)$  surface reconstruction during the GaAs spacer layer growth gives the indication that the residual Bi atoms stay on the growing surface after the first QW growth and serve as surfactants. Consequently, during the growth of the second QW, As flux is reduced to near stoichiometry of group III and group V atoms. Bi atoms start to incorporate shortly after the Bi shutter is opened since the Bi atoms left on the growing surface have greatly shortened the accumulation process, resulting in nearly unaffected QW thickness and increased Bi composition. The nearly identical PL peak positions of the

second QWs in the two samples with different GaAs spacer thickness suggest that the Bi composition in the second QWs is not sensitive to the spacer thickness. This proves that the desorption of Bi atoms is negligible during the LT growth of GaAs spacer layer, which agrees with the report of the extremely low desorption rate of Bi at LT [10].

Understanding the exact behavior of Bi during the GaAsBi QW growth is of great importance because of the dual mechanisms of Bi in LT growth, alloying with GaAs and serving as surfactant. The knowledge derived from our observation enables us to manage to control closely relevant parameters to achieve the expected design characteristics. For example, in order to achieve the same QW thickness in the DQW structures, an offset value should be added to the nominal value of the first QW thickness (in our case, 2.5 nm for sample C and D with Bi composition around 3.5%) to compensate for the reduced QW width due to the Bi accumulation process at the beginning of the first QW growth. The PL peak position of the second QW can be tuned as well by varying its Bi composition to match with that of the first one. We design sample E whose structure is the same as sample C except that the Bi flux for the second QW region is reduced by 25%. Fig. 5.5(d) and Fig. 5.6 show the sample exhibits a single PL peak at both 18 K and RT. Compared with sample B in Fig. 5.5(a), the PL spectrum of sample E in Fig. 5.5(d) is slightly broader at the short wavelength side, suggesting that the ground-state transition energy of the second QW in sample E is slightly higher than that of the first QW. Further fittings of the  $\theta$ - $2\theta$  scans of the (004) HRXRD pattern reveals that there is still slight discrepancy between the Bi compositions of the two QWs. It is expected that the same Bi composition of the second QW can be achieved by carefully tuning the Bi flux for the second QW growth.

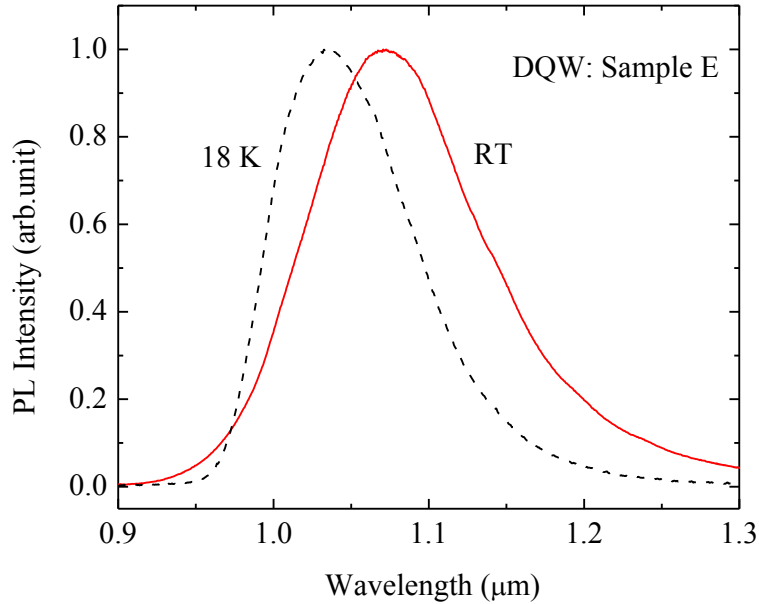


Fig. 5.6 PL spectra of DQW sample E at 18 K (black dash-line) and RT (red solid-line) to show that the sample exhibits a single PL peak at both temperatures. Reprinted with permission from [D. Fan, *et al.*, “MBE Grown GaAsBi/GaAs Double Quantum Well Separate Confinement Heterostructures”, *J. Vac. Sci Technol. B*, vol. 31, pp. 03C105, 2013]. Copyright [2013], American Vacuum Society.

#### 5.4 Integration of DQW and SCH designs

With the growth of high quality SCH and DQW structures successfully accomplished, the DQW SCH (sample F) is finally developed to integrate the DQW and the separate confinement designs, which is vital for future device development. The growth condition of sample F is similar to that of the SQW SCH samples except that the DQW SCH has two QW regions and one GaAs spacer between the two QWs. The structural diagrams and temperature profiles of the sample are shown in Fig. 5.7.



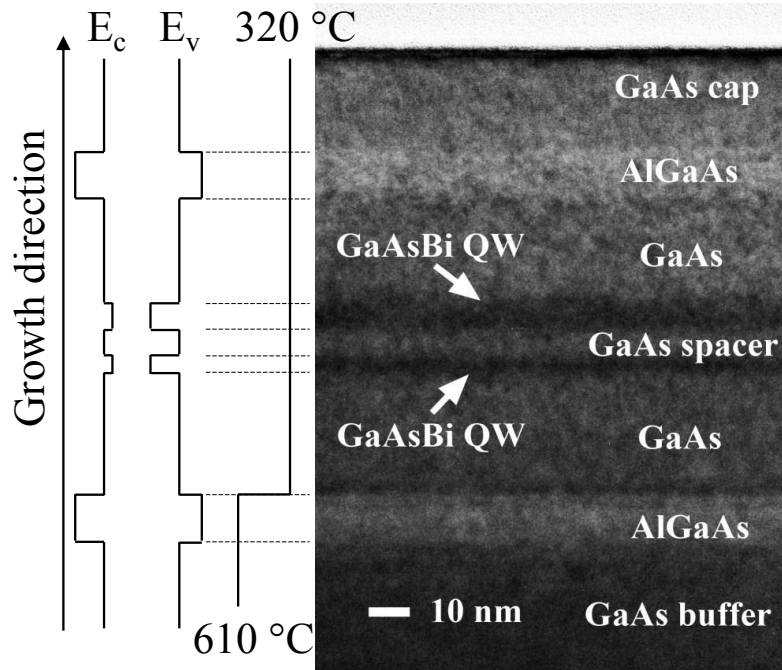


Fig. 5.7 Schematic of cross-section with growth temperature profile and low magnification bright field cross-sectional TEM image of DQW SCH sample (sample F) to show smooth interfaces between the different layers. Reprinted with permission from [D. Fan, *et al.*, “MBE Grown GaAsBi/GaAs Double Quantum Well Separate Confinement Heterostructures”, *J. Vac. Sci Technol. B*, vol. 31, pp. 03C105, 2013]. Copyright [2013], American Vacuum Society.

Cross-sectional TEM is used to investigate the structural properties of the sample. Fig. 5.7 shows the low magnification TEM image of sample F, from which GaAsBi QWs, GaAs spacer, GaAs barriers, AlGaAs barriers and GaAs cap layer can be clearly seen. Smooth interfaces between the layers are shown as well.

The sample exhibits strong RT PL as displayed in Fig. 5.8. The PL peak intensity is at the same order and the peak wavelength is about the same with that of the SQW SCH reference

sample (sample A) [158]. The width of the spectrum is broader than that of sample A. This is due to the variation of Bi composition in the two QWs in sample F. The excellent optical properties are attributed to the beneficial effect of Bi serving as the surfactant, as indicated by the  $(1 \times 3)$  surface reconstruction persisting throughout the growth of GaAs spacer layer, GaAs barrier, top AlGaAs barrier and GaAs cap layer at LT.

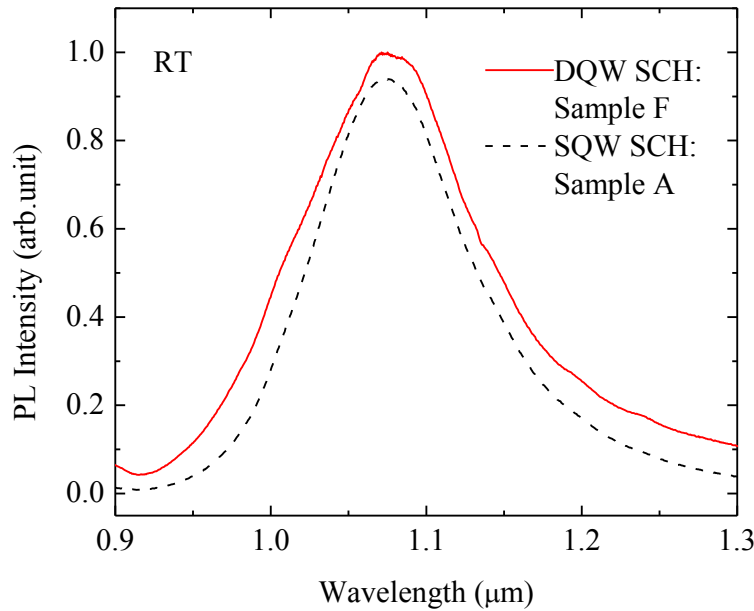


Fig. 5.8 A comparison of RT PL spectra of DQW SCH sample (sample F, red solid-line) and SQW SCH reference sample (sample A, black dash-line) to show high optical quality of the DQW SCH. Reprinted with permission from [D. Fan, *et al.*, “MBE Grown GaAsBi/GaAs Double Quantum Well Separate Confinement Heterostructures”, *J. Vac. Sci Technol. B*, vol. 31, pp. 03C105, 2013]. Copyright [2013], American Vacuum Society.

The approach of growing GaAsBi/GaAs DQWs and DQW SCHs without growth interruption can be applied directly to grow MQWs and MQW SCHs in a variety of settings. In the design of a MQW structure, the thickness of the first QW needs to be compensated by an

offset calibrated from the growth and the thickness of the rest of the QWs can be designed in accordance to the nominal value. Meanwhile, the Bi flux should be calibrated for the growth of each QW region to achieve the same Bi composition among all of the QWs.

The PL spectrum of a GaAsSb SQW sample, which was grown under optimal growth condition during the development of RT CW operational 1.3  $\mu\text{m}$  laser diodes [165,166], is used to benchmark the PL intensity of the GaAsBi samples. Fig. 5.9 shows the PL comparison between the benchmark sample and the most frequently used GaAsBi SQW reference sample in this work (sample B). Although the PL line-width of sample B is much broader than that of the reference GaAsSb SQW sample, its PL peak intensity is comparable to that of the reference, indicating good optical properties of the GaAsBi samples.

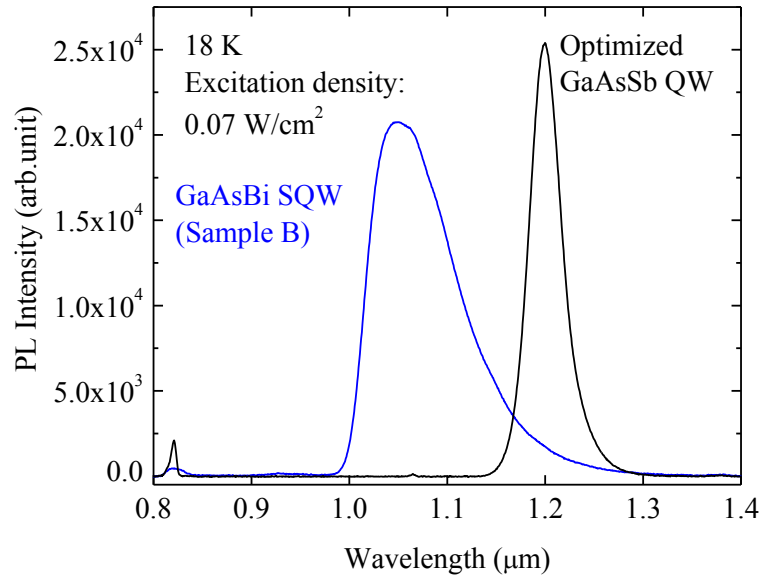


Fig. 5.9 PL comparison between a SQW GaAsBi sample (sample B) and an optimized GaAsSb SQW benchmark sample, indicating good properties of the GaAsBi sample.

## 5.5 Summary

In summary, GaAsBi/GaAs/AlGaAs SQW SCHs have been successfully grown using MBE with the top AlGaAs barrier layers grown at the unconventional low temperature 320 °C. Cross-sectional TEM images show smooth and sharp interfaces between the low temperature AlGaAs layer and adjacent GaAs layers. The separate confinement design enhances the room temperature PL intensity by more than 10 times due to improved carrier injection. The high quality of the low temperature AlGaAs barrier is attributed to the beneficial effect of Bi serving as the surfactant during the low temperature growth, which is evidenced by the presence of a (1 × 3) surface reconstruction throughout the growth of the low temperature AlGaAs.

Moreover, GaAsBi/GaAs DQWs and DQW SCHs have been developed using MBE. It has been demonstrated that identical QWs can be realized by controlling the Bi flux and QW thickness without growth interruption. The DQW SCH shows not only good structural properties in cross-sectional TEM measurement, but also good optical properties as exhibiting strong RT PL. The proposed approach can be extended to grow laser diode structures with MQW SCHs containing more identical QWs. The growth of the high quality DQW SCH integrates separate confinement designs and multiple QW designs into GaAsBi/GaAs material and enables the further development of the material system towards high performance optoelectronic devices.

## 6 DEVICE FABRICATION

### 6.1 Motivation

With high quality MQWs and SCHs developed, the GaAsBi/GaAs material system is ready to be used to fabricate optoelectronic devices, such as laser diodes, LEDs and photo-detectors. Accordingly, reliable process flows should be developed for the device fabrication. Compared with the Si-based process, the process for III-V material system in the lab environment has a wide variety of differences.

Firstly, the Si-based process usually works on cheap Si wafers, while the III-V-based process works on much expensive III-V wafers. This is not only because of the high prices of the III-V substrates, but also because of the costs and values that have been added to the substrates by MBE or MOCVD material growth. For example, the typical price for a 2-inch Si bare wafer is less than \$10 and the typical price for a same size bare GaAs wafer is ~\$150. Meanwhile, the related cost of growing the device structures on the III-V substrates can easily exceed \$1000. As a result, the cost of the III-V samples is two orders of magnitude higher than that of Si samples. Therefore, low yield and low reliability processes are hardly acceptable.

Secondly, the III-V-based process usually has lower yield than the Si-based process since the III-V wafers are considerably more fragile than the Si ones. Especially when the bottom contact is used in the process flow, the substrate needs to be thinned to  $\sim 100 \mu\text{m}$  in thickness by using the lapping process before the bottom metal is deposited. During these processes, the sample is extremely fragile and vulnerable to huge yield loss. Special measures therefore need to be taken during the processing to minimize the catastrophic yield loss due to sample breaking.

Thirdly, III-V-based process often has to deal with samples in small or tiny size. In our research group, a quarter of 2-inch and 20 mm × 20 mm are the most frequently used sizes of wafers for the MBE growth. After the growth, a part of the sample will be cut for the device fabrication and some other parts will be reserved for other characterizations such as PL and TEM measurement. In fact, 10 mm × 10 mm in size is not uncommon for the samples in device fabrication. The size of samples imposes great complexity to the process not only because of the difficulty of sample handling but also because of the incompatibility of some instruments with the small size samples. Extra efforts such as designing special adapters have to be exerted during the processing to cater for the small size samples.

The significant differences between the III-V-based process and the Si-based process require well-designed process flows to address the processing flexibility, capability and reliability problems as stated above. Our goal is to build a set of process flows which can be used for the high performance optoelectronic device fabrication.

In this work, we develop a set of process flows by integrating the process steps in HiDEC and Nano-fab facilities, which consist of photolithography, wet etching, Plasma-enhanced chemical vapor deposition (PECVD), ebeam evaporation, lift-off, lapping, RTA and etc. The resolution and overlay of the processes achieve 2 μm and 1 μm respectively. Photomasks for laser diodes, LEDs and photo-detectors are designed and fabricated. High performance GaAs QW laser diodes and InAs QD LEDs are fabricated to demonstrate the excellent quality of the process flows.

## 6.2 Process flows

The edge emitter is one of the most typical optoelectronic devices and is widely used in industry and scientific research. Fig. 6.1 shows the schematic diagram of an edge emitter, which contains p-type metal on the top, MESA waveguide and active region in the middle, and n-type metal in the bottom.

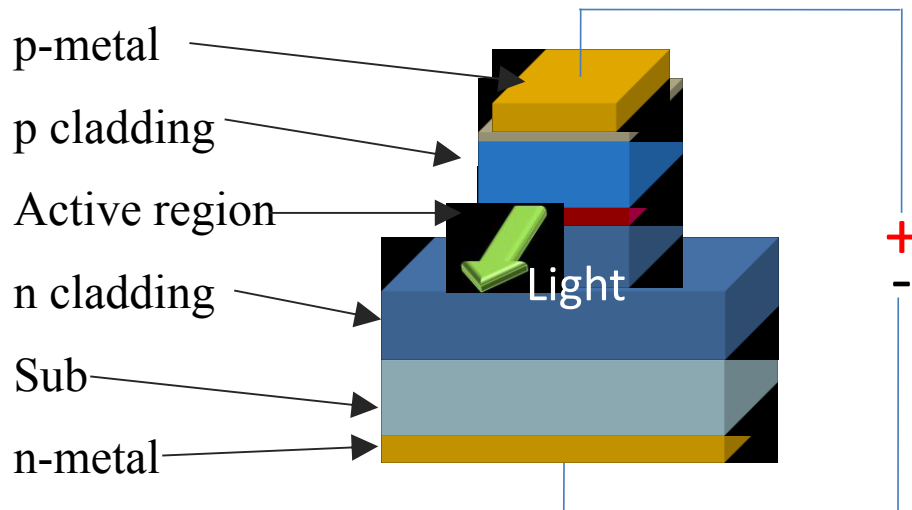


Fig. 6.1 Schematic diagram of an edge emitter.

The process flow is used to define and transfer the designed patterns onto the substrates. Fig. 6.2 shows a process flow to fabricate edge emitters with double side metal deposition and oxide isolation layer. Oxide buried design and large contact pad are to facilitate the wire-bonding in the packaging. The process flow includes 8 major steps: sample preparation, MESA etching, SiO<sub>2</sub> deposition, SiO<sub>2</sub> window opening, p-metal deposition, substrate thinning, n-metal deposition, and RTA. Three lithography processes are needed in this process, for MESA etching, SiO<sub>2</sub> window open and p-metal deposition respectively. Brief descriptions of each step are listed as follows.

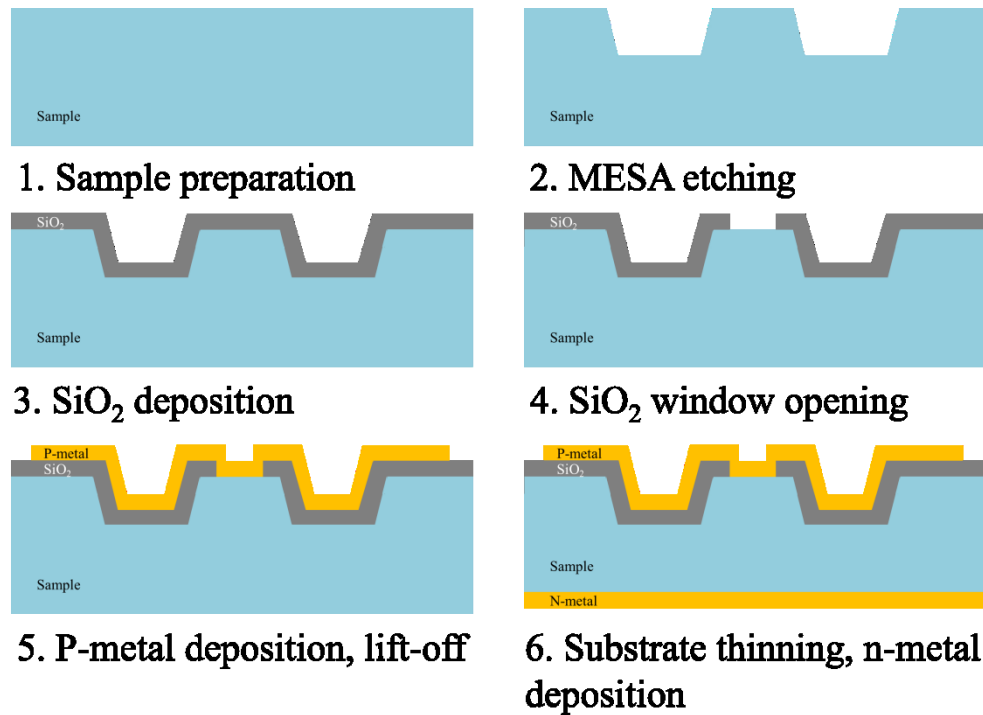


Fig. 6.2 Cross-sectional process flow diagram for edge emitters with oxide isolation.

**1) Sample preparation:** The samples are first cut into desired sizes and cleaned with Acetone, Methanol, and IPA rinse. After the cleaning, the wafer should immediately be dried gently with Nitrogen.

**2) MESA lithography:** In this step, spin-coater is utilized to apply AZ5214 resist onto the sample and the target thickness is  $\sim 2 \mu\text{m}$ . A profilometer is used to measure the thickness of the resist. Due to the irregular and small sizes of the samples, blue tape is used as adapter to assist the spin-coating. After the spin-coating, the sample is soft-baked at  $95 \text{ }^\circ\text{C}$  for 60 s. Photolithography is then used to define the patterns on MESA mask into photo-resist, followed by developing the sample in AZ300MIF developer for 60 s to transfer the patterns into the photo-resist. An optical microscope is used to inspect the defects on the sample surface. Next, the



sample is hard-baked at 110 °C for 3 mins, followed by an optional O<sub>2</sub> plasma descum to clean the resist residual in the area cleared by developer. A non-selective etchant of H<sub>2</sub>SO<sub>4</sub>:H<sub>2</sub>O<sub>2</sub>:H<sub>2</sub>O with the ratio of 1:8:40 is used to etch the MESA ridge. The etch rate is ~15 nm/min and should be finely calibrated before the device sample is etched. After the wet etching process, the resist is stripped using acetone, followed by the standard sample cleaning described in step 1).

**3) SiO<sub>2</sub> deposition:** PECVD is used to deposit a 500 nm SiO<sub>2</sub> layer at 250 °C onto the sample. The small size sample is attached to a five-inch dummy wafer with high-temperature tape, which is used as an adapter to accommodate the loading/unloading in PECVD with automatic mechanical arms. An extra small piece dummy silicon wafer should be attached to the adapter as well to serve as the thickness monitor wafer since the refractive index of Si substrate has already been added into the database of thickness measurement instrument but that of the III-V sample has not been. At last, the thickness of the SiO<sub>2</sub> layer is measured to compare with the nominal value 500 nm.

**4) SiO<sub>2</sub> window opening:** In order to increase the adherence between the photo-resist and the sample substrate, Hexamethyldisiloxane (HMDS) vapor prime is applied before the AZ5214 is coated, the target thickness of which is 2 μm. An image reverse lithography is used to define the pattern. The sample is exposed for 5 s with the SiO<sub>2</sub> window mask on in the mask aligner, then taken out and baked at 105 °C for 150 s, flood-exposed for 12.5 s in the mask aligner without mask, and developed in AZ300MIF for 60s. A BHF solution is used to etch the SiO<sub>2</sub> in the opened window, which contains 40% NH<sub>4</sub>OH and 49% HF with the ratio of 5:1. The solution is further diluted with DI water with 1:5 ratio to slow down the etch rate to make it process more controllable. The sample is then etched and rinsed with DI water in plastic beakers. The optimal etch time is about 90 s. At last, the resist is stripped using acetone, followed by the

standard sample cleaning process described in step 1). Fig. 6.3 shows the optical microscope images of the sample after the lithography and wet etching respectively.

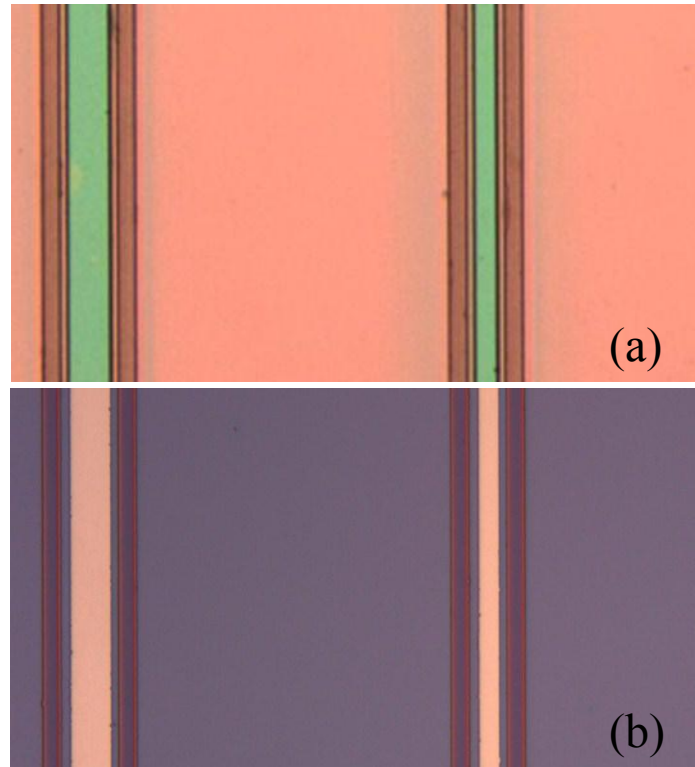


Fig. 6.3 Optical microscope images of the sample after the lithography (a) and wet etching process (b) respectively.

**5) P-metal deposition:** The image reserve lithography described in step 4) is used for the second time to make patterns in the photo-resist except that the mask used in this step is the p-metal mask. In an ebeam evaporator the sample is deposited with a 20 nm-thick Ti followed by a 300 nm-thick Au. Next, the sample is immersed in acetone to lift-off the metal pieces on top of the photo-resist. If necessary, the ultrasonic bath is used to accelerate the lift-off process. At last, the sample is cleaned using the cleaning process described in step 1) and blown dry using Nitrogen. Fig. 6.4 shows the optical microscope image of the sample after this step.

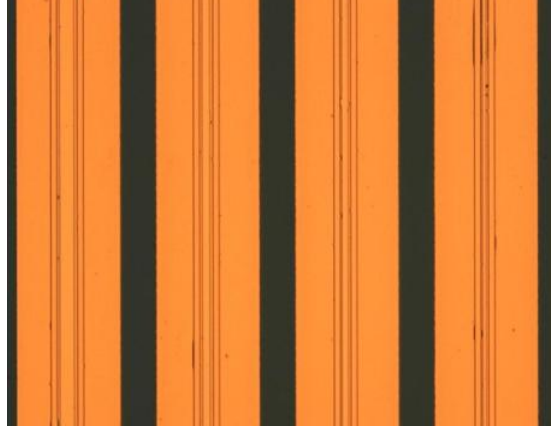


Fig. 6.4 Optical microscope image of the sample after the p-metal deposition.

**6) Substrate thinning:** Lapping process is used to thin the substrate on the backside from  $350\ \mu\text{m}$  to  $\sim 110\ \mu\text{m}$ . The sample is first covered with a spin-coated AZ5214 photo-resist thin layer to protect the front surface and mounted onto a warm 4-inch quartz plate ( $70\ ^\circ\text{C}$ , heated by hot plate) using white wax. After the quartz plate is cold, a blade is used to remove the excess white wax. The glass plate is mounted to the jig using vacuum and the jig is placed on the lapping plate. Slurry is made of  $3\ \mu\text{m}$ -diameter  $\text{Al}_2\text{O}_3$  powder and DI water with the ratio of 1:10 in volume, feeding to the lapping system at the speed of  $\sim 56$  drops/minute. Rotation speeds of the plate and the jig are set to 20 and 8 rpm respectively, which results in the lapping speed at  $15\ \mu\text{m}/\text{min}$ . A Starrlett thickness gauge is used to measure the thickness of the sample. After the desired thickness is achieved, the sample and the quartz plate is merged into the warm Optical Clear<sup>TM</sup> solvent ( $70\ ^\circ\text{C}$ , heated by hot plate) to dissolve the white wax to un-mount the sample. The un-mounted sample is rinsed thoroughly using the Optical Clear<sup>TM</sup> solvent, followed by the resist strip and standard clean procedure described in step 1). However, special cares should be taken since the sample is very thin and fragile at this point and even a strong nitrogen blow would tear the sample apart.

7) *n-metal deposition*: In this step, an AuGe/Ni/Au stack (75 nm/50 nm/300 nm) is deposited on the backside of the sample using ebeam evaporation. A profilometer is used to measure the thickness of the stack after the deposition.

8) *RTA*: AGA Heat Pulse 610 is used to perform the RTA to the samples. Based on the calibration results on p type and n type GaAs using transmission line method (TLM), we conclude the optimal condition to anneal is at 410 °C for 30 s for GaAs-based devices. Nitrogen is kept on all the time during the annealing process.

After step 8), the sample is ready to be cleaved to form Fabry-Perot cavity. A cleaving station is designed to cleave the sample precisely and a probe station is designed to measure the characterization of devices. Fig 6.5 shows the optical microscope image of the cleaved sample on the probe station.

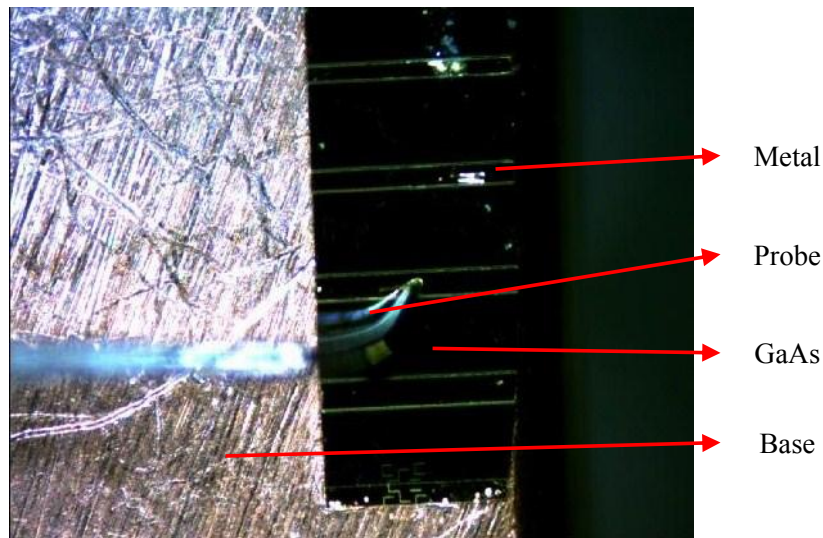


Fig. 6.5 Optical microscope image of the cleaved sample on the probe station.

## 6.3 Mask design

### 6.3.1 Design of device patterns

In our experiments, photomasks have been designed for different types of optoelectronic devices, such as edge emitters and photo-detectors. In the design of edge emitting laser diodes, five different MESA widths are used, 8  $\mu\text{m}$ , 10  $\mu\text{m}$ , 12  $\mu\text{m}$ , 16  $\mu\text{m}$ , 20  $\mu\text{m}$ , and 30  $\mu\text{m}$ . Fig. 6.6 (a), (b) and (c) show the mask designs for edge emitting laser diodes with MESA width of 20  $\mu\text{m}$ . The three layers are used for the three lithography processes in the process flow. Fig. 6.6 (d) and (e) display the mask stack image and the wafer image, which indicates the well agreement between the design target and the real fabricated device.

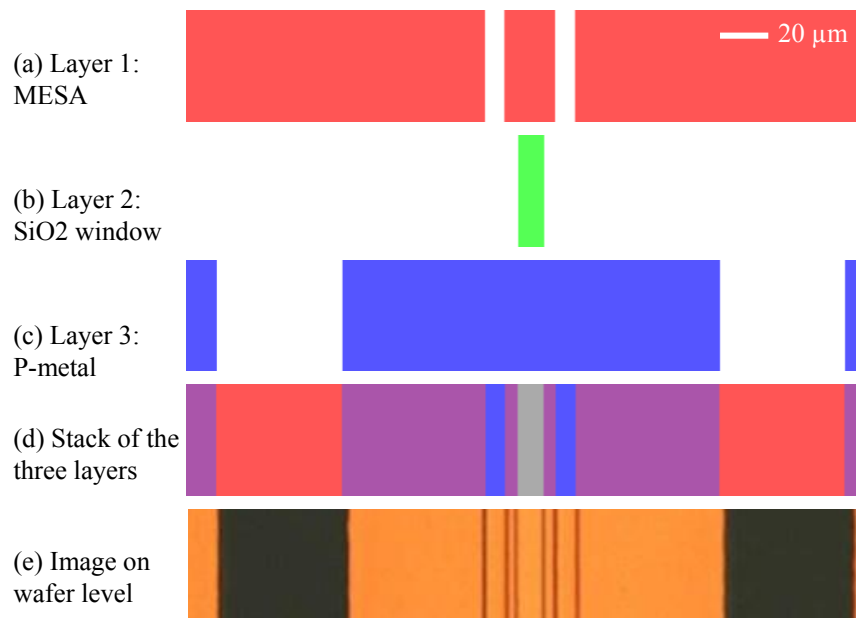


Fig. 6.6 Mask designs for edge emitting laser diodes (a-d) and the corresponding image on wafer level (e).

Fig. 6.7 shows the pattern designs of photo-detectors with different sizes. The MESA layer is in red and the metal layer is in blue. The lower right corner is filled with metal to facility the wire bonding process in packaging.

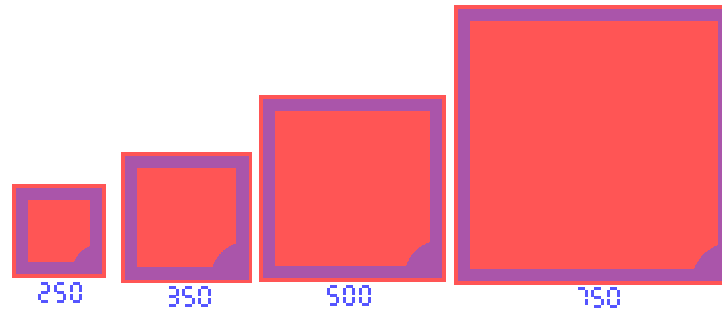


Fig. 6.7 Mask of photo-detectors with different sizes. The MESA layer is in red and the metal layer is in blue.

### 6.3.2. Design of auxiliary functionalities

Although the critical role of the device mask designs is highly appreciated, the importance of the auxiliary pattern designs is usually underestimated. For example, it is not uncommon that the device patterns occupy the most area on the mask and little space is reserved for overlay, process monitoring and characterization. In this work, we design one set of standard auxiliary patterns for those underrated functionalities and implement them into the device processing works to improve the capability and reliability of the process.

Fig. 6.8(a) shows a vernier scale that is used as a fine alignment mark to improve the overlay accuracy between different layers. In the layout, the red (middle), green (lower) and blue (upper) colors represent the first, second, and third layers respectively. The bars are 20  $\mu\text{m}$  in width, spaced to each other by 31  $\mu\text{m}$  in the first layer and 30  $\mu\text{m}$  in other two layers. The center bars in the three layers are designed to be coincident in horizontal direction, as highlighted in the

circles in Fig. 6.8(a). If the layers are perfectly aligned in the processing, the relative position of the three layers will be the same as designed. On the other hand, if the second or the third layer is misaligned to the first layer, the center bars of the two layers will not match with the center bar of the first layer and the bars in other position may match with the corresponding bar in the first layer depending on the offset of the misalignment. For example, Fig. 6.8(b) shows the third layer is shifted to left by  $3\ \mu\text{m}$  hence their third bars match with each other perfectly. This vernier scale not only can be used to characterize the overlay quantitatively in an in-situ manner but also can be used to minimize the alignment error. In this design, it is capable to achieve the overlay accuracy within  $1\ \mu\text{m}$ . Fig. 6.9 displays an optical microscope image of the vernier scale in a laser diode processing, in which the center bars of the two layers are well aligned and the overlay error is within  $1\ \mu\text{m}$ .

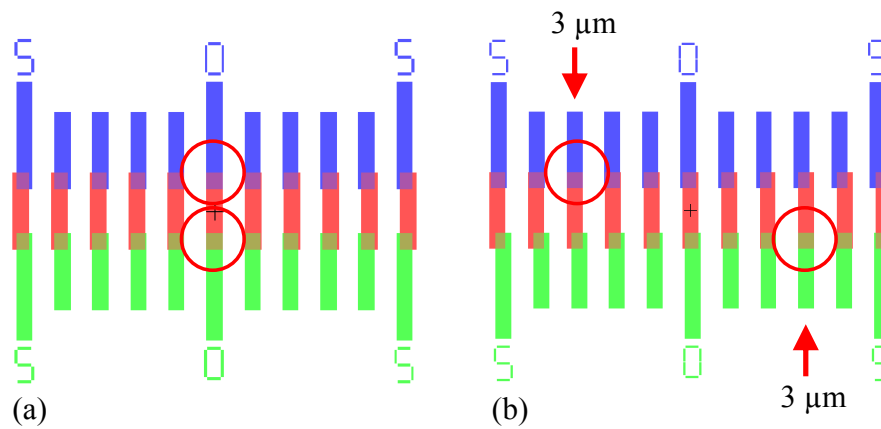


Fig. 6.8 Schematic diagrams of vernier scale alignment marks. (a) Perfectly aligned; (b) misaligned by  $3\ \mu\text{m}$ .

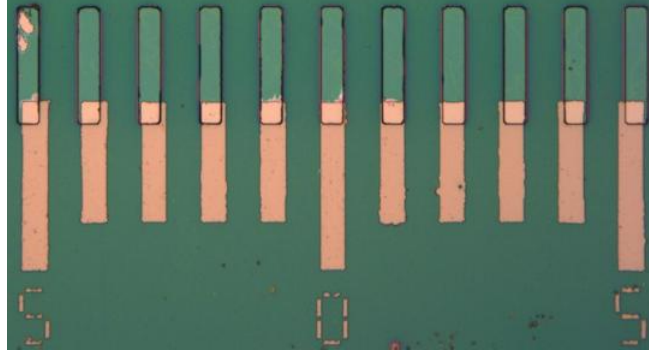


Fig. 6.9 An optical microscope image of the vernier scale in the processing of laser diodes. The center bars of the two layers are well aligned and the overlay error is within 1 μm.

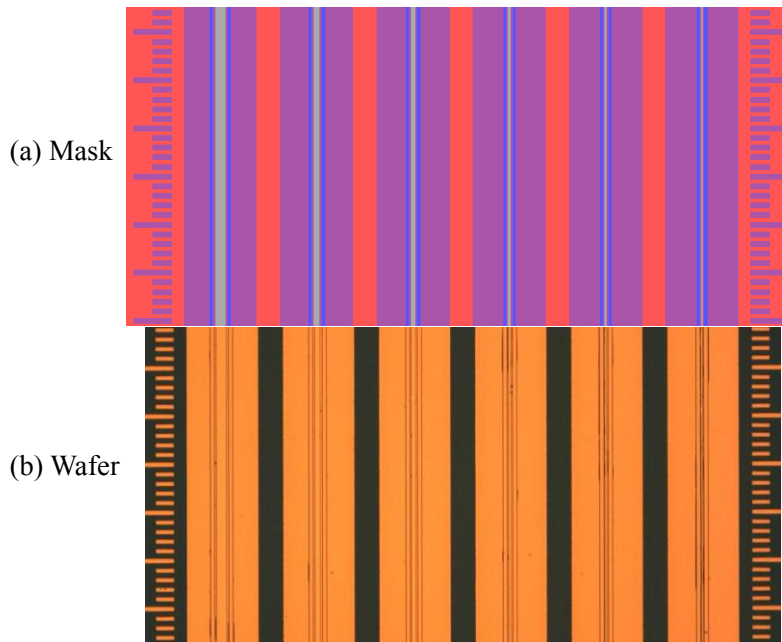


Fig. 6.10 Metal scales in mask design (a) and on wafer surface (b). The major ticks are placed every 100 μm and four minor ticks are placed between the major ticks.

In laser diode characterization, the cavity length needs to be determined precisely since the threshold current of laser diodes closely depends on the length of the Fabry-Perot cavity. It will



even be very helpful if the cavity length of the device can be predicated and controlled during the sample cleaving. We incorporate scales into the mask design so that the length of cavity can be in-situ monitored during the cleaving process. Fig. 6.10 shows the scales on mask and wafer levels, which have 10  $\mu\text{m}$  in width. The major ticks are 80  $\mu\text{m}$  in length and placed every 100  $\mu\text{m}$ . Four minor ticks are 40  $\mu\text{m}$  in length and placed between the major ticks. In sample cleaving process, the scales can be viewed clearly under microscope therefore the devices can be cut with desired cavity lengths. The length error can be controlled within 5  $\mu\text{m}$ , which is only 0.5% error for a 1 mm cavity.

#### 6.4 Device demonstration

Different types of optoelectronic devices, such as GaAs QW laser diodes, InGaAs QW laser diodes and InAs QD LEDs have been successfully fabricated using the developed processes. Fig. 6.11 displays the cross-sectional SEM image of a GaAs QW laser diode using the process flow described in Fig. 6.2.

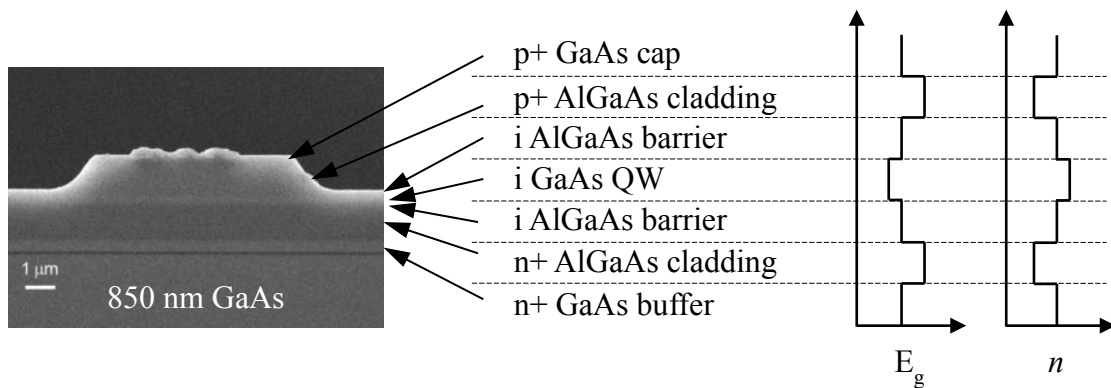


Fig. 6.11 Cross-sectional SEM image of a GaAs QW laser diode.

Continuous-wave room-temperature operation of this device has been achieved, as shown in the I-L curve in Fig. 6.12. The cavity length of the device is  $\sim 1$  mm and the width of the MESA

is about 8  $\mu\text{m}$ , which yields a threshold current of  $\sim 250 \text{ A/cm}^2$ . The low threshold and high output power of the laser device indicate the high performance of the device and the excellent quality of the process. The device-proven process demonstrates the capability and readiness to make high performance optoelectronic devices using III-V bismide materials.

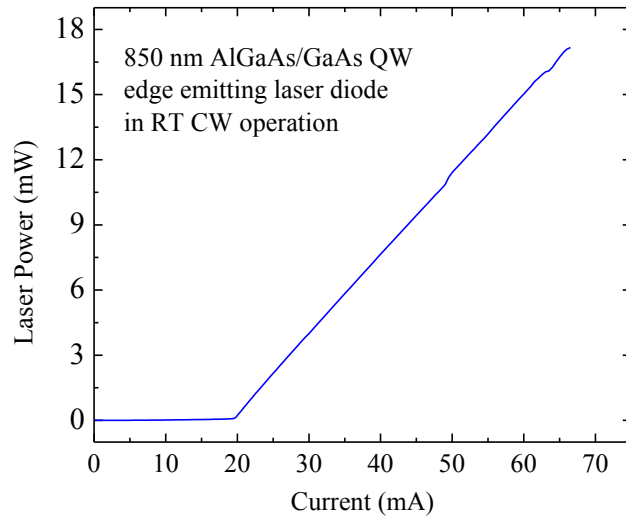


Fig 6.12 I-L curve of a RT CW operational GaAs QW laser diode.

In addition, the performance of the devices is an indicator of material quality and the devices can be used to evaluate new growth techniques. For example, we develop an *in-situ* patterning technique by using Ga droplets to drill nano-holes on the GaAs substrates in MBE chamber. Compared with the conventional *ex-situ* patterning technique, this *in-situ* technique avoids the sample being taken out from the MBE chamber and thus eliminates the contamination associated with the wet bench processing. It is of importance to know if the material still has good optical properties after the treatment. Hence, we grow InAs QDs on the nano-hole drilled substrate, fabricate LEDs using the process and characterize the devices. The room temperature operational performance indicates good optical quality of the material, as shown in Fig. 6.13,

which suggests that the *in-situ* patterning technique provides a high material quality solution to pattern substrate effectively and is worthy to be further investigated.

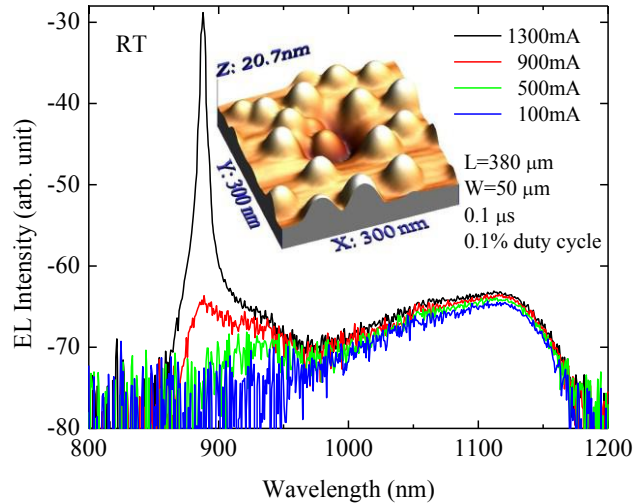


Fig. 6.13 RT spectra of an InAs QD LED. The inset shows the AFM image of InAs QDs grown on nano-holes patterned GaAs substrate.

## 6.5 Summary

In summary, process flows for optoelectronic devices have been developed and the related photomasks have been designed. Photolithography, wet etching, PECVD, ebeam evaporation, lift-off, lapping and RTA have been optimized and integrated into the process flows. 2 μm resolution and 1 μm overlay have been achieved for the processes. The capability, flexibility and reliability of the process flows have been demonstrated by the high performance GaAs-based optoelectronic devices fabricated using these flows. The device-proven processes bridge the material research with the device development and enable the future device fabrication using III-V bismide materials.



## 7 CONCLUSION AND FUTURE WORK

### 7.1 Conclusion

Firstly, we have thoroughly studied the technologies used in the RT CW operational GaSb-based type-I InGaAsSb/AlGaInAsSb QW laser diodes and discussed the limitations of current solutions – lack of hole confinement, difficulty in extending the wavelength and potential reliability issues. To address these difficulties, we have proposed novel GaSb-based GaInAsSbBi alloys to replace traditional InGaAsSb alloys to be used in QW regions of the laser diodes to achieve the optical transition wavelength up to 4  $\mu\text{m}$ . This novel III-V bismide alloys deliver excellent flexibility in tuning the optical transition wavelength and the band alignment, meanwhile greatly enhanced hole confinement ( $> 100$  meV than traditional designs). Moreover, quasi-Al-free laser structures have been achieved by using GaInAsSbBi/GaSb active regions and InGaAsSb cladding layers, which significantly improve the reliability of the laser devices. Compared with the currently used InGaAsSb/AlInGaAsSb approach, our approach provides enhanced hole confinement, extended wavelength, eased growth complexity and elevated reliability. These outstanding advantages make the GaInAsSbBi alloys the best candidates for the RT CW operational laser diodes operating in 3-4  $\mu\text{m}$ . In addition, we have proposed the GaInAsSbBi alloys to be used in high efficiency multi-junction thermophotovoltaic devices. Compared with traditionally used InGaAsSb alloys, GaInAsSbBi alloys provide much narrower bandgaps (below 0.5 eV), which result in broader spectrum coverage and considerably improved efficiency.

Secondly, we have systematically investigated the effects of the Bi flux and the growth temperature on the morphological and optical properties of the GaAs-based GaAsBi material in the MBE growth. The Bi composition can be tuned in a wide range by varying the Bi flux and

the growth temperature. The optimal growth condition can be achieved by balancing the effect of Bi as the surfactant to promote the optical quality and the accumulation of Bi as droplets to deteriorate the optical quality. The samples grown under the optimal growth conditions not only show excellent structural properties in the HRXRD, TEM and EDS measurement, but also feature excellent optical properties by exhibiting strong RT PL. The deeply understanding of Bi's dual mechanisms in low temperature GaAsBi/GaAs material growth and the successful growth of high quality GaAsBi/GaAs QW samples open up new possibilities for the further development of quantum nanostructure using this material system towards high performance RT operational optoelectronic devices.

Thirdly, we have proposed the Bi surfactant mediated growth of AlGaAs barrier layers at low temperatures to address the bottleneck of the current GaAs-based GaAsBi optoelectronic devices – lack of high quality SCHs – to improve the performance of the devices. We have demonstrated for the first time the high quality GaAsBi/GaAs/AlGaAs SQW SCHs and DQW SCHs using MBE growth with the top AlGaAs barrier layers grown at the unconventional low temperature 320 °C. The surfactant effect of Bi is evidenced by the presence of a  $(1 \times 3)$  surface reconstruction throughout the growth of the growth of AlGaAs layers at the low temperature. Both the SQW and DQW SCHs show good structural properties in cross-sectional TEM measurement as well as good optical properties as exhibiting strong RT PL. The proposed approach to grow DQW SCH can be extended to growing laser diode structures with MQW SCHs containing more identical QWs. The growth of the high quality SQW and DQW SCH successfully integrates SCH and MQW designs into GaAsBi/GaAs material system and enables the growth of optimized device structures towards high performance temperature insensitive optoelectronic devices.

Fourthly, process flows and photomasks have been developed for the fabrication of the optoelectronic devices such as laser diodes, light emitting diodes, and photo-detectors. High performance GaAs QW laser diodes and InAs QD LEDs have been demonstrated using our designed process flows. The device-proven processes not only build the infrastructures for the fabrication of III-V bismide devices, but also bridge the material research with the device design and device development.

## **7.2 Future work**

### **7.2.1 GaAsBi optoelectronic devices**

With the high quality GaAsBi SCHs developed, the performance of the GaAs-based GaAsBi optoelectronic devices is expected to be considerably improved. The laser diodes also become possible to be realized implementing the SCH designs into the device structures. GaAs-based GaAsBi laser diodes, LEDs and photodetectors with the SCH designs therefore can be grown and fabricated using the established methodologies. The high performance bismide optoelectronic devices not only facilitate the device applications for telecommunication, sensing and imaging, but also accelerate the development of the III-V bismide material.

### **7.2.2 Bi surfactant mediated growth for III-V-Si integration**

In the development of GaAsBi SCHs, Bi surfactant mediated growth is used to grow the high quality AlGaAs at low temperatures. This low temperature growth technique is of great interest for the applications of III-V-Si integration, optical interconnects and optical computing. The III-V-Si integration has been desired for many years to integrate the high density silicon electronics with the high performance optoelectronics without malfunction and performance degradation. Among the different approaches, the most efficient way to integrate the two

material systems is to grow III-V material on Si wafers after the Si circuitry is made on the Si substrates. However, if the III-V material is grown at the conventional high temperature (GaAs: 580 °C, AlGaAs: 610 °C), the Si circuitry will malfunction due to a variety of side effects, for example the unexpected diffusion of the dopants in the p-n junctions. Through the Bi surfactant mediated growth, the III-V material can be grown at ~300 °C with excellent properties, which effectively eliminates the side-effects brought by the traditional high temperature growth.

To demonstrate the performance of this novel technique, standard optoelectronic devices, such as GaAs QW laser diodes, can be grown on GaAs substrates at low temperatures. The specifications of the GaAs laser diodes grown at low temperatures then can be compared with the devices grown at traditional high temperatures. The same device design can be implemented on the Si substrates to further investigate the integration of III-V and Si material systems. This new growth technique opens new route for III-V-Si integration and helps to propel the future development in optical interconnects and optical computing.



## BIBLIOGRAPHY

- [1] S. L. Chuang, "Physics of Photonic devices", 2<sup>nd</sup> edition, *Wiley, New York*, 2009.
- [2] I. Vurgaftman, J. R. Meyer and L. R. Ram-Mohan, "Band parameters for III-V compound semiconductors and their alloys", *J. Appl. Phys.*, vol. 89, no. 11, pp. 5815, 2001.
- [3] A. Janotti, S.-H. Wei and S. B. Zhang, "Theoretical study of the effects of isovalent coalloying of Bi and N in GaAs", *Phys. Rev. B*, vol. 65, pp. 115203, 2002.
- [4] S. Nakamura, T. Mukai and M. Senoh, "High-Power GaN P-N junction blue-light-emitting diodes", *Jpn. J. Appl. Phys.*, vol. 30, pp. L1998, 1991.
- [5] R.J. Mears, L. Reekie, S. B. Poole, D. N. Payne, "Low-threshold tunable CW and Q-switched fibre laser operating at 1.55  $\mu\text{m}$ ", *Electronics Letters*, vol. 22, no. 3, pp. 159, 1986.
- [6] V. M. Ustinov, *et al.*, "InAs/InGaAs quantum dot structures on GaAs substrates emitting at 1.3  $\mu\text{m}$ ", *Appl. Phys. Lett.*, vol. 73, no. 19, pp. 2815, 1999.
- [7] R. Jäger, M. Grabherr, C. Jung, R. Michalzik, G. Reiner, B. Weigl and K. J. Ebeling, "57 % wallplug efficiency oxide-confined 850nm wavelength GaAs VCSELs", *Electronics Letters*, vol. 33, no. 4, pp. 330, 1997.
- [8] B. Joukoff and A.M. Jean-Louis, "Growth of  $\text{InSb}_{1-x}\text{Bi}_x$  single crystals by Czochralski method", *J. Cryst. Growth*, vol. 12, no. 2, pp. 169, 1972.
- [9] K. Oe, S. Ando and K. Sugiyama, " $\text{InSb}_{1-x}\text{Bi}_x$  films grown by molecular beam epitaxy", *Jpn. J. Appl. Phys.*, vol. 20, no. 4, pp. L303, 1981.
- [10] A. J. Noreika, W. J. Takei, M. H. Francombe, and C. E. C. Wood, "Indium antimonide bismuth compositions grown by molecular beam epitaxy", *Appl. Phys. Lett.*, vol. 53, no. 7, pp. 4932, 1982.
- [11] T. P. Humphreys, P. K. Chiang, S. M. Bedair, and N. R. Parikh, "Metalorganic chemical vapor deposition and characterization of the InAsSbBi material system for infrared detection", *Appl. Phys. Lett.*, vol. 53, no. 2, pp. 142, 1988.
- [12] Z. M. Fang, K. Y. Ma, R. M. Cohen and G. B. Stringfellow, "Photoluminescence of InAsBi and InAsSbBi grown by organometallic vapor phase epitaxy", *J. Appl. Phys.*, vol. 66, no. 3, pp. 1187, 1990.
- [13] K. Y. Ma, Z. M. Fang, R. M. Cohen, and G. B. Stringfellow, "Organometallic vaporphase epitaxy growth and characterization of Bi containing III/V alloys", *J. Appl. Phys.*, vol. 68, no. 9, pp. 4586, 1990.
- [14] K. T. Huang, C. T. Chiu, R. M. Cohen, and G. B. Stringfellow, "InAsSbBi alloys grown by organometallic vapor-phase epitaxy", *J. Appl. Phys.*, vol. 75, no. 6, pp. 2857, 1994.

- [15] J. J. Lee, J. D. Kim, and M. Razeghi, "Growth and characterization of InSbBi for long wavelength infrared photodetectors", *Appl. Phys. Lett.*, vol. 70, no. 24, pp. 3266, 1997.
- [16] Q. Du, J. Alperin and W. I. Wang, "Molecular beam epitaxial growth of GaInSbBi for infrared detector applications", *J. Cryst. Growth*, vol. 175, pp. 849, 1997.
- [17] K. Oe and H. Okamoto, "New Semiconductor Alloy GaAs<sub>1-x</sub>Bi<sub>x</sub> Grown by Metal Organic Vapor Phase Epitaxy", *Jpn. J. Appl. Phys.*, vol. 37, pp. L1283, 1998.
- [18] S. Tixier, M. Adamcyk, T. Tiedje, S. Francoeur, A. Mascarenhas, P. Wei, and F. Schiettekatte, "Molecular beam epitaxy growth of GaAs<sub>1-x</sub>Bi<sub>x</sub>", *Appl. Phys. Lett.*, vol. 82, pp. 2245, 2003.
- [19] K. Oe, "Metalorganic vapor phase epitaxial growth of metastable GaAs<sub>1-x</sub>Bi<sub>x</sub> alloy", *J. Cryst. Growth*, vol. 237-239, pp. 1481, 2002.
- [20] M. Yoshimoto, S. Murata, A. Chayahara, Y. Horino, J. Saraie and K. Oe, "Metastable GaAsBi alloy grown by molecular beam epitaxy", *Jpn. J. Appl. Phys.*, vol. 42, no. 10B, pp. L1235, 2003.
- [21] S. Francoeur, M.-J. Seong and A. Mascarenhas, S. Tixier, M. Adamcyk and t. Tiedje, "Band gap of GaAs<sub>1-x</sub>Bi<sub>x</sub>, 0<x<3.6%", *Appl. Phys. Lett.*, vol. 82, no. 22, pp. 3874, 2003.
- [22] M. Henini, J. Ibáñez, M. Schmidbauer, M. Shafi, S. V. Novikov, L. Turyanska, S. I. Molina, D. L. Sales, M. F. Chisholm, and J. Misiewicz, "Molecular beam epitaxy of GaBiAs on (3 1 1)B GaAs substrates", *Appl. Phys. Lett.*, vol. 91, pp. 251909, 2007.
- [23] E. C. Young, M. B. Whitwick, T. Tiedje, D. A. Beaton, "Bismuth incorporation in GaAs<sub>1-x</sub>Bi<sub>x</sub> grown by molecular beam epitaxy with in-situ light scattering", *phys.stat. sol. (c)*, vol. 4, no. 5, pp. 1707, 2007.
- [24] X. Lu, D. A. Beaton, R. B. Lewis, T. Tiedje and M. B. Whitwick, "Effect of molecular beam epitaxy growth conditions on the Bi content of GaAs<sub>1-x</sub>Bi<sub>x</sub>", *Appl. Phys. Lett.*, vol. 92, pp. 192110, 2008.
- [25] V. Pačebutas, K. Bertulis, G. Aleksejenko and A. Krotkus, "Molecular-beam-epitaxy grown GaBiAs for terahertz optoelectronic applications", *J. Mater. Sci: Mater. Eletron.*, Vol. 20, pp. 363, 2009.
- [26] X. Lu, D. A. Beaton, R. B. Lewis, T. Tiedje and Y. Zhang, "Composition dependence of photoluminescence of GaAs<sub>1-x</sub>Bi<sub>x</sub> alloys", *Appl. Phys. Lett.*, vol. 95, pp. 041903, 2009.
- [27] Z. Chine, H. Fitouri, I. Zaied, A. Rebey and B. El Jani, "Growth of GaAsBi alloy under alternated bismuth flows by metalorganic vapor phase epitaxy", *J. Cryst. Growth*, vol. 330, pp. 35, 2011.

- [28] F. Bastiman, A. R. B. Mohmad, J. S. Ng, J. P. R. David and S. J. Sweeney, “Non-stoichiometric GaAsBi/GaAs (1 0 0) molecular beam epitaxy growth”, *J. Cryst. Growth*, vol. 338, pp. 57, 2012.
- [29] A. J. Ptak, R. France, D. A. Beaton, K. Alberi, J. Simon, A. Mascarenhas, C.-S. Jiang, “Kinetically limited growth of GaAsBi by molecular-beam epitaxy”, *J. Cryst. Growth*, vol. 338, pp. 107, 2012.
- [30] M. Yoshimoto, W. Huang, Y. Takehara, J. Saraie, A. Chayahara, Y. Horino, K. Oe, “New semiconductor GaNAsBi alloy grown by molecular beam epitaxy”, *Jpn. J. Appl. Phys.*, vol. 43, no. 7A, pp. L845, 2004.
- [31] W. Huang, M. Yoshimoto, Y. Takehara, J. Saraie and K. Oe, “GaN<sub>y</sub>As<sub>1-x-y</sub>Bi<sub>x</sub> alloy lattice matched to GaAs with 1.3 μm photoluminescence emission”, *Jpn. J. Appl. Phys.*, vol. 43, no. 10B, pp. L1350, 2004.
- [32] D. A. Beaton, A. J. Ptak, K. Alberi and A. Mascarenhas, “Quaternary bismide alloy B<sub>y</sub>Ga<sub>1-y</sub>As<sub>1-x</sub>Bi<sub>x</sub> lattice matched to GaAs”, *J. Cryst. Growth*, vol. 351, pp. 37, 2012.
- [33] G. Feng, K. Oe and M. Yoshimoto, “Bismuth containing III-V quaternary alloy InGaAsBi grown by MBE”, *phys. stat. sol. (a)*, vol. 203, no.11, pp. 2670, 2006.
- [34] J. P. Petropoulos, Y. Zhong, and J. M. O. Zide, “Optical and electrical characterization of InGaBiAs for use as a mid-infrared optoelectronic material”, *Appl. Phys. Lett.*, vol. 99, pp. 031110, 2011.
- [35] Y. Zhong, P. B. Dongmo, J. P. Petropoulos, and J. M. O. Zide, “Effects of molecular beam epitaxy growth conditions on composition and optical properties of In<sub>x</sub>Ga<sub>1-x</sub>Bi<sub>y</sub>As<sub>1-y</sub>”, *Appl. Phys. Lett.*, vol. 100, pp. 112110, 2012.
- [36] S. K. Das, T. D. Das, S. Dhar, M. de la Mare, A. Krier, “Near infrared photoluminescence observed in dilute GaSbBi alloys grown by liquid phase epitaxy”, *Infrared Physics & Technology*, vol. 55, pp. 156, 2012.
- [37] N. J. H. Graf, “MBE of mixed systems Ga(Sb,Bi) and In(Sb,Bi)”, *Ph.D. dissertation*, 2008.
- [38] Y. Song, S. Wang, I. S. Roy, P. Shi, and A. Hallen, “Growth of GaSb<sub>1-x</sub>Bi<sub>x</sub> by molecular beam epitaxy”, *J. Vac. Sci. Technol. B*, vol. 30 no. 2, pp. 02B114, 2012.
- [39] B. M. Sinel’nikov and M. L. Lunina, “Ga<sub>x</sub>In<sub>1-x</sub>Bi<sub>y</sub>As<sub>z</sub>Sb<sub>1-y-z</sub>/InSb and InBi<sub>y</sub>As<sub>z</sub>Sb<sub>1-y-z</sub>/InSb heterostructures grown in a temperature gradient”, *Inorganic Materials*, vol. 48, no. 9, pp. 877, 2012.
- [40] L.S. Rothman *et al.*, “The HITRAN 2008 molecular spectroscopic database”, *Journal of Quantitative Spectroscopy & Radiative Transfer*, vol. 110, pp. 533, 2009.

- [41] A. Vicet, D. A. Yarekha, A. Pérona, Y. Rouillard, S. Gaillard, A. N. Baranov, “Trace gas detection with antimonide-based quantum-well diode lasers”, *Spectrochimica Acta Part A*, vol. 58, no. 11, pp. 2405, 2002.
- [42] L. Shterengas, G. Belenky, G. Kipshidze and T. Hosoda, “Room temperature operated 3.1  $\mu\text{m}$  type-I GaSb-based diode lasers with 80 mW continuous-wave output power”, *Appl. Phys. Lett.*, vol. 92, pp. 171111, 2008.
- [43] K. Vizbaras, A. Vizbaras, A. Andrejew, C. Grasse, S. Sprengel and M.-C. Amann, “Room-temperature type-I GaSb-based lasers in the 3.0-3.7  $\mu\text{m}$  wavelength range”, *Proc. SPIE 8277, Novel In-plane Semiconductor Lasers XI*, pp. 82771B, 2012.
- [44] A. D. Andreev and D. V. Donetsky, “Analysis of temperature dependence of the threshold current in 2.3–2.6  $\mu\text{m}$  InGaAsSb/AlGaAsSb quantum-well lasers”, *Appl. Phys. Lett.*, vol. 74, no. 19, pp. 2743, 1999.
- [45] L. Shterengas, G. L. Belenky, J. G. Kim and R. U. Martinelli, “Design of high-power room-temperature continuous-wave GaSb-based type-I quantum-well lasers with  $\lambda > 2.5 \mu\text{m}$ ”, *Semicond. Sci. Technol.*, vol. 19, pp. 655, 2004.
- [46] A. Salhi, Y. Rouillard, J. Angellier, P. Grech and A. Vicet, “2.61  $\mu\text{m}$  GaInAsSb/AlGaAsSb type I quantum well laser diodes with low threshold”, *Electronics Letters*, vol. 40, no. 7, pp. 424, 2004.
- [47] G. L. Belenky, J. G. Kim, L. Shterengas, A. Gourevitch and R. U. Martinelli, “High-power 2.3  $\mu\text{m}$  laser arrays emitting 10W CW at room temperature”, *Electronics Letters*, vol. 40, no. 12, pp. 737, 2004.
- [48] J. A. Gupta, P. J. Barrios, J. Lapointe, G. C. Aers, and C. Storey, “Single-mode 2.4  $\mu\text{m}$  InGaAsSb/AlGaAsSb distributed feedback lasers for gas sensing”, *Appl. Phys. Lett.*, vol. 95, pp. 041104, 2009.
- [49] K. Kashani-Shirazi, K. Vizbaras, A. Bachmann, S. Arafin and M.-C. Amann, “Low-Threshold Strained Quantum-Well GaSb-Based Lasers Emitting in the 2.5- to 2.7-  $\mu\text{m}$  Wavelength Range”, *IEEE Photonics Technology Letters*, vol. 21, no. 16, pp. 1106, 2009.
- [50] C. Lin, M. Grau, O. Dier and M.-C. Amann, “Low threshold room-temperature continuous-wave operation of 2.24-3.04  $\mu\text{m}$  GaInAsSb/AlGaAsSb quantum-well lasers”, *Appl. Phys. Lett.*, vol. 84, no. 25, pp. 5088, 2004.
- [51] M. Grau, C. Lin, O. Dier, C. Lauer and M.-C. Amann, “Room-temperature operation of 3.26  $\mu\text{m}$  GaSb-based type-I lasers with quaternary AlGaInAsSb barriers”, *Appl. Phys. Lett.*, vol. 87, pp. 241104, 2004.
- [52] T. Hosoda, G. Belenky, L. Shterengas, G. Kipshidze and M. V. Kisin, “Continuous-wave room temperature operated 3.0  $\mu\text{m}$  type I GaSb-based lasers with quaternary AlInGaAsSb barriers”, *Appl. Phys. Lett.*, vol. 92, pp. 091106, 2008.

- [53] T. Lehnhardt, M. Hümmer, K. Röbner, M. Müller, S. Höfling and A. Forchel, “Continuous wave single mode operation of GaInAsSb/GaSb quantum well lasers emitting beyond 3  $\mu\text{m}$ ”, *Appl. Phys. Lett.*, vol. 92, pp. 183508, 2008.
- [54] L. Shterengas, G. Belenky, T. Hosoda, G. Kipshidze and S. Suchalkin, “Continuous wave operation of diode lasers at 3.36  $\mu\text{m}$  at 12  $^{\circ}\text{C}$ ”, *Appl. Phys. Lett.*, vol. 93, pp. 011103, 2008.
- [55] T. Hosoda, G. Kipshidze, L. Shterengas, S. Suchalkin and G. Belenky, “200mW type I GaSB-based laser diodes operating at 3  $\mu\text{m}$ : Role of waveguide width”, *Appl. Phys. Lett.*, vol. 94, pp. 261104, 2009.
- [56] J. A. Gupta, P. J. Barrios, G. C. Aers, P. Waldron and C. Storey, “Room-temperature continuous-wave operation of type-I GaSb-based lasers at 3.1  $\mu\text{m}$ ”, *Electronics Letters*, vol. 45, no. 16, pp. 835, 2009.
- [57] T. Hosoda, G. Kipshidze, G. Tsvid, L. Shterengas and G. Belenky, “Type-I GaSb-based laser diodes operating in 3.1- to 3.3- $\mu\text{m}$  wavelength range”, *IEEE Photonics Technology Letters*, vol. 22, no. 10, pp. 718, 2010.
- [58] T. Hosoda, G. Kipshidze, L. Shterengas and G. Belenky, “Diode lasers emitting near 3.44  $\mu\text{m}$  in continuous-wave regime at 300K”, *Electronics Letters*, vol. 46, no. 21, pp. 1455, 2011.
- [59] K. Vizbaras, M.-C. Amann, “3.6  $\mu\text{m}$  GaSb-based type-I lasers with quaternary barriers, operating at room temperature”, *Electronics Letters*, vol. 47, no. 17, pp. 980, 2011.
- [60] G.B. Stringfellow, “Miscibility gaps in quaternary III/V alloys”, *J. Cryst. Growth*, vol. 58, no.1, pp. 194, 1982.
- [61] O. Dier, S. Dachs, M. Grau, C. Lin, C. Lauer and M.-C. Amann, “Effects of thermal annealing on the band gap of GaInAsSb”, *Appl. Phys. Lett.*, vol. 86, pp. 151120, 2005.
- [62] K. O’Brien, S. J. Sweeney, A. R. Adams, S. R. Jin, C. N. Ahmad, B. N. Murdin, A. Salhi, Y. Rouillard and A. Joullié, “Carrier recombination mechanisms in mid-infrared GaInAsSb quantum well lasers”, *phys. status solidi (c)*, vol. 244, no. 1, pp. 203, 2007.
- [63] Y. Horikoshi and Y. Furukawa, “Temperature sensitive threshold current of InGaAsP-InP double heterostructure lasers”, *Jpn. J. Appl. Phys.*, vol. 18, no. 4, pp. 809, 1979.
- [64] N. K. Dutta and R. J. Nelson, “Temperature dependence of threshold of InGaAsP/InP double heterostructure lasers and Auger recombination”, *Appl. Phys. Lett.*, vol. 38, no. 6, pp. 407, 1981.
- [65] S. J. Sweeney, “Light emitting semiconductor device”, WO patent 2010/149978, 2010.
- [66] A. Sugimura, “Comparison of Band-to-band Auger process in InGaAsP”, *IEEE J. Quantum Electron.*, vol. QE-19, no. 6, pp. 930, 1983.

- [67] M. Ferhat and A. Zaoui, “Structural and electronic properties of III-V bismuth compounds”, *Phys. Rev. B*, vol. 73, pp. 115107, 2006.
- [68] K. Alberi, J. Wu, W. Walukiewicz, K. M. Yu, O. D. Dubon, S. P. Watkins, C. X. Wang, X. Liu, Y.-J. Cho, and J. Furdyna, “Valence-band anticrossing in mismatched III-V semiconductor alloys”, *Phys. Rev. B*, vol. 75, pp. 045203, 2007.
- [69] K. Alberi, O. D. Dubon, W. Walukiewicz, K. M. Yu, K. Bertulis, and A. Krotkus, “Valence band anticrossing in  $\text{GaBi}_x\text{As}_{1-x}$ ”, *Appl. Phys. Lett.*, vol. 91, pp. 051909, 2007.
- [70] A. Mascarenhas, R. Kini, Y. Zhang, R. France and A. Ptak, “Comparison of the dilute bismide and nitride alloys  $\text{GaAsBi}$  and  $\text{GaAsN}$ ”, *phys. stat. sol. (b)*, vol. 246, no. 3, pp. 504, 2009.
- [71] Y. Zhang, A. Mascarenhas and L.-W. Wang, “Similar and dissimilar aspects of III-V semiconductors containing Bi versus N”, *Phys. Rev. B*, vol. 71, pp. 155201, 2005.
- [72] B. Fluegel, S. Francoeur and A. Mascarenhas, “Giant spin-orbit bowing in  $\text{GaAs}_{1-x}\text{Bi}_x$ ”, *Phys. Rev. Lett.*, vol. 97, pp. 067205, 2006.
- [73] S. Francoeur, S. Tixier, E. Young, T. Tiedje and A. Mascarenhas, “Bi isoelectric impurities in  $\text{GaAs}$ ”, *Phys. Rev. B*, vol. 77, pp. 085209, 2008.
- [74] M. Usman, C. A. Broderick, A. Lindsay, and E. P. O’Reilly, “Tight-binding analysis of the electronic structure of dilute bismide alloys of  $\text{GaP}$  and  $\text{GaAs}$ ”, *Phys. Rev. B*, vol. 84, pp. 245202, 2011.
- [75] Z. Batool, K. Hild, T. J. C. Hosea, X. Lu, T. Tiedje and S. J. Sweeney, “The electronic band structure of  $\text{GaBiAs/GaAs}$  layers: Influence of strain and band anti-crossing”, *J. Appl. Phys.*, vol. 111, pp. 113108, 2012.
- [76] P. Carrier and S.-H. Wei, “Calculated spin-orbit splitting of all diamondlike and zinc-blende semiconductors: Effects of  $p_{1/2}$  local orbitals and chemical trends”, *Phys. Rev. B*, vol. 70, pp. 035212, 2004.
- [77] Z. Batool, K. Hild, S. J. Sweeney, T. J. C. Hosea, A. R. Mohmad, T. Tiedje, X. Lu, A. Krotkus, V. Pacebutas and R. Butkute, “Resonance of bandgap and spin-orbit splitting in  $\text{GaBiAs/GaAs}$  alloys”, *2nd International Workshop on Bismuth Containing Semiconductors*, UK, July, 2011
- [78] Y. Tominaga, Y. Kinoshita, K. OE and M. Yoshimoto, “Structural investigation of  $\text{GaAs}_{1-x}\text{Bi}_x/\text{GaAs}$  multiquantum wells”, *Appl. Phys. Lett.*, vol. 93, pp. 131915, 2008.
- [79] Y. Tominaga, Y. Kinoshita, G. Feng, K. Oe and M. Yoshimoto, “Growth of  $\text{GaAs}_{1-x}\text{Bi}_x/\text{GaAs}$  multiquantum wells by molecular beam epitaxy”, *phys. stat. sol. (c)*, vol. 5, no. 9, pp. 2719, 2008. *phys. stat. sol. (c)*, vol. 3, no. 3, pp. 693, 2008.

- [80] T. Fuyuki, Y. Tominaga, K. Oe and M. Yoshimoto, "Growth of GaAs<sub>1-x</sub>Bi<sub>x</sub>/Al<sub>y</sub>Ga<sub>1-y</sub>As multi-quantum-well structures", *Jpn. J. Appl. Phys.*, vol. 49, pp. 070211, 2010.
- [81] P. Ludewig, N. Knaub, W. Stolz and K. Volz, "MOVPE growth of Ga(AsBi)/GaAs multi quantum well structures", *J. Cryst. Growth*, DOI: 10.1016/j.jcrysgro.2012.07.002, 2012.
- [82] K. Takahiro, K. Kawatsura, K. Oe and F. Nishiyama, "Structural characterization of GaAs<sub>1-x</sub>Bi<sub>x</sub> alloy by Rutherford Backscattering Spectrometry combined with the channeling technique", *Journal of electronic materials*, vol. 32, no. 1, pp. 34, 2003.
- [83] P. Wei, S. Tixer, M. Chicoine, S. Francoeur, A. Mascarenhas, T. Tiedje, F. Schiettekatte, "Ion beam characterization of GaAs<sub>1-x-y</sub>N<sub>x</sub>Bi<sub>y</sub> epitaxial layers", *Nuclear Instruments and Methods in Physics Research B*, vol. 219-220, pp. 671, 2004.
- [84] Y. Takehara, M. Yoshimoto, W. Huang, J. Saraie, K. Oe, A. Chayahara, and Y. Horino, "Lattice distortion of GaAsBi alloy grown on GaAs by Molecular Beam Epitaxy", *Jpn. J. Appl. Phys.*, vol. 45, no. 1A, pp. 67, 2006.
- [85] A. R. Mohmad, F. Bastiman, J. S. Ng, S. J. Sweeney and J. R. R. David, "Photoluminescence investigation of high quality GaAs<sub>1-x</sub>Bi<sub>x</sub> on GaAs", *Appl. Phys. Lett.*, vol. 98, pp. 122107, 2011.
- [86] N. A. Riordan, C. Gogineni, S. R. Johnson, X. Lu, T. Tiedje, D. Ding, Y.-H. Zhang, R. Fritz, K. Kolata, S. Chatterjee, K. Volz, S. W. Koch, "Temperature and pump power dependent photoluminescence", *J. Mater. Sci: Mater. Electron.*, vol. 23, pp. 1799, 2012.
- [87] Yu. I. Mazur, V. G. Dorogan, M. Schmidbauer, G. G. Tarasov, S. R. Johnson, X. Lu, S.-Q. Yu, Zh. M. Wang, T. Tiedje, G. J. Salamo, "Optical evidence of quantum well channel in low-temperature molecular beam epitaxy grown Ga(AsBi)/GaAs nanostructures", *Nanotechnology*, vol. 22, pp. 375703, 2011.
- [88] N. Hossain, I. P. Marko, S. R. Jin, K. Hild, S. J. Sweeney, R. B. Lewis, D. A. Beaton, and T. Tiedje, "Recombination mechanisms and band alignment of GaAs<sub>1-x</sub>Bi<sub>x</sub>/GaAs light emitting diodes", *Appl. Phys. Lett.*, vol. 100, pp. 051105, 2012.
- [89] J. Yoshida, T. Kita, O. Wada, and K. Oe, "Temperature dependence of GaAs<sub>1-x</sub>Bi<sub>x</sub> band gap Studied by photoreflectance spectroscopy", *Jpn. J. Appl. Phys.*, vol. 42, pp. 371, 2003.
- [90] K. Oe, "characteristics of semiconductor alloy GaAs<sub>1-x</sub>Bi<sub>x</sub>", *Jpn. J. Appl. Phys.*, vol. 41, no. 5A, pp. 2801, 2002.
- [91] K. Yamashita, M. Yoshimoto and K. Oe, "Temperature-insensitive refractive index of GaAsBi alloy for laser diode in WDM optical communication", *phys. stat. sol. (c)*, vol. 3, no. 3, pp. 693, 2006.
- [92] Y. Tominaga, K. Oe and M. Yoshimoto, "Temperature-insensitive photoluminescence emission wavelength in GaAs<sub>1-x</sub>Bi<sub>x</sub>/GaAs multiquantum wells", *phys. status solidi C*, vol. 8, no. 2, pp. 260, 2011.

- [93] K. Oe and H. Asia, "Proposal on a temperature-insensitive wavelength semiconductor laser", *IEICE Trans Electron*, vol. E79-C, pp1751, 1996.
- [94] D. G. Cooke, F. A. Hegmann, E. C. Young, and T. Tiedje, "Electron mobility in dilute GaAs bismide and nitride alloys measured by time-resolved terahertz spectroscopy", *Appl. Phys. Lett.*, vol. 89, pp. 122103, 2006.
- [95] R. N. Kini, L. Bhusal, A. J. Ptak, R. France and A. Mascarenhas, "Electron hall mobility in GaAsBi", *J. Appl. Phys.*, vol. 106, pp. 043705, 2009.
- [96] D. A. Beaton, R. B. Lewis, M. Masnadi-Shirazi and Tiedje, "Temperature dependence of hole mobility in GaAs<sub>1-x</sub>Bi<sub>x</sub> alloys", *J. Appl. Phys.*, vol. 108, pp. 083708, 2010.
- [97] B. Fluegel, R. N. Kini, A. J. Ptak, D. Beaton, K. Alberi and A. Mascarenhas, "Shubnikov-de Haas measurement of electron effective mass in GaAs<sub>1-x</sub>Bi<sub>x</sub>", *Appl. Phys. Lett.*, vol. 99, pp. 162108, 2011.
- [98] R. N. Kini, A. J. Ptak, B. Fluegel, R. France, R. C. Reedy, and A. Mascarenhas, "Effect of Bi alloying on the hole transport in the dilute bismide alloy GaAs<sub>1-x</sub>Bi<sub>x</sub>", *Phys. Rev. B*, vol. 83, pp. 075307, 2011.
- [99] K. Kado, T. Fuyuki, K. Yamada, K. Oe, and M. Yoshimoto, "High Hole Mobility in GaAs<sub>1-x</sub>Bi<sub>x</sub> Alloys", *Jpn. J. Appl. Phys.*, vol. 51, pp. 040204, 2012.
- [100] K. Bertulis, A. Krotkus, G. Aleksejenko, V. Pačebutas, R. Adomavičius, G. Molis, and S. Marcinkevičius, "GaBiAs: A material for optoelectronic terahertz devices", *Appl. Phys. Lett.*, vol. 88, pp. 201112, 2006.
- [101] R. B. Lewis, D. A. Beaton, X. Lu and T. Tiedje, "GaAs<sub>1-x</sub>Bi<sub>x</sub> light emitting diode", *J. Cryst. Growth*, vol. 311, pp. 1872, 2009.
- [102] Y. Tominaga, K. Oe, and M. Yoshimoto, "Low temperature dependence of oscillation wavelength in GaAs<sub>1-x</sub>Bi<sub>x</sub> laser by photo-pumping", *Appl. Phys. Express*, vol. 3, pp. 062201, 2010.
- [103] Y. Tominaga, K. Oe, and M. Yoshimoto, "Photo-pumped GaAs<sub>1-x</sub>Bi<sub>x</sub> lasing operation with low-temperature-dependent oscillation wavelength", *Proc. SPIE*, vol. 8277, pp. 827702, 2012.
- [104] S. Adachi, "Band gaps and refractive indices of AlGaAsSb, GaInAsSb, and InPAsSb: Key properties for a variety of the 2 - 4 μm optoelectronic device applications", *J. Appl. Phys.*, vol. 61, no. 10, pp. 4869, 1987.
- [105] G. P. Donati, R. Kaspi and K. J. Malloy, "Interpolating semiconductor alloy parameters: Application to quaternary III-V band gaps", *J. Appl. Phys.*, vol. 94, no. 9, pp. 5814, 2003.



- [106] M. H. M. Reddy, D. A. Buell, A. S. Huntington, T. Asano, R. Koda, D. Feezell, D. Lofgreen, and L. A. Coldren, "Al<sub>0.95</sub>Ga<sub>0.05</sub>As<sub>0.56</sub>Sb<sub>0.44</sub> for lateral oxide-confinement layer in InP based devices", *Appl. Phys. Lett.*, vol. 82, no. 9, pp. 1329, 2003.
- [107] S. Basu, Y.-B. Chen, and Z. M. Zhang, "Microscale radiation in thermophotovoltaic devices—A review", *Int. J. Energy Res.*, vol. 31, no. 6-7, pp. 689, 2007.
- [108] V. L. Teofilo, P. Choong, J. Chang, Y.-L. Tseng, and S. Ermer, "Thermophotovoltaic energy conversion for space", *J. Phys. Chem. C*, vol. 112, no. 21, pp. 7841, 2008.
- [109] V. M. Andreev, "An overview of TPV cell technologies", Thermophotovoltaic Generation of Electricity: 5th conference, *AIP Conf. Proc.*, 653, pp. 289, 2003.
- [110] T. J. Coutts, "An overview of thermophotovoltaic generation of electricity", *Sol. Energ. Mat. Sol. Cells*, vol. 66, pp. 443, 2001.
- [111] A. C. Day, W. E. Horne, and M. D. Morgan, "Application of the GaSb solar cell in isotope-heated power systems", *Photovoltaic Specialists Conference*, vol. 2, pp. 1320, 1990.
- [112] R. S. Tuley and R. J. Nicholas, "Band gap dependent thermophotovoltaic device performance using the InGaAs and InGaAsP material system", *J. Appl. Phys.*, vol. 108, pp. 084516, 2010.
- [113] <http://en.wikipedia.org/wiki/Sun>
- [114] C. H. Henry, "Limiting efficiencies of ideal single and multiple energy gap terrestrial solar cells", *J. Appl. Phys.*, vol. 51, no. 8, pp. 4494, 1980.
- [115] R. E. Nelson, "A brief history of thermophotovoltaic development", *Semicond. Sci. Technol.*, vol. 18, pp. S141, 2003.
- [116] A. W. Bett and O. V. Sulima, "GaSb photovoltaic cells for applications in TPV generators", *Semicond. Sci. Technol.*, vol. 18, pp. S184, 2003.
- [117] M. G. Mauk and V. M. Andreev, "GaSb-related materials for TPV cells", *Semicond. Sci. Technol.*, vol. 18, pp. S191, 2003.
- [118] <http://jxcystals.com/>
- [119] C. A. Wang, H. K. Choi, D. C. Oakley, G. W. Charache, "Recent progress in GaInAsSb thermophotovoltaics grown by organometallic vapor-phase epitaxy", *J. Cryst. Growth*, vol. 195, pp. 346, 1998.
- [120] C. A. Wang, H. K. Choi, S. L. Ransom, G. W. Charache, L. R. Danielson and D. M. Depoy, "High-quantum-efficiency 0.5 eV GaInAsSb/GaSb thermophotovoltaic devices", *App. Phys. Lett.*, vol. 75, no. 9, pp. 1305, 1999.

- [121] M. W. Dashiell, et al. "Quaternary InGaAsSb Thermophotovoltaic Diodes", *IEEE Trans. Electron. Dev.*, vol. 53, no. 12, pp. 2879, 2006.
- [122] C. A. Wang, H. K. Choi, D. C. Oakley, and G. W. Charache, "Extending the cutoff wavelength of lattice-matched GaInAsSb/GaSb thermophotovoltaic devices", *Fourth NREL Conference (AIP Conf. Proceedings)*, vol. 460, pp. 256, 1998.
- [123] J. G. Cederberg, J. D. Blaich, G. R. Girard, S. R. Lee, D. P. Nelson, C. S. Murray, "The development of (InGa)As thermophotovoltaic cells in InP using strain-relaxed In(Pas) buffers", *J. Cryst. Growth*, vol. 310, no. 15, pp. 3453, 2008.
- [124] D. Wilt, R. Wehrer, M. Palmisiano, M. Wanlass and C. Murray, "Monolithic interconnected modules (MIMs) for thermophotovoltaic energy conversion", *Semicond. Sci. Technol.*, vol. 18, no. 5, pp. S209, 2003.
- [125] R. Wehrer, M. Wanlass, D. Wilt, B. Wernsman, R. Siergiej, and J. Carapella, "InGaAs series-connected, tandem MIM TPV converters", *Photovoltaic Energy Conversion, Proceedings of 3rd World Conference*, vol. 1, pp. 892, 2003.
- [126] R. R. Siergiej, S. Sinharoy, T. Valko, R. J. Wehrer, B. Wernsman, S. D. Link, r. W. Schultz, and R. L. Messham, "InGaAsP/InGaAs tandem TPV device", *AIP Conference Proceedings*, vol. 738, pp.480, 2004.
- [127] K. J. Cheetham, P. J. Carrington, N. B. Cook, A. Krier, "Low bandgap GaInAsSbP pentanary thermophotovoltaic didoes", *Sol. Energ. Mat. Sol. Cells*, vol. 95, no. 2, pp. 534, 2011.
- [128] A. Y. Cho, "Morphology of epitaxial growth of GaAs by a molecular beam method: the observation of surface structures", *J. Appl. Phys.*, vol. 41, no. 7, pp. 2780, 1970.
- [129] A. Y. Cho, "GaAs epitaxy by a molecular meam method: mbservations of surface structure on the (001) face", *J. Appl. Phys.*, vol. 42, no. 5, pp. 2074, 1971.
- [130] A. Y. Cho, "Film deposition by molecular-beam techniques", *J. Vac. Sci. Technol.* vol. 8, no. 5, pp. S31, 1971
- [131] J. P. van der Ziel, R. Dingle, R. C. Miller, W. Wiegmann, and W. A. Nordland, "Laser oscillation from quantum states in very thin GaAs-Al<sub>0.2</sub>Ga<sub>0.8</sub>As multilayer structures", *Appl. Phys. Lett.*, vol. 26, no. 8, pp. 463, 1975.
- [132] W. T. Tsang, "Extremely low threshold (AlGa)As modified multi-quantum well heterostructure lasers grown by molecular beam epitaxy", *Appl. Phys. Lett.*, vol. 39, no. 10, pp. 786, 1981.
- [133] H. Morkoc and P. M. Solomon, "The HEMT: A superfast transistor: An experimental GaAs-AlGaAs device switches in picoseconds and generates little heat. This is just what supercomputers need", *IEEE Spectrum*, vol. 21, no. 2, pp. 28, 1984.

- [134] D. L. Smith and V. Y. Pickhardt, "Molecular beam epitaxy of II-VI compounds", *J. Appl. Phys.*, vol. 46, no. 6, pp. 2366, 1975.
- [135] G. L. Patton, S. S. Iyer, S. L. Delage, S. Tiwari, J. M. C. Stork, "Silicon-Germanium-base heterojunction bipolar transistors by molecular beam epitaxy", *IEEE Electron Device Letters*, vol. 9, no. 4, pp. 165, 1988.
- [136] R. A. McKee, F. J. Walker, J. R. Conner, E. D. Specht, and D. E. Zelmon, "Molecular beam epitaxy growth of epitaxial barium silicide, barium oxide, and barium titanate on silicon", *Appl. Phys. Lett.*, vol. 59, no. 7, pp. 782, 1991.
- [137] J. H. Neave, B. A. Joyce, P. J. Dobson and N. Norton, "Dynamics of Film Growth of GaAs by MBE from RHEED Observations", *Appl. Phys. A*, vol. 31, pp. 1, 1983
- [138] J. R. Arthur, "Molecular beam epitaxy", *Surface Science*, vol. 500, pp. 189, 2002.
- [139] A. S. Bracker, M. J. Yang, B. R. Bennett, J. C. Culbertson, W. J. Moore, "Surface reconstruction phase diagrams for InAs, AlSb and GaSb", *J. Cryst. Growth*, vol. 220, pp. 384, 2000.
- [140] E. J. Koerperick, L. M. Murray, D. T. Norton, T. F. Boggess, J. P. Prineas, "Optimization of MBE-grown GaSb buffer layers and surface effects of antimony stabilization flux", *J. Cryst. Growth*, vol. 212, pp. 185, 2010.
- [141] D. Kandel, E. Kaxiras, "Surfactant mediated crystal growth of semiconductors", *Phys. Rev. Lett.*, vol. 75, no. 14, pp. 2742, 1995.
- [142] E. Tournié, N. Grandjean, A. Trampert, J. Massies, K.H. Ploog, "Surfactant-mediated molecular-beam epitaxy of III-V strained-layer heterostructures", *J. Cryst. Growth*, vol. 150, pp. 460, 1995.
- [143] G. Feng, K. Oe and M. Yoshimoto, "Temperature dependence of Bi behavior in MBE growth of InGaAs/InP", *J. Cryst. Growth*, vol. 301-302, pp. 121, 2007.
- [144] M. R. Pillai, S. S. Kim, S. T. Ho and S. A. Barnett, "Growth of  $\text{In}_x\text{Ga}_{1-x}\text{As}/\text{GaAs}$  heterostructures using Bi as a surfactant", *J. Vac. Sci. Technol. B*, vol. 18, no. 3, pp. 1232, 2000.
- [145] B. N. Zvonkov, I. A. Karpovich, N. V. Baidus, D. O. Filatov, S. V. Morozov and Yu. Yu. Gushina, "Surfactant effect of bismuth in the MOVPE growth of the InAs quantum dots on GaAs", *Nanotechnology*, vol. 11, pp. 221, 2000.
- [146] S. W. Sun, C. M. Fetzer, R. T. Lee, J. K. Shurtleff and G. B. Stringfellow, "Bi surfactant effects on ordering in GaInP grown by organometallic vapor-phase epitaxy", *Appl. Phys. Lett.*, vol. 76, no. 19, pp. 2716, 2000.
- [147] R. T. Lee, C. M. Fetzer, S. W. Jun, D. C. Chapman, J. K. Shurtleff, G. B. Stringfellow, Y. W. Ok, and T. Y. Seong, "Enhancement of compositional modulation in GaInP epilayers

- by the addition of surfactants during organometallic vapor phase epitaxy growth”, *J. Cryst. Growth*, vol. 233, pp. 490, 2001.
- [148] L. Zhang, H. F. Tang, J. Schieke, M. Mavrikakis, and T. F. Kuech, “Influence of Bi impurity as a surfactant during the growth of GaN by metalorganic vapor phase epitaxy”, *J. Cryst. Growth*, vol. 242, pp. 302, 2002.
- [149] S. Tixier, M. Adamcyk, E. C. Young, J. H. Schmid, T. Tiedje, “Surfactant enhanced growth of GaNAs and InGaNAs using bismuth”, *J. Cryst. Growth*, vol. 251, pp. 449, 2003.
- [150] R. R. Wixom, L. W. Rieth, and G. B. Stringfellow, “Sb and Bi surfactant effects on homo-epitaxy of GaAs on (0 0 1) patterned substrates”, *J. Cryst. Growth*, vol. 265, pp. 367, 2004.
- [151] E. C. Yong, S. Tixier, and T. Tiedje, “Bismuth surfactant growth of the dilute nitride  $\text{GaN}_x\text{As}_{1-x}$ ”, *J. Cryst. Growth*, vol. 279, pp. 316, 2005.
- [152] H. Okamoto, T. Tawara, H. Gotoh, H. Kamada, and T. Sogawa, “Growth and characterization of telecommunication-wavelength quantum dots using Bi as a surfactant”, *Jpn. J. Appl. Phys.*, vol. 49, pp. 06GJ01, 2010.
- [153] A. J. Ptak, D. A. Beaton, A. Mascarenhas, “Growth of BGaAs molecular-beam epitaxy and the effects of a bismuth surfactant”, *J. Cryst. Growth*, vol. 351, pp. 122, 2012.
- [154] D. Fan, Z. Zeng, V. G. Dorogan, Y. Hirono, C. Li, Yu. I. Mazur, S.-Q. Yu, S. R. Johnson, Zh. M. Wang and G. J. Salamo, “Bismuth surfactant mediated growth of InAs quantum dots by molecular beam epitaxy”, *J. Mater. Sci: Mater. Electron.*, DOI: 10.1007/s10854-012-0987-z, 2012.
- [155] U. W. Pohl, K. Pötschke, A. Schliwa, F. Guffarth, D. Bimberg, N. D. Zakharov, P. Werner, M. B. Lifshits, V. A. Shchukin, D. E. Jesson, “Evolution of a multimodal distribution of self-organized InAs/GaAs quantum dots”, *Phys. Rev. B*, vol. 72, pp. 245332, 2005.
- [156] J. Porsche, A. Ruf, M. Geiger, F. Scholz, “Size control of self-assembled InP/GaInP quantum islands”, *J. Cryst. Growth*, vol. 195, pp. 591, 1998.
- [157] G. Wang, S. Fafard, D. Leonard, J. E. Bowers, J. L. Merz, P. M. Petroff, “Time-resolved optical characterization of InGaAs/GaAs quantum dots”, *Appl. Phys. Lett.*, vol. 64, no. 21, pp. 2815, 1994.
- [158] D. Fan, Z. Zeng, X. Hu, V. G. Dorogan, C. Li, M. Benamara, M. E. Hawkrige, Yu. I. Mazur, S.-Q. Yu, S. R. Johnson, Zh. M. Wang, and G. J. Salamo, “Molecular beam epitaxy growth of GaAsBi/GaAs/AlGaAs separate confinement heterostructures”, *Appl. Phys. Lett.*, vol. 101, pp. 181103, 2012.
- [159] U. W. Arndt, D. C. Creagh, R. D. Deslattes, J. H. Hubbell, P. Indelicato, E. g. Kessler Jr and E. Lindroth, “X-rays”, *International Tables for Crystallography*, vol, C, pp. 191, 2006.

- [160] P. J. Brown, A. G. Fox, E. N. Maslen, M. A. O’Keefe and B. T. M. Willis, “Intensity of diffracted intensities”, *International Tables for Crystallography*, vol. C, pp. 554, 2006.
- [161] M. B. Panish, H. C. Casey, S. Sumski, and P. W. Foy, “Reduction of threshold current density in GaAs-Al<sub>x</sub>Ga<sub>1-x</sub>As heterostructure lasers by separate optical and carrier confinement”, *Appl. Phys. Lett.*, vol. 22, no. 11, pp. 590, 1973.
- [162] G. H. B. Thompson and P. A. Kirkby, “Low threshold-current density in 5-layer-heterostructure (GaAl)As/GaAs localised-gain-region injection lasers”, *Electron. Lett.*, vol. 9, pp. 295, 1973.
- [163] H. C. Casey, M. B. Panish, W. O. Schlosser, and T. L. Paoli, “GaAs-Al<sub>x</sub>Ga<sub>1-x</sub>As heterostructure laser with separate optical and carrier confinement”, *J. Appl. Phys.*, vol. 45, no. 1, pp. 322, 1974.
- [164] S. R. Johnson, C. Z. Guo, S. Chaparro, Yu. G. Sadofyev, J. Wang, Y. Cao, N. Samal, J. Xu, S.Q. Yu, D. Ding, Y.-H. Zhang, “GaAsSb/GaAs band alignment evaluation for long-wave photonic applications”, *J. Cryst. Growth*, vol. 251, pp. 521, 2003.
- [165] S.-Q. Yu, X. Jin, S. R. Johnson, and Y.-H. Zhang, “Gain saturation and carrier distribution effects in molecular beam epitaxy”, *J. Vac. Sci. Technol. B*, vol. 24, no. 3, pp. 1617, 2006.
- [166] S.-Q. Yu, D. Ding, J.-B Wang, N. Samal, X. Jin, Y. Cao, S. R. Johnson, and Y.-H. Zhang, “High performance GaAsSb/GaAs quantum well lasers”, *J. Vac. Sci. Technol. B*, vol. 25, no. 5, pp. 1658, 2007.
- [167] R. W. H. Engelmann, C.-L. Shieh, and C. Shu, “multiquantum well lasers: Threshold consideration”, in *Quantum Well Lasers*, edited by P. S. Zory, Jr., Academic, San Diego, pp. 166–176, 1993
- [168] A. R. Mohamad, F. Bastiman, C. J. Hunter, R. Richards, S. J. Sweeney, J. S. Ng and J. P. R. David, “Effect of rapid thermal annealing on GaAs<sub>1-x</sub>Bi<sub>x</sub> alloys”, *Appl. Phys. Lett.*, vol. 101, pp. 012106, 2012.
- [169] R. A. Stall, C. E. C. Wood, P. D. Kirchner, and L. F. Eastman, “Growth-parameter dependence of deep levels in molecular-beam-epitaxial GaAs”, *Electron. Lett.*, vol. 16, no. 5, pp. 171, 1980.
- [170] M. Missous, “Stoichiometric low-temperature GaAs and AlGaAs: A reflection high-energy electron-diffraction study”, *J. Appl. Phys.*, vol. 78, no. 7, pp. 4467, 1995.
- [171] M. Missous and S. O’Hagan, “Nonstoichiometry and dopants related phenomena in low temperature GaAs by molecular beam epitaxy”, *J. Appl. Phys.*, vol. 75, no. 7, pp. 3396, 1994.
- [172] D. D. Nolte, “Semi-insulating semiconductor heterostructures: Optoelectronic properties and applications”, *J. Appl. Phys.*, vol. 85, no. 9, pp. 6259, 1999.

- [173] M. Asai, F. Sato, H. Imamoto, K. Imanaka, and M. Shimura, "Low temperature (350 °C) growth of AlGaAs/GaAs laser diode by migration enhanced epitaxy", *J. Appl. Phys.*, vol. 64, no. 1, pp. 432, 1988.
- [174] Y. Horikoshi, M. Kawashima, and H. Yamaguchi, "Migration-enhanced epitaxy of GaAs and AlGaAs", *Jpn. J. Appl. Phys.*, vol. 27, no. 2, pp. 169, 1988.
- [175] K. M. Yu, M. Kaminska, and Z. Liliental-Weber, "Characterization of GaAs layers grown by low temperature molecular beam epitaxy using ion beam techniques", *J. Appl. Phys.*, vol. 72, no. 7, pp. 2850, 1992.
- [176] M. Kaminska, Z. Liliental-Weber, E. R. Weber, T. George, J. B. Kortright, F. W. Smith, B-Y. Tsaur, and A. R. Calawa, "Structural properties of As-rich GaAs grown by molecular beam epitaxy at low temperatures", *Appl. Phys. Lett.*, vol. 54, no. 19, pp. 1881, 1989.
- [177] M. D. Sturge, "Optical Absorption of Gallium Arsenide between 0.6 and 2.75 eV", *Phys. Rev.*, vol. 127, no. 3, pp. 768, 1962.
- [178] H. C. Casey, D. D. Sell, and K. W. Wecht, "Concentration dependence of the absorption coefficient for n- and p-type GaAs between 1.3 and 1.6 eV", *J. Appl. Phys.*, vol. 46, no.1, pp. 250, 1975.

## APPENDIX A: PERMISSION TO REUSE COPYRIGHTED MATERIALS

1/23/13

Rightslink Printable License

### AMERICAN INSTITUTE OF PHYSICS LICENSE TERMS AND CONDITIONS

Jan 23, 2013

**All payments must be made in full to CCC. For payment instructions, please see information listed at the bottom of this form.**

License Number	3074950396113
Order Date	Jan 23, 2013
Publisher	American Institute of Physics
Publication	Applied Physics Letters
Article Title	Molecular beam epitaxy growth of GaAsBi/GaAs/AlGaAs separate confinement heterostructures
Author	Dongsheng Fan, Zhaoquan Zeng, Xian Hu, Vitaliy G. Dorogan, et al.
Online Publication Date	Oct 29, 2012
Volume number	101
Issue number	18
Type of Use	Thesis/Dissertation
Requestor type	Author (original article)
Format	Print and electronic
Portion	Excerpt (> 800 words)
Will you be translating?	No
Title of your thesis / dissertation	III-V Bismide optoelectronic devices
Expected completion date	May 2013
Estimated size (number of pages)	150
Total	0.00 USD

#### Terms and Conditions

American Institute of Physics -- Terms and Conditions: Permissions Uses

American Institute of Physics ("AIP") hereby grants to you the non-exclusive right and license to use and/or distribute the Material according to the use specified in your order, on a one-time basis, for the specified term, with a maximum distribution equal to the number that you have ordered. Any links or other content accompanying the Material are not the subject of this license.

1. You agree to include the following copyright and permission notice with the reproduction of the Material: "Reprinted with permission from [FULL CITATION]. Copyright [PUBLICATION YEAR], American Institute of Physics." For an article, the copyright and permission notice must be printed on the first page of the article or book chapter. For photographs, covers, or tables, the copyright and permission notice may appear with the Material, in a footnote, or in the reference list.
2. If you have licensed reuse of a figure, photograph, cover, or table, it is your responsibility to ensure that the material is original to AIP and does not contain the copyright of another entity, and that the copyright notice of the figure, photograph, cover, or table does not indicate that it was reprinted by AIP, with permission, from another source. Under no

- circumstances does AIP, purport or intend to grant permission to reuse material to which it does not hold copyright.
3. You may not alter or modify the Material in any manner. You may translate the Material into another language only if you have licensed translation rights. You may not use the Material for promotional purposes. AIP reserves all rights not specifically granted herein.
  4. The foregoing license shall not take effect unless and until AIP or its agent, Copyright Clearance Center, receives the Payment in accordance with Copyright Clearance Center Billing and Payment Terms and Conditions, which are incorporated herein by reference.
  5. AIP or the Copyright Clearance Center may, within two business days of granting this license, revoke the license for any reason whatsoever, with a full refund payable to you. Should you violate the terms of this license at any time, AIP, American Institute of Physics, or Copyright Clearance Center may revoke the license with no refund to you. Notice of such revocation will be made using the contact information provided by you. Failure to receive such notice will not nullify the revocation.
  6. AIP makes no representations or warranties with respect to the Material. You agree to indemnify and hold harmless AIP, American Institute of Physics, and their officers, directors, employees or agents from and against any and all claims arising out of your use of the Material other than as specifically authorized herein.
  7. The permission granted herein is personal to you and is not transferable or assignable without the prior written permission of AIP. This license may not be amended except in a writing signed by the party to be charged.
  8. If purchase orders, acknowledgments or check endorsements are issued on any forms containing terms and conditions which are inconsistent with these provisions, such inconsistent terms and conditions shall be of no force and effect. This document, including the CCC Billing and Payment Terms and Conditions, shall be the entire agreement between the parties relating to the subject matter hereof.

This Agreement shall be governed by and construed in accordance with the laws of the State of New York. Both parties hereby submit to the jurisdiction of the courts of New York County for purposes of resolving any disputes that may arise hereunder.

**If you would like to pay for this license now, please remit this license along with your payment made payable to "COPYRIGHT CLEARANCE CENTER" otherwise you will be invoiced within 48 hours of the license date. Payment should be in the form of a check or money order referencing your account number and this invoice number RLNK500940636. Once you receive your invoice for this order, you may pay your invoice by credit card. Please follow instructions provided at that time.**

**Make Payment To:  
Copyright Clearance Center  
Dept 001  
P.O. Box 843006  
Boston, MA 02284-3006**

**For suggestions or comments regarding this order, contact RightsLink Customer Support: [customercare@copyright.com](mailto:customercare@copyright.com) or +1-877-622-5543 (toll free in the US) or +1-978-646-2777.**

**Gratis licenses (referencing \$0 in the Total field) are free. Please retain this printable license for your reference. No payment is required.**





**AMERICAN INSTITUTE OF PHYSICS LICENSE  
TERMS AND CONDITIONS**

Jan 23, 2013

**All payments must be made in full to CCC. For payment instructions, please see information listed at the bottom of this form.**

License Number	3074950676110
Order Date	Jan 23, 2013
Publisher	American Institute of Physics
Publication	Applied Physics Letters
Article Title	Molecular beam epitaxy growth of GaAsBi/GaAs/AlGaAs separate confinement heterostructures
Author	Dongsheng Fan, Zhaoquan Zeng, Xian Hu, Vitaliy G. Dorogan, et al.
Online Publication Date	Oct 29, 2012
Volume number	101
Issue number	18
Type of Use	Thesis/Dissertation
Requestor type	Author (original article)
Format	Print and electronic
Portion	Figure/Table
Number of figures/tables	4
Title of your thesis / dissertation	III-V Bismide optoelectronic devices
Expected completion date	May 2013
Estimated size (number of pages)	150
Total	0.00 USD

**Terms and Conditions**

American Institute of Physics -- Terms and Conditions: Permissions Uses

American Institute of Physics ("AIP") hereby grants to you the non-exclusive right and license to use and/or distribute the Material according to the use specified in your order, on a one-time basis, for the specified term, with a maximum distribution equal to the number that you have ordered. Any links or other content accompanying the Material are not the subject of this license.

1. You agree to include the following copyright and permission notice with the reproduction of the Material: "Reprinted with permission from [FULL CITATION]. Copyright [PUBLICATION YEAR], American Institute of Physics." For an article, the copyright and permission notice must be printed on the first page of the article or book chapter. For photographs, covers, or tables, the copyright and permission notice may appear with the Material, in a footnote, or in the reference list.
2. If you have licensed reuse of a figure, photograph, cover, or table, it is your responsibility to ensure that the material is original to AIP and does not contain the copyright of another entity, and that the copyright notice of the figure, photograph, cover, or table does not indicate that it was reprinted by AIP, with permission, from another source. Under no

**AMERICAN INSTITUTE OF PHYSICS LICENSE  
TERMS AND CONDITIONS**

Feb 14, 2013

**All payments must be made in full to CCC. For payment instructions, please see information listed at the bottom of this form.**

License Number	3087740749665
Order Date	Feb 14, 2013
Publisher	American Institute of Physics
Publication	Journal of Vacuum Science & Technology B
Article Title	MBE grown GaAsBi/GaAs double quantum well separate confinement heterostructures
Author	Dongsheng Fan, Perry C. Grant, Shui-Qing Yu, Vitaliy G. Dorogan, et al.
Online Publication Date	Feb 14, 2013
Volume number	31
Issue number	3
Type of Use	Thesis/Dissertation
Requestor type	Author (original article)
Format	Print and electronic
Portion	Figure/Table
Number of figures/tables	4
Order reference number	124
Title of your thesis / dissertation	III-V Bismide optoelectronic devices
Expected completion date	May 2013
Estimated size (number of pages)	150
Total	0.00 USD

**Terms and Conditions**

American Vacuum Society -- Terms and Conditions: Permissions Uses

American Vacuum Society ("AVS") hereby grants to you the non-exclusive right and license to use and/or distribute the Material according to the use specified in your order, on a one-time basis, for the specified term, with a maximum distribution equal to the number that you have ordered. Any links or other content accompanying the Material are not the subject of this license.

1. You agree to include the following copyright and permission notice with the reproduction of the Material: "Reprinted with permission from [FULL CITATION]. Copyright [PUBLICATION YEAR], American Vacuum Society." For an article, the copyright and permission notice must be printed on the first page of the article or book chapter. For photographs, covers, or tables, the copyright and permission notice may appear with the Material, in a footnote, or in the reference list.
2. If you have licensed reuse of a figure, photograph, cover, or table, it is your responsibility to ensure that the material is original to AVS and does not contain the copyright of another entity, and that the copyright notice of the figure, photograph, cover, or table does not

**AMERICAN INSTITUTE OF PHYSICS LICENSE  
TERMS AND CONDITIONS**

Feb 14, 2013

**All payments must be made in full to CCC. For payment instructions, please see information listed at the bottom of this form.**

License Number	3087740469943
Order Date	Feb 14, 2013
Publisher	American Institute of Physics
Publication	Journal of Vacuum Science & Technology B
Article Title	MBE grown GaAsBi/GaAs double quantum well separate confinement heterostructures
Author	Dongsheng Fan, Perry C. Grant, Shui-Qing Yu, Vitaliy G. Dorogan, et al.
Online Publication Date	Feb 14, 2013
Volume number	31
Issue number	3
Type of Use	Thesis/Dissertation
Requestor type	Author (original article)
Format	Print and electronic
Portion	Excerpt (> 800 words)
Will you be translating?	No
Order reference number	123
Title of your thesis / dissertation	III-V Bismide optoelectronic devices
Expected completion date	May 2013
Estimated size (number of pages)	150
Total	0.00 USD

**Terms and Conditions**

American Vacuum Society -- Terms and Conditions: Permissions Uses

American Vacuum Society ("AVS") hereby grants to you the non-exclusive right and license to use and/or distribute the Material according to the use specified in your order, on a one-time basis, for the specified term, with a maximum distribution equal to the number that you have ordered. Any links or other content accompanying the Material are not the subject of this license.

1. You agree to include the following copyright and permission notice with the reproduction of the Material: "Reprinted with permission from [FULL CITATION]. Copyright [PUBLICATION YEAR], American Vacuum Society." For an article, the copyright and permission notice must be printed on the first page of the article or book chapter. For photographs, covers, or tables, the copyright and permission notice may appear with the Material, in a footnote, or in the reference list.
2. If you have licensed reuse of a figure, photograph, cover, or table, it is your responsibility to ensure that the material is original to AVS and does not contain the copyright of another entity, and that the copyright notice of the figure, photograph, cover, or table does not

**SPRINGER LICENSE  
TERMS AND CONDITIONS**

Jan 23, 2013

---

This is a License Agreement between Dongsheng Fan ("You") and Springer ("Springer") provided by Copyright Clearance Center ("CCC"). The license consists of your order details, the terms and conditions provided by Springer, and the payment terms and conditions.

**All payments must be made in full to CCC. For payment instructions, please see information listed at the bottom of this form.**

License Number	3074951184202
License date	Jan 23, 2013
Licensed content publisher	Springer
Licensed content publication	Journal of Materials Science: Materials in Electronics
Licensed content title	Bismuth surfactant mediated growth of InAs quantum dots by molecular beam epitaxy
Licensed content author	Dongsheng Fan
Licensed content date	Jan 1, 2012
Type of Use	Thesis/Dissertation
Portion	Excerpts
Author of this Springer article	Yes and you are the sole author of the new work
Order reference number	
Title of your thesis / dissertation	III-V Bismide optoelectronic devices
Expected completion date	May 2013
Estimated size(pages)	150
Total	0.00 USD

**Terms and Conditions**

**Introduction**

The publisher for this copyrighted material is Springer Science + Business Media. By clicking "accept" in connection with completing this licensing transaction, you agree that the following terms and conditions apply to this transaction (along with the Billing and Payment terms and conditions established by Copyright Clearance Center, Inc. ("CCC"), at the time that you opened your Rightslink account and that are available at any time at <http://myaccount.copyright.com>).

**Limited License**

With reference to your request to reprint in your thesis material on which Springer Science and Business Media control the copyright, permission is granted, free of charge, for the use indicated in

your enquiry.

Licenses are for one-time use only with a maximum distribution equal to the number that you identified in the licensing process.

This License includes use in an electronic form, provided its password protected or on the university's intranet or repository, including UMI (according to the definition at the Sherpa website: <http://www.sherpa.ac.uk/romeo/>). For any other electronic use, please contact Springer at ([permissions.dordrecht@springer.com](mailto:permissions.dordrecht@springer.com) or [permissions.heidelberg@springer.com](mailto:permissions.heidelberg@springer.com)).

The material can only be used for the purpose of defending your thesis, and with a maximum of 100 extra copies in paper.

Although Springer holds copyright to the material and is entitled to negotiate on rights, this license is only valid, provided permission is also obtained from the (co) author (address is given with the article/chapter) and provided it concerns original material which does not carry references to other sources (if material in question appears with credit to another source, authorization from that source is required as well).

Permission free of charge on this occasion does not prejudice any rights we might have to charge for reproduction of our copyrighted material in the future.

#### Altering/Modifying Material: Not Permitted

You may not alter or modify the material in any manner. Abbreviations, additions, deletions and/or any other alterations shall be made only with prior written authorization of the author(s) and/or Springer Science + Business Media. (Please contact Springer at ([permissions.dordrecht@springer.com](mailto:permissions.dordrecht@springer.com) or [permissions.heidelberg@springer.com](mailto:permissions.heidelberg@springer.com)))

#### Reservation of Rights

Springer Science + Business Media reserves all rights not specifically granted in the combination of (i) the license details provided by you and accepted in the course of this licensing transaction, (ii) these terms and conditions and (iii) CCC's Billing and Payment terms and conditions.

#### Copyright Notice:Disclaimer

You must include the following copyright and permission notice in connection with any reproduction of the licensed material: "Springer and the original publisher /journal title, volume, year of publication, page, chapter/article title, name(s) of author(s), figure number(s), original copyright notice) is given to the publication in which the material was originally published, by adding: with kind permission from Springer Science and Business Media"

#### Warranties: None

Example 1: Springer Science + Business Media makes no representations or warranties with respect to the licensed material.

Example 2: Springer Science + Business Media makes no representations or warranties with respect to the licensed material and adopts on its own behalf the limitations and disclaimers established by CCC on its behalf in its Billing and Payment terms and conditions for this licensing

transaction.

#### Indemnity

You hereby indemnify and agree to hold harmless Springer Science + Business Media and CCC, and their respective officers, directors, employees and agents, from and against any and all claims arising out of your use of the licensed material other than as specifically authorized pursuant to this license.

#### No Transfer of License

This license is personal to you and may not be sublicensed, assigned, or transferred by you to any other person without Springer Science + Business Media's written permission.

#### No Amendment Except in Writing

This license may not be amended except in a writing signed by both parties (or, in the case of Springer Science + Business Media, by CCC on Springer Science + Business Media's behalf).

#### Objection to Contrary Terms

Springer Science + Business Media hereby objects to any terms contained in any purchase order, acknowledgment, check endorsement or other writing prepared by you, which terms are inconsistent with these terms and conditions or CCC's Billing and Payment terms and conditions. These terms and conditions, together with CCC's Billing and Payment terms and conditions (which are incorporated herein), comprise the entire agreement between you and Springer Science + Business Media (and CCC) concerning this licensing transaction. In the event of any conflict between your obligations established by these terms and conditions and those established by CCC's Billing and Payment terms and conditions, these terms and conditions shall control.

#### Jurisdiction

All disputes that may arise in connection with this present License, or the breach thereof, shall be settled exclusively by arbitration, to be held in The Netherlands, in accordance with Dutch law, and to be conducted under the Rules of the 'Netherlands Arbitrage Instituut' (Netherlands Institute of Arbitration). **OR:**

**All disputes that may arise in connection with this present License, or the breach thereof, shall be settled exclusively by arbitration, to be held in the Federal Republic of Germany, in accordance with German law.**

#### Other terms and conditions:

v1.3

**If you would like to pay for this license now, please remit this license along with your payment made payable to "COPYRIGHT CLEARANCE CENTER" otherwise you will be invoiced within 48 hours of the license date. Payment should be in the form of a check or money order referencing your account number and this invoice number RLNK500940653. Once you receive your invoice for this order, you may pay your invoice by credit card. Please follow instructions provided at that time.**

**Make Payment To:  
Copyright Clearance Center  
Dept 001  
P.O. Box 843006**

**Boston, MA 02284-3006**

For suggestions or comments regarding this order, contact RightsLink Customer Support: [customer@copyright.com](mailto:customer@copyright.com) or +1-877-622-5543 (toll free in the US) or +1-978-646-2777.

Gratis licenses (referencing \$0 in the Total field) are free. Please retain this printable license for your reference. No payment is required.

---

---



**SPRINGER LICENSE  
TERMS AND CONDITIONS**

Jan 23, 2013

---

This is a License Agreement between Dongsheng Fan ("You") and Springer ("Springer") provided by Copyright Clearance Center ("CCC"). The license consists of your order details, the terms and conditions provided by Springer, and the payment terms and conditions.

**All payments must be made in full to CCC. For payment instructions, please see information listed at the bottom of this form.**

License Number	3074951074367
License date	Jan 23, 2013
Licensed content publisher	Springer
Licensed content publication	Journal of Materials Science: Materials in Electronics
Licensed content title	Bismuth surfactant mediated growth of InAs quantum dots by molecular beam epitaxy
Licensed content author	Dongsheng Fan
Licensed content date	Jan 1, 2012
Type of Use	Thesis/Dissertation
Portion	Figures
Author of this Springer article	Yes and you are the sole author of the new work
Order reference number	
Title of your thesis / dissertation	III-V Bismide optoelectronic devices
Expected completion date	May 2013
Estimated size(pages)	150
Total	0.00 USD

**Terms and Conditions**

**Introduction**

The publisher for this copyrighted material is Springer Science + Business Media. By clicking "accept" in connection with completing this licensing transaction, you agree that the following terms and conditions apply to this transaction (along with the Billing and Payment terms and conditions established by Copyright Clearance Center, Inc. ("CCC"), at the time that you opened your Rightslink account and that are available at any time at <http://myaccount.copyright.com>).

**Limited License**

With reference to your request to reprint in your thesis material on which Springer Science and Business Media control the copyright, permission is granted, free of charge, for the use indicated in

## APPENDIX B: LIST OF PAPERS

### Journals:

- [01] **D. Fan**, P. C. Grant, S.-Q. Yu, V. G. Dorogan, X. Hu, Z. Zeng, C. Li, M. E. Hawkrige, M. Benamara, Yu, I. Mazur, G. J. Salamo, S. R. Johnson, Zh. M. Wang, “MBE Grown GaAsBi/GaAs Double Quantum Well Separate Confinement Heterostructures”, *J. Vac. Sci Technol. B*, vol. 31, pp. 03C105, 2013.
- [02] **D. Fan**, Z. Zeng, X. Hu, V. G. Dorogan, C. Li, M. Benamara, M. E. Hawkrige, Yu, I. Mazur, S.-Q. Yu, S. R. Johnson, Zh. M. Wang, and G. J. Salamo, “Molecular Beam Epitaxy Growth of GaAsBi/GaAs/AlGaAs Separate Confinement Heterostructures”, *Appl. Phys. Lett.*, vol. 101, pp. 181103, 2012.
- [03] **D. Fan**, Z. Zeng, V. G. Dorogan, Y. Hirono, C. Li, Yu. I. Mazur, S.-Q. Yu, S. R. Johnson, Zh. M. Wang and G. J. Salamo, “Bismuth surfactant mediated growth of InAs quantum dots by molecular beam epitaxy”, *J. Mater. Sci: Mater. Eletron.*, DOI: 10.1007/s10854-012-0987-z, 2012.
- [04] C. Li, Z. Zeng, **D. Fan**, Y. Hirono, J. Wu, T. A. Morgan, X. Hu, S.-Q. Yu, Zh. M. Wang, and G. J. Salamo, “Bismuth Nano-droplets for Group-V Based Molecular-Beam Droplet Epitaxy”, *App. Phys. Lett.*, vol. 99, pp. 243113, 2011.
- [05] Z. Li, J. Wu, Zh. M. Wang, **D. Fan**, A. Guo, S. Li, S.-Q. Yu, O. Manasreh, G. J. Salamo, “InGaAs Quantum Well Grown on High-Index Surfaces for Superluminescent Diode Applications”, *Nanoscale Res. Lett.*, Vol. 5, No. 6, pp. 1079-1084, 2010.

### Conferences:

- [06] **D. Fan**, P. C. Grant, Z. Zeng, X. Hu, C. Li, V. G. Dorogan, M. E. Hawkrige, Yu, I. Mazur, S.-Q. Yu, S. R. Johnson, Zh. M. Wang, and G. J. Salamo, “GaAsBi/GaAs Multiple Quantum Wells Grown by Molecular Beam Epitaxy”, *29<sup>th</sup> North American Molecular Beam Epitaxy Conference (NAMBE)*, Atlanta GA, October 14-17, 2012.
- [07] **D. Fan**, Z. Zeng, X. Hu, V. G. Dorogan, Y. Hirono, C. Li, P. C. Grant, M. Benamara, M. E. Hawkrige, Yu, I. Mazur, S.-Q. Yu, S. R. Johnson, Zh. M. Wang, and G. J. Salamo, “High Optical Quality GaAsBi/GaAs/AlGaAs Separate Confinement Heterostructures”, *17th International Conference on Molecular Beam Epitaxy (MBE 2012)*, Nara, Japan, September 23-28, 2012.
- [08] **D. Fan**, Z. Zeng, X. Hu, V. G. Dorogan, Y. Hirono, C. Li, P. C. Grant, M. Benamara, M. E. Hawkrige, Yu, I. Mazur, S.-Q. Yu, S. R. Johnson, Zh. M. Wang, and G. J. Salamo, “Molecular Beam Epitaxy Growth of GaAsBi/GaAs/AlGaAs Separate Confinement Heterostructures”, *3<sup>rd</sup> International Workshop on Bismuth-Containing Semiconductors (3<sup>rd</sup> BCS)*, Victoria B.C., Canada, July15-18, 2012.

- [09] Z. Zeng, C. Li, **D. Fan**, Y. Hirono, T. A. Morgan, X. Hu, J. Wang, M. Singh, Zh. M. Wang, S.-Q. Yu, A. Q. Guo, and G. J. Salamo, “Fabrication of Bi<sub>2</sub>Te<sub>3</sub> Nanodots by Droplet Epitaxy on GaAs substrates”, *APS March Meeting*, Boston MA, Feb. 27th ~Mar. 2nd, 2012.
- [10] **D. Fan**, Z. Zeng, Zh. M. Wang, S. R. Johnson, S.-Q. Yu, and G. J. Salamo, “Molecular Beam Epitaxy Grown GaInAsSbBi alloys on GaSb substrates for mid-infrared laser diode applications”, *SPIE Photonics West 2012*, San Francisco CA, January 21-26, 2012.
- [11] **D. Fan**, J. Wu, Zh. M. Wang, S.-Q. Yu, and G. J. Salamo, “InAs QD light emitting diodes on in situ patterned substrates using Molecular Beam Epitaxy”, *SPIE Photonics West 2012*, San Francisco CA, January 21-26, 2012.
- [12] Z. Zeng, **D. Fan**, C. Li, Y. Hirono, T. A. Morgan, J. Wang, J. S. Lee, Zh. M. Wang, S.-Q. Yu, A. Q. Guo, and G. J. Salamo, “Epitaxial Growth of High-Quality Bi<sub>2</sub>Te<sub>3</sub> and Sb<sub>2</sub>Te<sub>3</sub> Thin Films on GaAs (111)”, *2011 MRS Fall Meeting & Exhibit*, Boston MA, Nov. 28th - Dec. 2nd, 2011.
- [13] **D. Fan**, Z. Zeng, V. G. Dorogan, Y. Hirono, C. Li, Yu. I. Mazur, Zh. M. Wang, S. R. Johnson, S.-Q. Yu, and G. J. Salamo, “Bismuth surfactant mediated growth of InAs quantum dots by Molecular Beam Epitaxy”, *2011 MRS Fall Meeting & Exhibit*, Boston MA, Nov. 28th - Dec. 2nd, 2011.
- [14] **D. Fan**, Z. Zeng, V. G. Dorogan, Y. Hirono, C. Li, Yu. I. Mazur, Zh. M. Wang, S. R. Johnson, S.-Q. Yu, G. J. Salamo, “Photoluminescence and Surface Morphology Characterization of GaAsBi Grown on GaAs by Molecular Beam Epitaxy”, *28<sup>th</sup> North American Molecular Beam Epitaxy Conference (NAMBE)*, San Diego CA, August 14-17, 2011.
- [15] **D. Fan**, S.-Q. Yu, Zh. M. Wang, S. R. Johnson and G. J. Salamo, “Novel GaInAsSbBi Materials for Mid-Infrared Type-I Quantum Well Lasers”, *2nd International Workshop on Bismuth-Containing Semiconductors (2nd BCS)*, Guildford, UK, July 18-20, 2011.

